UTPP-31

STUDY OF CHARGED INTERMEDIATE VECTOR BOSON PRODUCTION IN PROTON-ANTIPROTON COLLISIONS AT $\sqrt{s}$=1.8 TEV

JUNE 1988

MASAYUKI SHIBATA

Submitted in partial fulfillment of the requirements
for the degree of Doctor of Science
in Doctoral Program in
University of Tsukuba

UTPP–31

STUDY OF CHARGED INTERMEDIATE VECTOR BOSON PRODUCTION IN PROTON-ANTIPROTON COLLISIONS AT $\sqrt{s}$=1.8 TEV

JUNE 1988

MASAYUKI SHIBATA

Submitted in partial fulfillment of the requirements
for the degree of Doctor of Science
in Doctoral Program in
University of Tsukuba

Abstract

A study of Charged Intermediate Vector bosons (W's) observed in the Fermilab proton-antiproton collision experiment at $\sqrt{s}$ = 1.8 TeV is described. The Collider Detector at Fermilab (CDF) is the first general purpose detector built to study the world highest energy region in proton-antiproton collisions. The first physics run was carried out from January 1987 to May 1987. Event analysis is based on charged particle tracking, magnetic momentum analysis and fine-grained calorimetry. Charged particle momenta are analyzed in a 1.5 Tesla solenoidal magnetic field, generated by a superconducting coil, 3 m in diameter and 5 m in length. The calorimetry, which has a polar angle coverage from 2° to 178° and full azimuthal coverage, consists of electromagnetic shower counters and hadron calorimeters; and is segmented into about 5,000 projective "towers" or solid angle elements. A custom front-end electronics system followed by a large Fastbus network provides the readout of the approximately 100,000 detector channels.

During the period of data taking runs, approximately 4.8 x 10^5 events were recorded on magnetic tapes by high Pt electron triggers and jet triggers. After having eliminated runs with detector problems or recording problems, we have obtained 4.1 x 10^5 events corresponding to an integrated luminosity of 27.4 nb^{-1}. By selecting events which include at least one electromagnetic cluster whose ratio of hadronic to electromagnetic energy is less than 0.1, they were reduced to 5.9 x 10^4 events and were recorded on 134 DST's (Data Summary Tapes). In the offline data reduction, we first selected events containing a high Pt isolated electron by the following cuts: (i) the ratio of hadronic to electromagnetic energy is less than 0.05, (ii) the number of tracks pointing to the electromagnetic cluster equal to 1, (iii) the transverse energy measured by calorimetry should match the transverse momentum measured by the central tracking chamber, (iv) the high Pt electron should be isolated from hadronic jets. By requiring the presence of a large amount of missing transverse energy, we finally obtained 22 events of W candidates in the η (pseudo rapidity) range $-1.1 < \eta < 1.1$. Background estimations were made by a Monte Carlo simulation study and also by a visual inspection using a CDF event display program with a color graphic terminal. Of the 22 W candidates, 0.7 ± 0.5 events are QCD jet background, 1 event is $Z^0 \rightarrow e^+e^-$ and 1.4 ± 0.4 events are $W \rightarrow \tau\nu$, followed by $\tau \rightarrow e\nu\nu$. Subtraction of the backgrounds from the 22 W candidates yields 18.9 $\pm$ 4.7 $W \rightarrow e\nu$ events. The overall efficiency for W boson detection is estimated to be 0.33 ± 0.03 (sta) $\pm$ 0.03 (sys) from the Monte Carlo simulation study and the visual inspection. The cross section for the production of W's and subsequent decay to electron and neutrino is given by $\sigma \cdot B(W \rightarrow e\nu) = 2.1 \pm 0.6$ (sta) $\pm$ 0.4 (sys) nb, where the first error includes statistical and an uncertainty in a track reconstruction efficiency and the second error includes systematic due to an uncertainty in a luminosity measurement and an uncertainty in estimating a geometrical acceptance by using different sets of structure functions. The measured value is in good agreement with theoretical predictions based on the Drell-Yan mechanism including higher order QCD corrections.

ACKNOWLEDGMENTS

I would like to express my appreciation to Profs. K.Takikawa and K.Kondo for their guidance and continuous encouragements during the course of this experiment. In particular, Prof. K.Takikawa gave me several suggestions and advice on my thesis. It has been a great help to me. Prof. K.Kondo gave me a great opportunity to do a research in the proton-antiproton collision experiment at the world highest energy region in USA. It has been the most exciting experience for me. They have also created a relaxed atmosphere in which it is a pleasure to work.

I greatly appreciate Drs. K.Yasuoka, C.Blocker, Profs. S.Miyashita, H.Frisch, L.Hollway, L.Nodulman and Mr. M.Miller for their valuable suggestions and advice on the W particle analysis. Drs. K.Yasuoka and C.Blocker gave me an excellent environment of the offline electron analysis codes. That has made me possible to do efficient analysis of electrons from W boson decay. I also appreciate Dr. P.Berge for his developing the codes for the track reconstruction and its display in the central tracking chamber. His codes have been a essential part of my analysis.

I also thank Drs. Y.Takaiwa and J.Freeman for their developing Monte Carlo event generation and simulation programs in the CDF environment. I have used their programs for the estimation of the backgrounds for the W->ev events. Their simple and efficient programs have been a great help for my thesis.

My deepest thanks go to Dr. G.P.Yeh and G.W.Foster for their developing the CDF event display program and its faster version. I have used their programs to check the track reconstruction efficiency for the high transverse momentum particles in the central tracking chamber.

I also wish to thank Drs. S.Kim, M.Mishina, Y.Fukui, Y.Hayashide, H.Miyata, Messrs. Y.Morita and S.Kanda for their help in the construction of the plug electromagnetic calorimeters. It has been a nice experience to have worked with them.

This work was carried out as a program of the Collider Detector at Fermilab (CDF) under the accord of US-Japan collaboration in high energy physics. I wish to express my special thanks to Prof. R.Schwitters and Dr. A. Tollestrup (CDF leaders), Dr. K.C.Stanfield (Head of Research Division) and Dr. L.Lederman (Director of Fermilab).

The success of the CDF experiment was the results of the patient and hard works of many collaborators in appendix A. I wish to thank all of them.

This experiment would have been impossible without the successful operation of the Tevatron Collider by the whole Fermilab Accelerator Group. I also thank the many staff members of the Fermilab Computing Group members for their vigorous support of the experiment.

I wish to express my appreciation to Profs. S.Mikamo, S.Mori, Drs. T.Yamanouch, T.Kamon, Messrs. A.Yamashita, M.Sekiguchi, F.Ukegawa and T.Mimashi. It has been a pleasure to have useful discussions with them.

This work was supported by the Department of Energy, Contract Nos. W-31-109-ENG-38 (ANL); DE-ACO2-76ER03230 (Brandeis); DE-ACO2-76CH03000 (Fermilab); DE-ACO2-76ER03064 (Harvard); DE-ACO2-76ER01196 (Illinois); DE-ACO2-76SF00098 (LBL); DE-ACO2-76ER03071 (Pennsylvania); DE-ACO2-76ER01428 (Purdue); DE-ACO2-87ER40325 (Rockefeller); DE-AS05-81ER40039 (Texas A & M); DE-ACO2-76ER00881 (Wisconsin); the National Science Foundation, Grant No. NSF-PHY 86-01628 (Chicago), NSF-PHY-85-14193 (Rutgers); Institute Nazionale di Fisica Nucleare (Frascati, Pisa); and the Ministry of Education, Science and Culture of Japan (KEK, Tsukuba).

CONTENTS

Abstract

acknowledgments

1 Introduction 1

1.1 Collider Detector at Fermilab (CDF) Overview 2

1.2 Intermediate Vector Bosons 4

2 Apparatus 7

2.1 Beam Beam Counters 7

2.2 Vertex Time Projection Chambers 8

2.3 Central Tracking Chamber 9

2.4 Superconducting Solenoid Coil 10

2.5 Central Electromagnetic Calorimeter 10

2.5.1 Structure 10

2.5.2 Gain Monitoring and Mapping 12

2.6 End Plug Electromagnetic Calorimeter 13

2.7 Forward Electromagnetic Calorimeter 15

2.8 Central and Endwall Hadron Calorimeter 16

2.9 End Plug Hadron Calorimeter 16

2.10 Forward Hadron Calorimeter 17

3 Performance of the End Plug Electromagnetic Calorimeter 18

3.1 Beam Test in 1985 18

3.1.1 Experimental Setup 18

3.1.2 Source Capacitance of the Detector and Charge Amplifier Gain 19

3.1.3 Performance of the Calorimeter 21

3.1.4 Gas Gain Monitoring 26

3.2 Electromagnetic Component Identification in the Plug Region 27

4 Pbar-P Collision Run in 1987 31

4.1 Readout System 31

4.2 Online Control Systems 32

4.3 Trigger System 32

4.4 Trigger for the W Boson Detection 33

4.5 Offline analysis overview 34

5 Data Reduction for W Boson Study 35

5.1 Electron Clustering Algorithm 35

5.2 Missing Transverse Energy 36

5.3 Data Reduction 36

5.4 $W \rightarrow e \nu$ Sample 39

5.5 Background Estimation 40

6 Results and Discussion 42

6.1 W Boson Production Cross Section 42

6.2 Transverse Mass Distribution of the W boson 44

7 Conclusions 46

Appendix A CDF Collaboration

Appendix B The Weinberg-Salam Standard Model

Appendix C Neutron Problem of the Gas Calorimeters

Appendix D Luminosity Determination in CDF

Appendix E Electromagnetic shower simulation in CDFSIM

References

Table Captions

Figure Captions

CHAPTER 1

Introduction

This thesis describes the structure and characteristics of CDF (Collider Detector at Fermilab) detector, and production cross section for charged intermediate vector bosons ($W^{\pm}$) and its decay properties observed at 1987 collision run with its identification procedure.

The W bosons are produced by the Drell-Yan mechanism [1-1] as a lowest order process; a quark and an antiquark annihilation. The first order cross section is directly predicted from the quark momentum distributions in the proton (structure functions) and the weak coupling constant[1-2]; and the corrections of order α_s to these cross sections have also been calculated[1-3]. From the predicted shape of the structure functions one expects an approximate three-fold increase in the W boson production cross section at the Tevatron energy of 1.8 TeV compared to the CERN collider energy of 630 GeV.

During the collision run, the data corresponding to $\int Ldt = 32.4\ nb^{-1}$ were stored on magnetic tapes which were taken under several trigger conditions including "electron" triggers and "jet" triggers. To search for events which include an electron candidate with a large amount of missing transverse energy, there are two different analysis paths. One path focuses on finding isolated electrons requiring only minimum requirements on the quality of the missing transverse energy. An independent analysis path focuses on the quality of missing transverse energy, and requires subsequent loose electron cuts. In this thesis, the first path which focuses on finding isolated electrons is described.

The quantity described in this thesis is the production cross section times the branching ratio of the W to an electron and a neutrino, $\sigma \cdot B(W \rightarrow e\nu)$, at 1.8 TeV. The quantity depends on the mass of the top quark. Previous measurements of $\sigma \cdot B(W \rightarrow e\nu)$ at UA1 and UA2 are consistent with the theoretical predictions assuming a mass of 40 GeV for the top quark. The

analysis is based on the measurement of the energy of the electron and the quality of missing transverse energy which in the case of W decay corresponds to the transverse energy of the neutrino.

The thesis organized as follows: Chapter 1 is composed of an overview of the CDF detector and a review of the Intermediate Vector Boson productions. In chapter 2 details of the detector used in the W boson study are reviewed. In chapter 3 details of the end plug electromagnetic calorimeter are described. In chapter 4 trigger and readout systems used in the 1987 collision run are reviewed. In chapter 5 a data reduction stream including background estimation for W boson study is described. In chapter 6 the results obtained in the chapter 5 are compared to the theoretical predictions, and conclusions are presented in chapter 7.

1.1 Collider Detector at Fermilab (CDF) Overview

The Collider Detector at Fermilab (CDF) is constructed as a general purpose detector for new physics research at high energy region[1-4]. Protons and antiprotons are accelerated in the same beam pipe to an energy of 900 GeV and collisions occur at the center of the CDF detector. The accelerator is called Tevatron, in which superconducting magnets are used. The CDF collaboration is international, with members from universities and laboratories in Japan, the U.S. and Italy. A list of the collaboration is given in Appendix A.

A perspective view of the detector is shown in Fig. 1-1-1. The CDF detector is constructed such that it surrounds the interaction region from 2° to 178° in polar angle and 360° in azimuthal angle. A cut view along the beam direction is shown in Fig. 1-1-2. The detector is divided into three regions in polar angle coverage; central region, plug region and forward/backward region, each covering 37°-90°, 11°-37° and 2°-11°, respectively. The 48 "wedge" modules of the central calorimetry (electromagnetic and hadron) form four C-shaped "arches" around the 3 m diameter 5 m long, 1.5 Tesla superconducting coil. The coil thickness, expressed in radiation length is 0.85 X_0. The endplug electromagnetic calorimeters are located in

the essentially uniform solenoidal field. The steel plates of the endplug and endwall hadron calorimeters form part of the solenoid flux return path.

Calorimetry plays an important role in the CDF detector by providing the basic information in the detection of quark and gluon jets and by giving a good measurement of the energy of electrons, and in some case, an indirect measurement of neutrino transverse momentum. The CDF calorimeters are segmented into about 5,000 "towers" or solid angle elements, and each calorimeter is constructed so that each "tower" or solid angle element point at the interaction region (tower geometry). The segmentation of the CDF calorimetry is shown in Fig. 1-1-3. In the central region, each calorimeter is segmented as $\Delta\eta$=0.09 in polar direction and $\Delta\phi$=15° in azimuthal direction. In the plug and the forward/backward region, each calorimeter is segmented as $\Delta\eta$=0.09 (partially $\Delta\eta$=0.045) in polar direction and $\Delta\phi$=5° in azimuthal direction. The calorimeters are all of the sampling type. The EM calorimeters contain lead sheet as absorber, whereas the hadron calorimeters use steel plates. The active medium is scintillator in the central region calorimeters (central electromagnetic, central hadron and wall hadron), and is proportional tube chambers with cathode pad readout in the plug and forward calorimeters (plug electromagnetic, plug hadron, forward electromagnetic and forward hadron). The proportional tube chamber calorimeters provide not only the tower (cathode pad) signals, but also some longitudinal information. The sum of wire signals, either from a section of a chamber or from a full chamber are read out and the detailed information about longitudinal shower development coming from these wire sums is very useful, both for diagnostic purposes, and for physics analysis, whenever particles are isolated.

The tracking systems are designed to measure charged particle tracks over the full solid angle. In the central region inside of the solenoid magnet, the momentum of particles is also measured. The tracking system used in this thesis are Vertex time projection chamber (VTPC) and Central tracking chamber (CTC). The VTPC consists of 8 modules of time projection chamber and finds the z-position of collision point. It measures charged particle multiplicities over a large solid angle ($-3.5 < \eta < 3.5$). The CTC is a large cylindrical drift chamber to measure

the trajectories and momenta of charged particles in the 1.5 T magnetic field. The momentum resolution at $\theta = 90°$ is expected to be $dPt/Pt = 0.003\ Pt$ (Pt in GeV/c).

Details of the calorimeters and tracking systems mentioned above will be described in chapter 2.

1.2 Intermediate Vector Bosons

The $W^{\pm}$ and Z^0 bosons described in the unified theory of weak and electromagnetic interactions[1-5] (see Appendix B) were observed through their leptonic decay modes in CERN proton-antiproton collision experiments[1-6],[1-7]. Several parameters observed in UA1 and UA2 for the $W^{\pm}$, Z^0 are shown in Table 1-2. In the theory leptons and quarks are classified into doublets by weak isospin as

$$\begin{bmatrix} \nu_e \\ e \end{bmatrix}_L, \quad \begin{bmatrix} \nu_\mu \\ \mu \end{bmatrix}_L, \quad \begin{bmatrix} \nu_\tau \\ \tau \end{bmatrix}_L,$$
$$\begin{bmatrix} u \\ d \end{bmatrix}_L, \quad \begin{bmatrix} c \\ s \end{bmatrix}_L, \quad \begin{bmatrix} (t) \\ b \end{bmatrix}_L, \qquad \text{... (1-2-1)}$$

where the subscript L indicates the left-handed components of the wavefunctions. In proton antiproton collisions, $W^{\pm}$ and Z^0 particles are produced by the Drell-Yan mechanism[1-1] and mainly detected by leptonic decay modes

$$\begin{aligned} u + \bar{d} &\rightarrow W^+ \rightarrow e^+ \nu_e , \\ &\rightarrow \mu^+ \nu_\mu , \\ u + \bar{u} &\rightarrow Z^0 \rightarrow e^+ e^- , \\ (d + \bar{d}) &\qquad\quad (\mu^+ \mu^-) . \end{aligned}$$

... (1-2-2)

The Feynman diagrams of the W production up to and including terms of order α_s are presented in Fig. 1-2-1. From the parton model description, the cross section for a reaction

$$p + \bar{p} \rightarrow W + X$$

... (1-2-3)

is given by

$$d\sigma(p + \bar{p} \rightarrow W + X) = \sum_{i,j} f_i^p(x_p)\, f_j^{\bar{p}}(x_{\bar{p}})\, d\hat{\sigma}(i + j \rightarrow W + X')$$

... (1-2-4)

where f_i and f_j are the parton distributions of species i and j, and x_p and $x_{\bar{p}}$ are the momentum fractions of i and j in p and $\bar{p}$, and $\hat{\sigma}$ is the cross section of a elementary reaction $i + j \rightarrow W + X'$. The parton distributions for u, d, gluon and s for several Q^2 are shown in Figs. 1-2-2 through 1-2-5 by using a parton distribution parametrization DO1[1-8].

The longitudinal momentum fractions x_p and $x_{\bar{p}}$ must satisfy the following relation by energy conservation

$$x_p \cdot x_{\bar{p}} \cdot s = M_W^2$$

...(1-2-5)

where s represents the proton-antiproton center of mass energy. By using the actual values for s ($1{,}800^2$ GeV^2) and M_W^2 ($\approx 80.5^2$ GeV^2), and putting that $x_p \approx x_{\bar{p}} \approx x$ in Eq. 1-2-5, we have a rough estimate for the momentum fraction of the partons involved in producing W particles

$$x \approx 0.04.$$

... (1-2-6)

The production cross section for $W^{\pm}$ and Z^0 are estimated to be

$$\sigma^{W\pm} \approx 18.0 \text{ nb},$$
$$\sigma^{Z0} \approx 5.6 \text{ nb},$$

... (1-2-7)

at $\sqrt{s} = 1.8$ TeV[1-3] by using the structure function of DO1. The production cross section times the branching ratio for a leptonic decay channel is estimated to be

$$\sigma \cdot B\,(W^+ + W^-) \approx 1.6 \text{ nb},$$
$$\sigma \cdot B\,(Z^0) \approx 0.18 \text{ nb},$$

... (1-2-8)

where the branching ratio to the leptonic channel is assumed to be 8.9%[1-3] for $W^{\pm}$ particle and 3.2 % [1-8] for Z^0 particle (assuming $m_{top} = 40$ GeV).

CHAPTER 2

Apparatus

In this chapter, some descriptions of the detectors used in the analysis of W events are presented. The detectors presented in this chapter are (a) Beam beam counter, which is used to determine the luminosity of each run, (b) Vertex time projection chamber, which is used to determine the collision point, (c) Central tracking chamber, which is used to determine the number of tracks and its transverse momentum, (d) Superconducting solenoid coil, which is used to generate 1.5 Tesla magnetic field, (e) Central electromagnetic calorimeter, which is used to determine the transverse energy of the particles detected, (f) other calorimeters, that is, Central hadron, Wall hadron, Plug EM, Plug hadron, Forward EM and Forward hadron calorimeters which are used to calculate the missing transverse energy of an event.

2.1 Beam Beam Counter

The counter surrounds the beam pipe and is 581.6 cm from the collision point. This system covers 360° in φ direction and from 0.317° to 4.47° in θ direction, corresponding to 5.89 to 3.24 in η respectively. Each counter covers approximately 1/4 of this rapidity range. The counter consists of a single layer of scintillator and is arranged in quadrants, with 4 counters per quadrant. The total number of counters is 16 in the forward direction and 16 in the backward direction, and are placed in front of the forward EM calorimeters. The counter have excellent timing properties (σ < 200 ps), and so provide the best measurement of the time of the interaction. A crude ($\pm$ 4 cm) measurement of the vertex position is also obtained from the timing. The BBC system of one side is shown in Fig. 2-1-1. The purposes of this system are

- Minimum bias trigger
- Luminosity monitor
- To reject beam-gas collisions
- To provide a good 'time zero' for the tracking chambers.

In particular, this system is used to determine the luminosity in the 1987 $\bar{p}$-p run. The method of the luminosity calculation is described in appendix C.

2.2 Vertex Time Projection Chamber

This detector surrounds the collision point and consists of eight modules of time projection chambers[2-1]. The 2.8 meter total length of the chamber covers well the long interaction region ($\sigma_z \approx 35$ cm). The VTPC chambers contain a total of 3072 sense wires for the measurement of track coordinates in r-z, where R is the radial distance from the beam and Z is the distance along the beam line from the center of the detector, and 3072 pads for the measurement of coordinates in R-φ. Fig. 2-2-1 is a schematic drawing of two octagonal VTPC modules. This detector is used to

1. Provide z-vertex position of each event,
2. Determine overall event topologies over a very wide range in polar angles (3.5° < θ < 176.5° or -3.5 < η < 3.5), and perform various charged particle measurements such as charged multiplicity $\langle N_{ch} \rangle_{total}$ and its η dependence $dN_{ch}/d\eta$,
3. Identify multiple interactions in the same beam crossing,
4. Provide intermediate angle tracking (10° < θ < 30°). In this angular region, VTPC information is used in conjunction with limited CTC information to provide both pointing to the energy cluster and momentum measurements. This is essential e/π^0 separation in the endplug calorimetry,
5. Provide forward angle tracking (3.5° < θ < 10°).

One module is divided into two region, and each has 15.25 cm long drift regions. Each endcap is divided into octants with 24 sense wires and 24 cathode pads in each octant. The chambers provide r-z information using TDC data from sense wire signals. Information on φ of tracks is obtained from cathode pad signals on a subset in chambers read out by a FADC (Flash Analog to Digital Converters) system. The sense wires and pads in some endcaps are instrumented with an analogue pulse height readout using FADC, so that dE/dx and φ information is available for particles produced at angles between 5° and 25° with respect to each beam axis. Adjacent modules have a relative rotation angle of φ=arctan(0.2) about the beam axis. For tracks passing through at least two modules, this eliminates inefficiencies near octant boundaries and provides φ information from small angle stereo.

2.3 Central Tracking Chamber

The Central Tracking Chamber[2-2] (CTC) is a 1.3 m radius 3.2 m long cylindrical drift chamber which gives precise momentum measurements in the angular region $40° < \theta < 140°$ ($-1 < \eta < 1$). The end view of the chamber is shown in Fig. 2-3-1. The CTC is located inside of the superconducting solenoid coil, surrounding the VTPC. The CTC has 84 layers of sense wires arranged into 9 super layers. There are two kinds of super layers. Five of the super layers are called axial layers, and each layer has 12 sense wires which are parallel to the beam line. The rest of the super layers are called stereo layers, and each layer has 6 sense wires. Both axial and stereo superlayers are divided into cells so that the maximum drift distance is less than 40 mm, corresponding to about 800 nsec of drift time. Each cell has 45° tilt to the radial direction to correct the Lorentz angle of the electron drift in the magnetic field. The sense wires of the half of the stereo layers (2-nd and 6-th layer from inside) have +3° angle to the azimuthal direction and the other two stereo layers (4-th and 8-th layer) have -3° angle, to measure the z-positions of the particles generated by collisions.

The CTC is operated under the 15 kG magnetic field, and Pt resolution is expected to be $\Delta Pt / Pt = 0.003 * Pt$ (in GeV at 90°). The resolution of the longitudinal coordinate (z) is expected to be 0.2 mm / sin 3° ≈ 4 mm or equal to the position resolution of the calorimetry. Summaries for the central tracking chamber such as mechanical parameters and performances are shown in Table 2-3-1 and 2-3-2.

Each sense wire is connected to a multiple hit TDC, with the option available to add analog information at a later date. The double track resolution is expected to be less than or equal to 5 mm or 100 nsec. Cancellation of the 1/t tail of sense wire pulses due to ion motion (up to 250 nsec) is accomplished by special filters in the electronics.

2.4 Superconducting Solenoid Coil

Precise momentum determination for charged particles produced in the central region is provided by the CTC, which is in a uniform 1.5 Tesla magnetic field oriented along the incident beam direction. The field is produced by a 3 meter diameter 5 m long superconducting solenoidal coil. The coil is made of 1164 turns of an aluminum stabilized NbTi/Cu superconductor, fabricated by the EFT (extrusion with front tension) method in which high purity alminum is friction welded to the superconducting wire during the extrusion process. The coil was designed to have no inner bobbin: the radially outward magnetic forces are supported by a thin aluminum-alloy cylinder outside the coil. Cooling is by forced flow of two-phase helium through aluminum tubes welded to the outer support cylinder. The overall radial thickness of the solenoid is 0.85 radiation lengths.

2.5 Central Electromagnetic Calorimeter

2.5.1 Structure

The calorimeter[2-3] consists of 33 layers of lead(1/8")-scintillator(1/4") pairs, and its effective radiation length is about 20 X_0. The calorimeter modules are placed outside the solenoid in a 24-fold configuration ($\Delta\varphi = 15°$), covering the range from $-1.1 < \eta < 1.1$ ($36° < \theta < 144°$) in polar direction and are divided into two along the beam axis. The segmentation in η direction is divided into 10 in each side as shown in Fig. 2-5-1. Each tower has projective geometry such that it points at the interaction region. The signal of each tower is read through two Y7 wave shifter sheets and acrylic light guides by two phototubes located outside of the hadron calorimeter. The efficiency of the portion where the wave shifter covers is low for any particles, and is called φ crack. It covers totally 5 % along φ direction in central region.

Energy resolution of the calorimeter is measured in a test beam and is given by

$$\sigma/E = 13.5\ \% / \sqrt{E}. \qquad \text{... (2-5-1-1)}$$

The position resolution of the module with only phototube information is about

$$\sigma\ (\varphi \text{ direction}) \approx \pm 7\ \text{cm} / \sqrt{E} \quad (E \text{ in GeV}),$$
$$\sigma\ (\eta \text{ direction}) \approx \pm 7\ \text{cm}. \qquad \text{... (2-5-1-2)}$$

A layer of wire proportional strip chamber is embedded in a module. The chamber is at 5.9 X_0 around shower maximum to measure the precise position of electromagnetic shower. The position resolution from the strip chamber is given by

$$\sigma\ (\varphi \text{ direction}) \approx \pm 5\ \text{mm}$$
$$\sigma\ (\eta \text{ direction}) \approx \pm 3\ \text{mm}. \qquad \text{... (2-5-1-3)}$$

The gain of a tower will be corrected by using the information from the wire strip chamber. Details of the mapping correction will be described in section 2.5.2. The summary of the central electromagnetic calorimeter is presented in Table 2-5-1.

2.5.2 Gain Monitoring and Mapping

To obtain the absolute calibration constant, ^{137}Cs sources with the strength of 3 mCi are used for the central EM calorimeter one per module[2-4]. The source can be moved through the module at a depth of 5.9 X_0, thereby illuminating nearby scintillators in all the towers in turn by remote control. The resulting DC currents, about 50 nA in the central EM calorimeter are measured to an rms accuracy of 0.3-0.4 %. The modules have been exposed to the 50 GeV electron beam, and the response was compared with the output from the ^{137}Cs source. It is possible to assume that the response ratio beam/source does not change with time. The assumption have been tested by repeated calibration of 3 modules over a period of about 5 weeks, as shown in Fig. 2-5-2-1. The result of this check is that the procedure has an accuracy of 0.6 % rms.

The response maps of central EM calorimeter are obtained for 5 wedge modules out of 50 modules by using 50 GeV electron beam[2-5]. For all 50 wedge modules, the electron beam was injected into the center of one tower as shown in Fig. 2-5-2-2 (a). For 5 wedge modules, the beam scanning was performed so as to obtain response map of a tower. The coordinates used are

$$x = R \tan\varphi$$
$$z' = R \cot\theta - z_0, \qquad \text{... (2-5-2-1)}$$

where R = 184.15 cm is the distance from the beam line to the imbedded strip chamber and z_0 is reference point at each tower (Fig. 2-5-2-2 (b)). The response is taken as the sum of phototube

pulse heights. The gain is higher about 10 % at around tower edge near φ crack, and 10 % lower at around η boundary of adjacent two towers as shown in Fig. 2-5-2-3. The map covers the full width of 24.1 cm in z', but x is limited to the region -22.5 cm < x < 22.5 cm, thus excluding the boundary region in φ, where the wavelength shifters are located. A common response map resulting from the scanning of five wedge modules describes the module response to about 1.5 % rms within the area -22.5 cm < x < 22.5 cm. The response map is parametrized as a function of x and z' as

$$S(x,z') = F_1 \cdot F_2(z') \cdot F_3(z') \cdot F_4(x,z') \cdot F_5(x,z') \ , \qquad \text{... (2-5-2-2)}$$

where

$$F_1 = p_1$$
$$F_2 = (1+p_2 \cdot \exp(p_3 \cdot |z'|)^{-1}$$
$$F_3 = (1+p_4 \cdot z' + p_5 \cdot z'^2)$$
$$F_4 = \cosh(x/\omega(z')), \ \omega(z')=\omega(0) \cdot F(z'), \text{ with } \omega(0)=p_6 \cdot p_7 \text{ and } F(z')=1+p_8 \cdot z' + p_9 \cdot z'^2$$
$$F_5 = (1+p_{10} \cdot \exp(|x| \cdot (p_{11}+p_{12} \cdot |z'|)))^{-1} \qquad \text{... (2-5-2-3)}$$

with 12 coefficients for each tower of towers 0 to 9 (For tower 0, $p_3 \cdot |z'|$ should be replaced to $p_3 \cdot z'$). The coefficients are presented in Table 2-5-2, and the typical fitting result of the parametrization is shown in Fig. 2-5-2-4. Within this area, the combined error from the absolute calibration (0.6 %) rms and from the deviations from the average map (1.5 %), are comparable to the energy resolution for 50 GeV electrons (2 %). The total rms error is of the order of 3 % for 50 GeV electrons within this area.

2.6 End Plug Electromagnetic Calorimeter

The end plug electromagnetic calorimeters[2-6] cover the η region from 1.1 (θ = 36°) to 2.4 (θ = 10°) with a segmentation of Δη=0.09 (1.41 < η < 2.40) or 0.045 (1.32 < η < 1.41), and Δφ=5° as shown in Fig. 2-6-1. Gas calorimeter is preferred as a shower counter in this region, because of the existence of the magnetic field and for the purpose of fine segmentation. The energy resolution of the gas calorimeters is not so good compared with the that the calorimeters made of scintillator. However, transverse momentum resolution is almost comparable with that of the central lead/scintillator electromagnetic calorimeter.

This detector consists of 34 layers of proportional counters and lead sheets. One layer consists of 2.7 mm lead sheet and proportional tube arrays sandwiched with two printed circuit boards as shown in Fig. 2-6-2. One is called pad board (Fig. 2-6-3), and another is called dummy board (or strip board from layer 6 through 15, Fig. 2-6-4 and 2-6-5). There is no pattern on dummy board, and it is directly connected to the ground. Total radiation length is 18.2 X_0 at θ=0° as shown in Table 2-6-1. This thickness corresponds to 0.88 absorption length including 0.5" iron plate at upstream from the interaction region as a gas vessel material. Resistive plastic tubes with 7 mm x 7 mm internal dimension are used as proportional counters. The surface resistance is chosen to be in a range of 60 kΩ/square to 100 kΩ/square. The resistive plastic tubes work as a conductor for low frequency pulses to make a d.c field, and high frequency pulses penetrate the tubes and it can be picked up at outer electrodes called pad. Proportional tube array is preferred also because it reduces the solid angle for secondary δ-rays which are sources of the fluctuation in energy deposit. The gold plated tungsten wire with 50 μm diameter is used as anode wire. The anode wires are supported by Y-shaped plastic pieces at both ends of each of the tubes as shown in Fig. 2-6-6. One quadrant plane consists of 156 tubes and each wire is connected to the high voltage bus via 100 Ω resistor to avoid cross talk of the signal. Only one high voltage line is connected to one quadrant plane.

The pads are etched out of the copper clad G-10 panels and face to the surface of the conductive plastic tubes. The signal picked up at the pad is transmitted to the signal line that is also etched at the other side of the G-10 panel via a through hole. Some pads are ganged together

to form a tower, and one tower is divided into three segments longitudinally. The first segment consists of 5 layers of proportional counters and lead sheets, the second segment consists of 24, and the third segment consists of 5. The second segment contains about 90 % of the total pulse height of an electromagnetic shower below 200 GeV (see for example Fig. 3-2-2). The event trigger was determined only by using this segment.

The two types of strip patterns are implemented around the shower maximum of the calorimeter. These are orthogonal with each other as illustrated in Fig. 2-6-4 and 2-6-5. The η strips with $\Delta\eta$=0.02 are implemented in odd-numbered five layers (7,9,11,13 and 15), and the φ strips with $\Delta\varphi$=1° are implemented in even-numbered five layers (6,8,10,12 and 14). The coverage of these strips is limited to a region of η=1.2 (θ=33°) to 1.84 (θ=18°), because of inferior energy measurement due to the leakage at the boundary around θ=37° and the smaller θ region is already finely segmented by the pads. All five θ and η strips are ganged together in depth forming well defined projected towers.

Basic parameters of the plug EM calorimeter are summarized in Tables 2-6-1 through 2-6-5. Details of the performance of the plug EM calorimeter is described in chapter 3.

2.7 Forward Electromagnetic Calorimeter

The forward electromagnetic calorimeters[2-7] are located approximately 6.5 m from the interaction point and enclose the beam pipe at either end of CDF. The calorimeters cover the small angle region between 2° and 10° in polar angle. Each calorimeter consists of 30 sampling layers, each of which is composed of a lead sheet and a chamber of gas proportional tubes with cathode pad readout. The sampling layers are constructed so that the insulating side of the cathode pad readout boards is bonded to the proportional tube walls using resistive epoxy. The lead sheets are 80 % of a radiation length thick and contain 6 % antimony for improved strength and flatness. The gas tubes are run at a nominal high voltage of 1900 volts, which is in the middle of the proportional region. The calorimeters use argon-ethane 50-50 for its gas mixture.

Each calorimeter is roughly 3 m on a side, 1 m deep, and weighs about 18 metric tons. The proportional tube layers in the calorimeter are divided into quadrants, each of which is a self-contained chamber which can be removed if repairs are required. The cathode pad geometry of a typical chamber is shown in Fig. 2-7-1. Each pad covers 0.1 units of pseudorapidity η and five degrees of azimuthal angle φ. The pads are ganged longitudinally into towers with two depth segmentations, both of which are 15 layers thick. There are 1440 pads per layer, resulting in a total of 5760 tower segments to be read out for both ends. The measured energy response of the calorimeter energy is linear up to 160 GeV and the measured energy resolution is approximately 25 % / $\sqrt{E}$ + 0.5 %. The position resolution varies between 1 mm and 4 mm depending on location in the calorimeter. The calorimeter offers good e/π discrimination, where typically the pion misidentification probability $f_{\pi\to e} < 0.5$ % with electron identification efficiency $\varepsilon > 90$ %.

2.8 Central and Endwall Hadron Calorimeter

The CDF central and endwall hadron calorimeter[2-8] covers the polar region between 30° and 150° and a full 2π in azimuth. The central calorimeters consist of 48 steel-scintillator layers with 2.5 cm sampling, and the endwall calorimeters consist of 48 steel-scintillator layers with 5.0 cm sampling. Each calorimeter module is divided into projective towers which covers approximately 0.1 units of pseudo-rapidity and 15° in azimuthal angle. This segmentation is fine enough that quark and gluon jets will normally spread over more than one tower. The central modules, covering polar angles between 45° and 135°, are 32 layers deep (Fig. 2-8-1). They are stacked into four free standing "C" shaped arches which can be rolled into and out of the detector. The endwall modules cover polar angles from 30° to 45° and from 135° to 150° (Fig. 2-8-2). They are plugged into cavities in the CDF magnet yoke and are parts of the flux return path.

2.9 End Plug Hadron Calorimeter

The end plug hadron calorimeters[2-9] cover the intermediate angular region from 10° to 30° to the beams and the corresponding pseudorapidity range of 1.3 to 2.4. The 2 inch steel plates of the end plugs are instrumented with pad proportional chambers in the 3/4" air gaps between the steel plates. The 2" steel plates of these calorimeters are in the flux return path of the solenoid. The wire chambers are designed with a high degree of modularity. Each detector plane is divided into 12 (30°) sectors in azimuth. Each sector is an independent chamber with its own gas volume. The principal readout consists of pads etched into standard printed circuit board forming one cathode plane. The calorimeters use argon-ethane 50-50 for its gas mixture.

2.10 Forward Hadron Calorimeter

The forward/backward hadron calorimeter[2-10] is composed of proportional tube chambers and steel plates. It is designed to cover a pseudorapidity region of $2.2 < \eta < 4.2$ with full azimuthal coverage with respect to the beam axis. Each of the forward and backward calorimeters is segmented into four independent sections ($\Delta\varphi = 90°$) which provide the necessary full azimuthal coverage. These calorimeter segments are each composed of 27 (213 cm x 213 cm x 5 cm) steel plates and 27 (204 cm x 196 cm x 2.5 cm) ionization chambers which are located between neighboring steel plates. The cathode surface of each of the ionization chambers has been segmented into 20 bins in pseudorapidity ($\Delta\eta = 0.1$) and 18 bins in azimuth ($\Delta\varphi = 5°$). The signals from each chamber pad at fixed η and φ are summed together to produce the total energy signal for a given projective tower. The calorimeters use argon-ethane 50-50 for its gas mixture resulting in an operating range of high voltage from 1.9 kV to 2.4 kV.

CHAPTER 3

Performance of the End Plug Electromagnetic Calorimeter

In this chapter, the performance of the plug EM calorimeter such as linearity and gas gain monitoring is described. The longitudinal shower shape observed in the calorimeter and its high voltage dependence is also presented. Some towers in the plug EM calorimeter have a large amount of source capacitance. The charge amplifier response with the source capacitance is also described.

3.1 Beam Test in 1985

3.1.1 Experimental Setup

The two plugs, east and west plugs have been brought to the M-Bottom beam line and tested in electron or negative pion beam. The energy of the beam was from 20 GeV to 200 GeV with the interval of 20 GeV. The both plugs were placed on a rotating stand and moved in the polar direction so that incident beam always came just like from the interaction point. These were also rotated in φ direction and total 2304 pads were scanned by using 100 GeV electron beam. The beam momentum was tagged by using 11 layers of PWC's (Proportional Wire Chambers) and bending magnets with an accuracy of 0.3 %. The beam position was also determined from the above PWC's. The η and φ encoders were connected to the gas vessel, and the actual position of the gas vessel was calculated from the output of these encoders.

The RABBIT (Redundant Analog Based Bus Information Transfer) system was used in the calibration run. Details of the RABBIT system will be described in chapter 4, but the system used in the beam test was a little different from that used in the $\bar{p}$-p collision run. One RABBIT

hutch contained one EWESIM which included 16-bit ADC, and some charge amplifier cards and one NIMBAT which transmitted timing signals called BEFORE and AFTER gates generated by a hand made NIM module called DINGGBAT. The BEFORE gate has been opening and closing all the time until the incident beam came in. When the beam came into the detector, the BEFORE gate started opening until the data taking finished. The AFTER gate started closing when the beam came in, and opened after 2.6 μsec. The time was changeable through the external gate generator.

Circuit diagram of the charge amplifier is shown in Fig. 3-1-1-1 with test pulse circuit (Fig. 3-1-1-2) which is common for 24 channels in a card. Output charge from the test pulse circuit is determined by the 100 pF capacitance and voltage from the voltage amplifier called VCAL. The charge stored in the capacitance is released when FET switch is opened or closed. The control signal that open or close the FET switch is called TCAL, and it was supplied from outer gate generator through NIMBAT.

3.1.2 Source Capacitance of The Detector and Charge Amplifier Gain

The rise time of a charge amplifier output was not fast enough due to the large magnitude of source capacitance of the calorimeter. The amount of source capacitance is determined by pad size and distance between the pad and the surface of the resistive plastic tubes; that is,

$$C = \varepsilon \frac{A}{d} ,$$

... (3-1-2-1)

where A is the area of pads and d is the distance between the surface of the plastic tubes and the pads, and ε is a dielectric constant of the material between the tubes and the pads. Typical source capacitance distribution is presented in Fig. 3-1-2-1 along η direction, and these values on some

rows are also shown in Table 3-1-2-1 through 3-1-2-3. These values are from about 20 nF through 120 nF for the 2 nd segment, 3 nF through 20 nF for the 1 st and 3 rd segments. The rms spread of the source capacitance along φ direction is not so small, because it is very difficult to control d in mass production. From the Table 3-1-2-1, the typical values of the spread is about 5 %.

The rise time of a charge amplifier is determined by the source capacitance and input impedance of the electronics, that is, $\tau = R_{in} C_{source}$. The rise time varies from 220 nsec to 1.3 μsec because the input impedance of the charge amplifier is about 11 - 12 Ω and the distribution of the source capacitance for the 2 nd segment pads are from 20 nF to 120 nF.

The gain of a charge amplifier card with source capacitance C_S is expressed as

$$G = G_0 \frac{G_{OPEN} C_F}{G_{OPEN} C_F + C_S} \left(1 - \exp\left(-\frac{t}{C_S R_{IN}}\right)\right)$$

... (3-1-2-2)

where G_0, G_{open}, C_F, R_{IN} and t denote the gain factor with no source capacitance, the open loop gain, the feedback capacitance (200 pF in mass production, Fig. 3-1-1-1), the input impedance and the sampling time, respectively.

The open loop gains and the input impedance of CARROT cards were measured by using ceramic capacitors of 22 nF, 47 nF, 68 nF and 100 nF as source capacitance. The measurement was made for a sampling time of 1.80 ± 0.02 μsec. The measurements were made on 24 channels of a card, and the data obtained were fitted with the equation 3-1-2-2. From the fitting, the obtained values of the open loop gain and input impedance are

$$G_{open} = 5180 \quad (280 \text{ in rms})$$
$$R_{IN} = 11.1\ \Omega \quad (0.6\ \Omega \text{ in rms}) .$$

... (3-1-2-3)

It is possible to estimate charge amplifier gain from the above equation if the source capacitance is known. For example, if the source capacitance is 100 nF, and the sampling time is 2.6 μsec, the gain will be reduced to about 85 % from the gain compared with the case of no source capacitance.

3.1.3 Performance of the Calorimeter

<Longitudinal Shower Shape>

Longitudinal shower profiles for several incident energies of the electron beam are presented in Fig. 3-1-3-1. They are fitted with the empirical function

$$y = A \cdot t^{\alpha} \cdot \exp(-\beta t), \qquad \text{... (3-1-3-1)}$$

where t is in radiation length. The energy dependence of the coefficients were obtained from the data taken by injecting electron beams of 20 GeV - 200 GeV to a point at θ=21.0° at 1.8 kV. Fitting results for these coefficients are shown in Fig. 3-1-3-2 for α and β. In Fig. 3-1-3-3 is shown these ratio α/β where the ratio α/β represents the position of shower maximum.

$$A = E\,\beta^{\alpha+1}/\Gamma(\alpha+1)$$
$$\alpha = (1.75 \pm 0.02) + (0.509 \pm 0.005)\ \ln E$$
$$\beta = (0.559 \pm 0.002) - (0.0104 \pm 0.0005)\ \ln E$$

(HV : 1.80 kV) ...1985.

... (3-1-3-2)

<Shower Leakage into the Plug Hadron Calorimeter>

Expected longitudinal shower leakage into the plug hadron calorimeter is estimated by fitting the shower tail with a function

$$y = A \cdot \exp(-Bt) \qquad \text{... (3-1-3-3)}$$

and by integrating the leakage part. The shower curve (Eq. 3-1-3-1) was not used for this estimation because the parameters α and β were slightly affected by setting high voltages due to gas gain saturation, as will be mentioned later.

Longitudinal shower leakage fraction is defined as follows

$$Y\,(\%) = \frac{\text{Estimated charge leaked from the detector}}{\text{Visible charge in the detector}} \cdot 100\,, \qquad \text{... (3-1-3-4)}$$

where the visible charge is defined as an integration value from $(0.722+0.514 \times 0.5)/\cos(\theta)\ X_0$ to $(0.722+0.514 \times 34.5)/\cos(\theta)\ X_0$ on the empirical shower function Eq. (3-1-3-1). Estimated longitudinal shower leakage fraction at θ=20° is plotted in Fig. 3-1-3-4 for several energies. The error bar at each point comes from the error of the fitting parameters A and B in Eq. (3-1-3-3). Expected longitudinal shower leakage at different θ points are also shown in the same figure. These are results of parametrization as a function of incident angle and energy in the form of

$$Y(\%) = P(\eta) \cdot E^{Q(\eta)} \qquad (E \text{ in GeV}),$$
$$P(\eta) = (-0.51 \pm 0.15) + (0.60 \pm 0.11)\,\eta$$
$$Q(\eta) = (0.46 \pm 0.09). \qquad \text{... (3-1-3-5)}$$

Longitudinal shower lost at the front steel plate is also estimated by integrating the empirical shower function from 0 X_0 to $(0.722 + 0.514 \times 0.5)/\cos(\theta)\ X_0$ and divided by visible charge defined previously. It is expressed as a function of energy and incident angle as

$$Y(\%) = P(\eta)/(E^{Q(\eta)}) \quad (E \text{ in GeV}),$$

$$P(\eta) = 9.7 - 2.5\,\eta$$

$$Q(\eta) = 1.07 + 0.08\,\eta$$

... (3-1-3-6)

and is shown in Fig. 3-1-3-5.

<Shower Shape for 100 GeV Electrons at Several High Voltages >

Shower curves for 100 GeV electrons at several high voltages are fitted with the empirical shower function of equation (3-1-3-1) and correlation between high voltages and fitting parameters are obtained. The high voltages were varied from 1.65 kV to 1.90 kV with an interval of 0.05 kV. The parameters α and β, and the ratio α/β are plotted in Fig. 3-1-3-6. These parameters have a slight supplied voltage dependence. For example, if the setting high voltage is changed 0.1 kV, α changes 1.3 % and β changes 1.6 % and the shower maximum shifts about 0.2 X_0.

To confirm the above results, the pulse height of each layer normalized at the shower tail (the last 8 layers) is plotted in Fig. 3-1-3-7 for 100 GeV electron data. The gas gain saturation effect is large at the front part of the shower because of high charge density.

<High Voltage Dependence of the Pulse Height>

The high voltage dependence of the pulse height (induced charge) is shown in Fig. 3-1-3-8. This curve is fitted with a function $Q = Q_0\exp(AV)$, where V is supplied high voltage in units of kV. The obtained values are

$Q_0=(0.175\pm0.002)\times10^{-4}$ (pC/100 GeV)

$A =(9.50\pm0.01)$ (kV^{-1})

... (3-1-3-7)

for the anode signal and

$Q_0=(0.127\pm0.001)\times10^{-4}$ (pC/100 GeV)

$A =(9.55\pm0.01)$ (kV^{-1})

... (3-1-3-8)

for the pad signal.

Though the calibration run was performed at 1.8 kV, the charge/energy ratio of the plug EM calorimeter should satisfy 125 pC/100 GeV for the trigger purpose. If the high voltage is 1.8 kV, total charge at 100 GeV is 370 pC for pad signal, and if the high voltage is 1.70 kV, total charge will become 140 pC. The value is a little higher than 125 pC, but it is easily correctable. Therefore the setting high voltage was changed to 1.70 kV in the 1987 collision run.

<Energy Resolution>

In Fig. 3-1-3-9 the energy resolution of the summed pad signals at 1.8 kV is plotted against a quality $1/\sqrt{E}$ and expressed as

$$\sigma/E\,(\%) = 28\,(\%)/\sqrt{E} \quad \text{... pad.}$$

... (3-1-3-9)

Though the operating voltage was set to 1.70 kV in the 1987 collision run, the above measurement was performed at 1.8 kV. To estimate the energy resolution at 1.70 kV, the energy resolution for several high voltages is plotted in Fig. 3-1-3-10. There is no significant change for energy resolution below 1.85 kV. Therefore we can use the same energy resolution curve which was obtained at 1.8 kV.

<Linearity Curve and Charge to Energy Conversion at 1.70 kV and 1.80 kV>

In the 1985 calibration run, the nonlinearity of the response against the incident energy was observed. The linearity curves at 1.8 kV are presented in figs. 3-1-3-11 and 3-1-3-12 for anode signals and 3-1-3-13 and 3-1-3-14 for pad signals for several angles. There are several factors that cause nonlinearity effect on the plug EM calorimeter. The main contribution to the nonlinearity effect is gas gain saturation. The longitudinal shower leakage into the hadron calorimeter and large magnitude of source capacitance with the limited slew rate of the charge amplifier are also the reasons of nonlinearity.

Unfortunately, linearity data at 1.7 kV were not taken in the calibration run. However, among the reasons that cause the nonlinearity effect, only the longitudinal shower leakage is a function of incident energy. The others are functions of total charge[3-1] deposited in the calorimeter or collected in a charge amplifier. Therefore we can predict linearity curve at a high voltage of 1.70 kV from the linearity curve taken at 1.8 kV. A predicted linearity curve at 1.7 kV is presented in Fig. 3-1-3-15 at $\theta = 21°$. A curve that determine the energy of a event from its observed charge is obtained by exchanging the axes of linearity curve, and the curve was refitted with quadratic function in the form for later convenience

$$\text{Energy (GeV)} = B \cdot q + C \cdot q^2. \qquad \text{... (3-1-3-10)}$$

where q is the corrected charge in pads. The predicted curves at 1.7 kV are shown in Fig. 3-1-3-16 and 3-1-3-17 only for pad and at several angles.

Scanning data were taken only by using 100 GeV electron beam. It is necessary to consider the behavior of the quadratic function along η direction. If the ratio of the coefficients (C/B) were parametrized as a function of incident angle, we can obtain one definite curve at any

position by using scanning data. The linearity data were taken at 4 different η positions (15.0°, 21.0°, 24.9° and 29.7°) in 1985 calibration run. We used these data to parametrize the ratio (C/B) of the coefficients. The data at 29.7° was not used because there is not full longitudinal coverage. The coefficient ratio (C/B) are plotted in Figs. 3-1-3-18 and 3-1-3-19 as a function of incident rapidity at 1.70 kV and 1.80 kV. These are parametrized as

$$\begin{aligned} C/B\ (\eta) &= (0.60 \pm 0.46)\times10^{-4} + (1.04 \pm 0.08)\times10^{-4}\eta \quad .. \text{ 1.70 kV}, \\ C/B\ (\eta) &= (0.97 \pm 0.44)\times10^{-4} + (0.67 \pm 0.25)\times10^{-4}\eta \quad .. \text{ 1.80 kV}. \end{aligned} \qquad \text{... (3-1-3-11)}$$

where the η region is restricted in $1.32 < \eta < 2.22$ where there is enough longitudinal coverage.

However, in the analysis stream, the linearity correction will be made in the last stage. Until then, only one constant is used as a conversion factor. The factor is chosen so that it is correct only for 100 GeV.

The linearity correction has to have the following form at the last stage,

$$E_{real} = B' E + C' E^2. \qquad \text{... (3-1-3-12)}$$

The relation between q and E is $q = 1.25\ E$. Finally, the following equation was obtained in the form with η dependence,

$$E_{REAL} = \frac{1}{1.01 + 0.013\,\eta} E + \frac{0.75\times10^{-4} + 1.30\times10^{-4}\,\eta}{1.01 + 0.013\,\eta} E^2. \qquad \text{... (3-1-3-13)}$$

The above equations actually satisfy $E_{real} = 100$ GeV at $E = 100$ GeV.

3.1.4 Gas Gain Monitoring

There are 6 tubes per each quadrant, and total 48 tubes are used to monitor the gas gain variation caused by the pressure, temperature and gas mixture change. The tubes of the same size and the same diameter of anode wires as those of the proportional counters in the calorimeter are used as monitor tubes as shown in Fig.3-1-4-1. The length of the monitor tube is about 10 cm and a Fe^{55} radioactive line source with the strength of 1 μ Ci is put to the surface of the monitor tubes that emit 5.9 keV X-rays. The pulse height distribution observed in the monitor tube is presented in Fig. 3-1-4-2. Tracing ability for 100 GeV electron beam events versus the output of the monitor tube is studied in 1984 beam test run and proved to be within 0.6 %; though the gas gain fluctuation itself is about 20 % in a day. The gas gain is monitored during the beam scanning continuously. The signal from the monitor tube goes to the LeCroy preamplifier TRA1000 and is sent to the LeCroy ADC 2280 system and read out by a computer, DEC PDP-11. Though the monitoring of the gas gain is achieved with about 1~2 % level, the absolute value measurement so that we can connect M-Bottom data to B0 collision run data is not so good, that is, $\pm$ 5%. Details of the gas gain monitoring is described in reference [3-2].

3.2 Electromagnetic Component Identification in the Plug Region

To identify electromagnetic signal such as electron or photon in the plug EM calorimeter, the following method called generalized χ^2 method is used. By using the electron events obtained in 1985 beam test run, a covariant matrix element is defined as

$$M_{ij}(E) = \frac{1}{N} \sum_{n=1}^{N} (X_i^{(n)} - \langle X_i(E) \rangle) (X_j^{(n)} - \langle X_j(E) \rangle), \qquad \text{... (3-2-1)}$$

where N, $X_i^{(n)}$ and $\langle X_i \rangle$ are the total number of electron events, the i-th variable for n-th electron events, and the average of the i-th variable for all electron events. For the k-th event which we want to examine, a single variable ζ_k is defined as

$$\zeta_k = \sum_{i,j=1}^{L} (X_i^{(k)} - \langle X_i(E) \rangle) (M^{-1}(E))_{ij} (X_j^{(k)} - \langle X_j(E) \rangle), \qquad \text{... (3-2-2)}$$

where L is total number of variables, M^{-1} is the inverse matrix of the M, $X_i^{(k)}$ and $\langle X_i \rangle$ are the i-th variable for k-th event and the average of the i-th variable for all the electron events. The variables used as X_i are

R_1 : Energy fraction that 1-st segment contains against total EM energy, E1/(E1+E2+E3).

R_2 : Energy fraction that 1-st segment contains against total EM energy, E2/(E1+E2+E3).

The distributions of R_1 and R_2 for various different energies are presented in Fig. 3-2-1 and 3-2-2, respectively. The mean of R_1 becomes smaller as energy becomes higher, but R_2 has the opposite tendency. The correlation between R_1 and R_2 for various energies are also presented in Fig. 3-2-3. For low energy electron the correlation is very strong. However it becomes weaker as incident energy becomes higher. The mean values and its σ's of R_1 and R_2 are parametrized as a function of energy by using 4-th order polynomials. The results of the fit are presented in Fig.3-2-4, and the fit parameters are presented in Table 3-2-1.

By using the means and σ's of R_1 and R_2, the matrix element of M is calculated from the Eq. 3-2-1. These values are parametrized as a function of energy by using 4-th order polynomials (Table 3-2-2) and are shown in Fig. 3-2-5. By using the matrix M as a function of

energy, generalized χ^2 values are calculated from Eq. 3-2-2 for the events of various energies, and are shown in Fig. 3-2-6. These distribution should be energy independent because the energy dependence is included in the matrix M. The probability distribution $P(\chi^2,\nu)$ for χ^2 is given by

$$P(\chi^2, \nu) = \frac{1}{2^{\nu/2}\,\Gamma(\nu/2)} (\chi^2)^{1/2(\nu-2)}\, e^{\chi^2/2} ,$$

... (3-2-3)

where ν is the number of degree of freedom. In the case of $\nu=2$, $P(\chi^2,\nu)$ becomes

$$P(\chi^2, \nu) = \frac{1}{2}\, e^{\chi^2/2} .$$

... (3-2-4)

The χ^2 distributions for the test beam data are fitted with a function $Y=e^{Bx}$. If the distribution of R_1 and R_2 have beautiful Gaussian shape, the fitted value B should be around -0.5. However the results are 0.74 ± 0.02 for various energy as is shown in Fig. 3-2-7. Since there seems no energy dependence about coefficient B, we will use 0.74 as a standard value to calculate electron efficiency.

For a threshold ζ_0, electron efficiency is defined as

$$\text{electron efficiency} = 0.74 \int_0^{\zeta_0} e^{-0.74\chi^2}\, d(\chi^2) .$$

... (3-2-5)

For example, if we choose $\zeta_0 = 4.0$ the electron efficiency is 94.8 ± 0.4 %.

Because of limited thickness of the plug EM calorimeters, it is necessary to study the ratio of the electron energies deposited in the electromagnetic calorimeter to the hadron calorimeter.

Though there are electron data from 20 GeV up to 200 GeV with the interval of 20 GeV, only 100 GeV and 200 GeV data are with hadron calorimeter high voltage on. The parameter E_{had}/EM_{tot} distribution is presented in figs. 3-2-8 and 3-2-9. The electron efficiency is almost 100 % if we apply the cut of $E_{had}/EM_{tot} < 0.1$.

CHAPTER 4

$\bar{P}$-P Collision Run in 1987

In this chapter, a readout system, an online control system and a trigger system used in the 1987 collision run are described. A trigger logic for detecting $W \rightarrow e \nu$ signals and the overview of an analysis stream for these signals are also presented.

4.1 Readout System

In the CDF calorimeter readout stream, RABBIT (Redundant Analog Based Bus Information Transfer) system[4-1] was used as photomultiplier output readout for central calorimeters and pad/wire/strip readouts for plug and forward/backward gas calorimeters. The RABBIT system consisted of 129 hutches mounted on the detector which handle all of the calorimeters, about 60,000 channels out of the 100,000 total of the CDF detector. One RABBIT hutch consisted of one EWE (Event Write Encoder) which contained 16 bit ADC, and one BAT (Before After Timing) as a control module and some charge amplifier[4-2] cards. The timing signal called C&S (Clear and Strobe) was supplied by external modules synchronized with the beam crossing. The BAT module supplied several sets of timing signals called BEFORE 0,1 and AFTER 0,1,2 (Fig. 4-1-1) after receiving C&S signals. Gate switches before sample and hold (S&H) capacitances in amplifier cards were controlled by the BEFORE and the AFTER signals. The energy of a event was recognized as a voltage difference between the two S&H capacitors. The voltages in the S&H capacitors were transmitted through bus lines on the backplane of the RABBIT hutch and go into a differential amplifier in the EWE. If this value was greater than a threshold value, this channel was digitized by 16-bit ADC mounted on the EWE. These data were sent to a module called MX, in which pedestal subtraction and multiplication of constants

from charge injection calibration and gas gain correction were applied. These correction factors were normalized around 1. The data were sent to the host computer and written to a magnetic tape.

4.2 Online Control System

The control of the reading of events, detector calibrations, and hardware diagnostics was by a computer process called RUN_CONTROL. Subsystems of the detector were isolated into separate DAQ systems for calibration or diagnosis by multiple copies of RUN_CONTROL executing simultaneously on one or several of the VAX processors in the CDF cluster of computers.

During physics data acquisition a single RUN_CONTROL process managed the DAQ hardware and the flow of data. Monitoring programs and data diagnostics as well as physics analysis and event selection filters accessed the data as independent "consumer processes" on either any VAX in the CDF cluster, or remotely via a network. For example, standard processes which accessed events during data acquisition were programs to identify bad electronics channels, to monitor trigger rates, and to accumulate luminosity information. A separate process ("Alarm and Limits") monitored the status of the detector.

Between data runs, calibration processes measured pedestal offsets and gains for the calorimeters, and measured constants for other systems. These data were then stored in large data bases, where they were extracted at the start of each data run for downloading to the detector subsystems. Other data bases have been created for storing data on external run conditions, integrated luminosity, etc., which were generated both by the monitoring consumer processes and by the Fermilab Control System (ACNET).

4.3 Trigger System

Both electromagnetic and hadron calorimeter towers were summed into trigger towers with a width in pseudo-rapidity of $\Delta\eta = 0.2$ and a width in φ of $\Delta\varphi = 15°$, in such a way that the entire calorimeter was divided into 42 (in η) by 24 (in φ) array. The trigger outputs from the calorimeters were transmitted to the CDF control room via dedicated cables, and were weighted by $\sin\theta$ to represent the transverse energy in the tower. The signals were DC levels (0-100 GeV in E_T correspond to 0-1 volts). The voltage levels stayed on these trigger cables until a Level 1 decision was made. If Level 1 was not satisfied in a given crossing, a reset was automatically sent in time for the next beam crossing. No deadtime was introduced by events which did not pass Level 1.

The Level 1 triggers required that the sum of E_T for all calorimeter towers which were individually over a lower threshold (typically 1 GeV) be greater than a higher threshold (typically 30-40 GeV). The two thresholds were programmable, and four (EM and hadron; single tower and sum of tower) such comparisons were made in a given beam crossing. The results of these comparisons were combined in a trigger "look-up" table with the beam-beam counter coincidence, muon triggers, a stiff track trigger from a fast hardware track processor, and other optional signals to generate the Level 1 decision to accept or reject the event. Different patterns could be rate-limitted so that minimum bias events, for example, could be taken intermixed with jet or electron triggers.

4.4 Trigger for the W Boson Detection

High transverse momentum electrons were triggered by two kinds of CDF trigger set, electron trigger and/or jet trigger. Both triggers were made by setting a threshold value for the sum of transverse energies over all trigger-towers whose transverse energies are above a threshold; 5-12 GeV for the electron trigger and 1 GeV for the jet trigger. The trigger-tower in the central EM calorimeter consists of two adjacent calorimeter-towers ($\Delta\eta = 0.2$, $\Delta\varphi = 15°$). The threshold values for the sum of transverse energies were changed in the range, 7-15 GeV for

the electron trigger and 20-45 GeV for the jet trigger, depending on the luminosity of a data taking run so that the trigger rate was kept about 1 Hz.

4.5 Offline Analysis Overview

Raw data are stored in the detector specific D-banks, such as CEMD for the central electromagnetic calorimeter or CHAD for the central hadron calorimeter. Since there are 7 major EM and Hadron calorimeters (CEM, CHA, WHA, PEM, PHA, FEM and FHA), there are 7 major D-banks corresponding to each calorimeter. The contents of the calorimeter D-banks are corrected ADC counts (amplifier gain correction or gas gain correction). In the subsequent analysis stream, all the D-banks are converted to the corresponding E-banks that contain energy of each tower or pad. Then all E-banks are merged to form one calorimeter tower bank called TOWE. Since the φ and η segmentation is a little different from detector to detector, there are 10 tower types in the TOWE bank. The energy clustering (electron clustering and jet clustering) algorithm are applied for this TOWE bank. In the case of electron clustering algorithm, for example, the algorithm finds a seed tower which has more than 3 GeV transverse energy. Looking around the seed tower, if there is a tower whose transverse energy is less than that of the seed tower and above 0.1 GeV, then the tower is recognized as forming a single cluster together with the seed tower. Details of the clustering algorithm is described in chapter 5. A bank called CALS stores the information of the cluster such as vertex corrected transverse energy, rapidity centroid, azimuthal centroid etc.

The track reconstruction is made for each tracking detector, and stored in a specific segment bank such as CTCS or VTCS. These information is merged to form a tracking segment bank called TRKS or TREX, in which the TOWE tower number to which a track points and track momentum and its directional cosine, etc., are stored.

The quality of missing Et information is stored in METS bank. This bank contains the missing Et value itself and its φ position and the sum of scalar Et's.

CHAPTER 5

Data Reduction for W Boson Study

In this chapter, an analysis stream to find events which include an isolated electron with a large amount of missing transverse energy is described. We first describe the electron finding algorithm to identify electron candidates in a event. Based on the energy cluster found by the algorithm, we search for events which include at least one isolated electron candidate by using the parameters of Isolation, E/p, Number of tracks pointing at the energy cluster and HAD/EM. Requiring a large amount of missing transverse energy, we obtain a $W \rightarrow e\nu$ sample. By a Monte Carlo simulation study, we estimate a background to $W \rightarrow e\nu$ from $W \rightarrow \tau\nu$, $\tau \rightarrow e\nu\nu$. We also estimate a background from QCD jet events from a distribution of the data itself.

5.1 Electron Clustering Algorithm

The electron (electromagnetic) clustering algorithm finds a seed tower whose electromagnetic transverse energy exceeds 3 GeV. If the transverse energy in an adjacent tower is lower than that for the seed tower but higher than a tower threshold transverse energy, 0.1 GeV, then the transverse energy in the adjacent tower is summed up to a cluster transverse energy. This process continues until no towers become satisfying these conditions. Since the lateral size of the electromagnetic shower is studied well in a test beam, the size of a cluster can be limited in a certain size. For the central EM calorimeter, the tower which is to be merged should be the next to the seed tower (seed $\pm$ 1) in the η direction. The number of towers in the φ direction is limited just 1 (seed tower itself). Because there is inactive area between the wedges caused by the wave length shifter bar, and it is possible to ignore the lateral shower leakage.

Thus the number of towers in a cluster is limited to within 3 (Fig. 5-1-1) in the central EM calorimeter. For the endplug and forward calorimeter, the cluster size is limited to 5 by 5.

5.2 Missing Transverse Energy

The quality of missing transverse energy of an event is defined as minus of the vector sum of the transverse energy over all EM and hadron cells of the calorimeter

$$E_t^{miss} = -\sum_{\text{all towers}} E_t \ ,$$

... (5-2-1)

corrected for the position of the vertex along the beam direction; excluding the six rapidity rings of the forward calorimeters closest to the beam ($2° < \theta < 3°$ and $177° < \theta < 178°$ or $\eta > 3.6$) which do not have complete azimuthal coverage due to the intrusion of the low-beta quadrupoles. Because of the neutron problem of the gas calorimeters in 1987 collision run (see appendix D), any cluster with less than 5 % electromagnetic energy is regarded as background. A study of a sample of jet triggers shows that 0.03 $\pm$ 0.03 % of real clusters would be eliminated by the above cut. There are some offset for the missing Et distribution, therefore offset corrections that was determined from the minimum bias events are applied.

5.3 Data Reduction

During the period of data taking run, approximately 4.8×10^5 events were recorded on tapes for the runs which include electron triggers and jet triggers. These amount of data correspond to an integrated luminosity of $\int Ldt = 32.4\ nb^{-1}$. After having eliminated runs with detector problems or recording problems, we obtained 4.1×10^5 events corresponding to 27.4 nb^{-1}.

The data is reduced by selecting events with electromagnetic clusters which a ratio of hadronic to electromagnetic energy less than 0.1. In addition for clusters with no associated charged tracks, the criterion that a transverse energy should be greater than 15 GeV are required. Approximately 5.9 x 10^4 events which passed the above requirement are recorded on the 134 DST's (Data Summary Tapes). Overall analysis stream is presented in Fig. 5-3-1. The number of events are reduced to 3.4 x 10^4 events by requirement of a single track association. In order to enhance electrons from W against backgrounds, we examined several quantities for the data on 134 DST's and Monte Carlo events simulated by the ISAJET 5.2[5-1] together with the CDF detector simulation programs. The quantities examined are

(a) Isolation, the ratio of total transverse energy inside a cone of R < 0.7 excluding the considering cluster to the cluster itself

$$I = \frac{Et\ (R<0.7) - Et\ (electron)}{Et\ (electron)} ,$$

... (5-3-1)

where R is the distance in the η and φ plane from the centroid of a EM cluster to the center of each tower

$$R = \sqrt{\Delta\eta^2 + \Delta\varphi^2} ,$$

... (5-3-2)

(b) HAD/EM, the ratio of hadronic energy to electromagnetic energy,

(c) Et, the transverse energy of electromagnetic cluster,

(d) E/p, the ratio of the transverse energy measured by the calorimeters to the transverse momentum measured by the central tracking chamber.

In the analysis stream for W boson study, a track reconstruction is required for only the tracks within ±15° in φ about the electromagnetic cluster. The minimum transverse momentum to be reconstructed is 2 GeV.

The distributions of these quantities are shown in Figs. 5-3-2 (a)-(d), where solid lines represent experimental data in 134 DST's, and dashed lines show Monte Carlo results. The simulated events show electrons from W bosons and the experimental data are mostly QCD jet events.

As shown in Fig. 5-3-2(a), the simulated electrons from W bosons are well isolated, while most of QCD events are not. The isolation I is a good parameter to separate $W \rightarrow ev$ events from QCD background events, providing a high efficiency for $W \rightarrow ev$ events and a large rejection power for QCD events. From the test beam data, the electron efficiency is greater than 95% at HAD/EM=0.05. This result is incorporated in the simulation program. (Fig. 5-3-2(b)). The distribution of transverse energies of electrons from W bosons forms a Jacobian peak at half of the W mass, while the QCD background decreases exponentially (Fig. 5-3-2(c)). Fig. 5-3-2(d) shows that the QCD backgrounds as well as electrons have a peak at E/p = 1.0, though the former has much broader distribution.

The distributions of the missing transverse energy divided by the square root of the sum of scalar Et's for the data in 134 DST's are presented in Figs. 5-3-3 (a) for x component and (b) for y component. From the figures, the missing transverse energy resolution is given by

$$\Delta Et^{miss} = (0.60 \pm 0.01)\sqrt{\sum_i Et^{(i)}} , \quad Et^{(i)} \text{ in GeV.}$$

... (5-3-3)

The above value is compared with the results of Monte Carlo two-jet simulations in which both jets have at least 20 GeV or 40 GeV transverse energy. These are presented in Figs. 5-3-4 (a) and (b) (each jet Et > 20 GeV) and in Figs. 5-3-5 (a) and (b) (each jet Et > 40 GeV). The widths of x component and y component of the quality of missing transverse energy divided by the square root of the sum of scalar Et's are 0.57 ± 0.01 for two-jet events with Et > 20 GeV and 0.59 ± 0.01 for Et > 40 GeV. These are in good agreement with the result (0.60 ± 0.01) for the data in 134 DST's.

Two sets of cuts, loose and tight cuts, are applied to the data in the 134 DST's to select events which include at least one electron candidate. These cuts are shown in Table 5-3-1 for both the central and plug regions. The tight cut positions are shown by arrows in Figs.5-3-2 (a)-(d).

The loose cuts reduced the number of events to 1560; among which 305 events are in the central region and 1255 in the endplug region. These events were recorded on 3 mini-DST's for the analysis of the W signals and their backgrounds. In this thesis only events in the central region will be discussed.

5.4 W → ev sample

Applying the tight cuts to the 305 events, we have obtained 53 events in the central region. So far we have not used one of the most powerful signatures for the W → ev decay, a quality of missing transverse energy. It is convenient to define a quantity

$$\chi = \frac{Et^{miss} \cdot Et^{miss}}{\Sigma Et} \quad , \qquad \text{... (5-4-1)}$$

where Et^{miss} is the quality of missing transverse energy and ΣEt is the sum of scalar Et's over all towers. A distribution of the χ for the events passing the tight cuts (53 events) is shown in Fig. 5-4-1. The data for χ less than 5 GeV is well fitted by a straight line in the semilog plot. The result of the fit is

$$f(\chi) = \exp(a+b\chi), \qquad a = 2.27 \pm 0.21, \quad b = -0.63 \pm 0.12. \qquad \text{... (5-4-2)}$$

This fit is used to estimate the QCD backgrounds to the W → ev events later. However, the slope is not so steep compared with the value expressed in Eq 5-3-3, that is, the slope from QCD jets should be $1/(2 \cdot 0.60 \cdot 0.60) \approx 1.4$. A cut $\chi > 5$ GeV is added to the tight cuts and we call it W cuts (Table 5-4-1).

The number of events which satisfy the W cuts is 22 and we call it a W sample. Figs. 5-4-2 shows the distribution of the parameters I, HAD/EM, Et, E/P for these 22 events. The distributions of the data are in good agreement with the results of the Monte Carlo simulations except for the energy-momentum matching, E/p (Fig. 5-4-2(d)). The energy was already corrected by a response map of the central calorimeters which was created from test beam data. The error in E/p is evaluated from the energy resolution of the central EM calorimeters, $0.14/\sqrt{E}$ (E in GeV), and the momentum resolution of the central tracking chamber, $0.003 \cdot Pt$ (Pt in GeV). Fig. 5-4-2 (d) shows that the momentum of electrons measured by the central tracking chamber is lower than the value determined by calorimetry. In Figs. 5-4-3 (a) and (b) are shown the difference of the positions measured by the central tracking chamber and by the strip chamber imbedded in the central EM calorimeter.

5.5 Background Estimation

Background contamination in the W sample (22 events) were estimated from the real data and the Monte Carlo simulations. The event sample (210 events), which passed the loose cuts with additional requirement of HAD/EM less than 0.05, was used to estimate QCD jet background contamination in the W sample. Fig. 5-5-1 shows a scatter plot of the isolation parameter I versus the missing Et significance χ for these events. The distribution shows a clear separation of W candidates from the background. The W candidates are populated in higher χ and lower I, while the background is located in lower χ and higher I.

A scatter plot of the electron transverse energy versus the missing transverse energy is also shown in Fig. 5-5-2. There is a strong correlation between the transverse energies and the

missing transverse energies of these events. Event display for the 22 events are shown in Figs. 5-5-3 (1) to 5-5-3 (22).

The background from two-jet events with one jet faking an electron and with the energy of other jet badly mismeasured is estimated by the same method as used in UA1[5-2]. Extrapolating the straight line in Fig. 5-4-1 from the region of $\not\!\!E_T < 5$ GeV to the region $\not\!\!E_T > 5$ GeV, we estimated the contamination from QCD jets as 0.7 ± 0.5 events. The Monte Carlo $W \rightarrow e\nu$ events are superimposed in the figure. In order to confirm this calculation, visual scans of the 22 events were made using the CDF event display program. After careful inspection, especially for the existence of additional high Pt tracks and lateral shower shapes in the strip chamber, we found one $Z \rightarrow e^+e^-$ and one QCD jet event. The event that is identified as $Z^0 \rightarrow e^+e^-$ (Run 7700, Event 6524, Fig. 5-5-3(20)) has two high Pt tracks (44.61 GeV/c and 36.44 GeV/c), but one track points at the tower 9 of the central EM calorimeter which does not have enough longitudinal coverage causing a high missing transverse energy. The event that is identified as QCD jet has multiple peaks in the lateral shower shape in the strip chamber, and is regarded as an overlap of π^+ and 3-4 π^0's. The remaining 20 events are consistent with $W \rightarrow e\nu$, (11 W^+'s and 9 W^-'s). Both estimations for QCD backgrounds are consistent with each other. An event list for all the 53 events passing the tight cuts are shown in Table 5-5-1. The two events found in the visual scans are indicated in Fig. 5-5-2.

The background from $W \rightarrow \tau\nu$, $\tau \rightarrow e\nu\nu$ is estimated as 1.4 ± 0.4 events using ISAJET 5.20. In Fig. 5-4-1(b) the contribution of the $W \rightarrow \tau\nu$, $\tau \rightarrow e\nu\nu$ is plotted as an upper curve, which is the sum of $W \rightarrow e\nu$ and $W \rightarrow \tau\nu$, followed by the $\tau \rightarrow e\nu\nu$ decay. Most of the τ background events have lower electron transverse energy and missing transverse energy in comparison with $W \rightarrow e\,\nu$ decays.

The backgrounds estimated in this section are summarized in Table 5-5-2. Subtracting 0.7 ± 0.5 QCD jet evnets, 1.4 ± 0.4 τ background and one $Z^0 \rightarrow e^+e^-$ from the 22 W candidates, we obtained 18.9 ± 4.7 $W \rightarrow e\nu$ events.

CHAPTER 6

Results and Discussion

We have obtained 22 events of the W sample and we have estimated backgrounds of 3.1 ± 0.6 events in the previous chapter. In this chapter, we evaluate the production cross section of W times its branching to $e\nu$ mode $\sigma \cdot B(W \rightarrow e\nu)$. An overall efficiency accepting $W \rightarrow e\nu$ events are estimated from Monte Carlo simulation studies and visual inspections by using the CDF event display program with color graphic terminals. The result is compared with the theoretically predicted values.

6.1 W Boson Production Cross Section

The production cross section for $W^{\pm}$ bosons in the process of $\bar{p}\,p \rightarrow W^{\pm} + X$ followed by the decay $W \rightarrow e\nu$ is evaluated from

$$\sigma \cdot B(W \rightarrow e\nu) = \frac{N^W}{\varepsilon \cdot \int L\,dt} \quad , \qquad \ldots (6\text{-}1\text{-}1)$$

where N^W is the measured number of $W \rightarrow e\nu$ decays after background subtraction, $\int L\,dt$ is the integrated luminosity and ε is the overall efficiency for detecting $W \rightarrow e\nu$ events. As described in the previous chapter, we have 18.9 ± 4.7 $W \rightarrow e\nu$ events after subtracting background contributions in the central region. The corresponding integrated luminosity is estimated to be 27.4 ± 4.1 nb^{-1}, where the error is a 15 % uncertainty in the BBC cross section. The details in estimating $\int L\,dt$ are described in Appendix C.

The overall efficiency ε can be divided into four factors, a track reconstruction efficiency in the central tracking chamber ε_{track}, a cut efficiency except the track reconstruction efficiency ε_{cut}, a geometrical acceptance ε_{geomet} and a trigger efficiency $\varepsilon_{trigger}$

$$\varepsilon = \varepsilon_{cut} \cdot \varepsilon_{track} \cdot \varepsilon_{geomet} \cdot \varepsilon_{trigger} \ . \qquad \text{... (6-1-2)}$$

The ε_{cut} includes the efficiencies applying the cuts of HAD/EM, Isolation and Et of electron. To estimate the efficiencies, we used the ISAJET Monte Carlo program V5.20 again in conjunction with a full simulation of the CDF detector V4.3. The ε_{cut} and ε_{geomet} are estimated by using 2,000 simulated events. The ε_{cut} is estimated to be 0.83 ± 0.01 (sta) where the error is statistical due to the limited number of the simulated events. The ε_{geomet} is estimated to be 0.50 ± 0.01 (sta) $\pm$ 0.05 (sys) where the first error is statistical and the second error is systematic due to the uncertainty in estimating it by using different sets of structure functions. The trigger efficiency $\varepsilon_{trigger}$ is estimated by using 800 simulated events and found to be $0.99^{+0.01}_{-0.05}$ (sta) where the error is statistical. However for the track reconstruction efficiency ε_{track}, we have not used the value estimated from the simulated events because we have found the ε_{track} is a little overestimated from a visual inspection. From the Monte Carlo simulation study, the track reconstruction efficiency ε_{track} is estimated to be 0.90 ± 0.01. However from the visual inspection for an event sample which satisfies the W cuts except $E/p < 1.8$ and $N_{track} = 1$, we found additional 5 events in which the track finding algorithm failed to reconstruct the transverse momentum of the electron correctly. If we assume the track reconstruction efficiency from visual inspection is 100 %, we can replace the track reconstruction efficiency of 0.90 ± 0.01 with 0.81 ± 0.07 (sta), that is, 22/(22+5). We thus estimate the overall efficiency ε to be

$$\begin{aligned}\varepsilon &= (0.83\pm0.01(\text{sta}))\cdot(0.81\pm0.07(\text{sta}))\cdot(0.50\pm0.01(\text{sta})\pm0.05(\text{sys}))\cdot(0.99^{+0.01}_{-0.05}(\text{sta})) \\ &= 0.33 \pm 0.03\ (\text{sta}) \pm 0.03\ (\text{sys}).\end{aligned} \qquad \text{... (6-1-3)}$$

The cross section at $\sqrt{s} = 1.8$ TeV is then calculated to be

$$\begin{aligned}\sigma\cdot B(W\rightarrow e\nu) &= (18.9 \pm 4.7)/((27.4 \pm 4.1)(0.33 \pm 0.03 \pm 0.03)) \\ &= 2.1 \pm 0.6\ (\text{sta}) \pm 0.4\ (\text{sys})\ \text{nb},\end{aligned} \qquad \text{... (6-1-4)}$$

where the first error includes the statistical error due to the number of events measured and the uncertainty in the track reconstruction efficiency, and the second error includes the systematic error due to the uncertainty of BBC cross section and the uncertainty in the geometrical acceptance ε_{geomet} by using different sets of structure functions.

The cross section is in agreement with the theoretical expectation of ≈1.6 nb which is interpolated to $\sqrt{s} = 1.8$ TeV from the results of Altarelli et al. [1-3] at $\sqrt{s} = 1.6$ and 2.0 TeV or 1.8 nb from the estimation of Eichten[6-1]. In both estimations, the branching ratio $B(W\rightarrow e\nu)$ is assumed to be 0.089[1-3] corresponding to Mt = 40 GeV. The theoretical prediction curve of Altarelli et al.[1-3] for the total production cross section for W particles are presented in Fig. 6-1-1 with obtained values at CDF, UA1 ($\sqrt{s}$ = 630 GeV)[6-2] and UA2 ($\sqrt{s}$ = 630 GeV)[6-3]

$$\begin{aligned}&\sigma\cdot B(W\rightarrow e\,\nu) = 0.63 \pm 0.04 \pm 0.10\ \text{nb} \quad \text{.. (UA1)} \\ &\sigma\cdot B(W\rightarrow e\,\nu) = 0.53 \pm 0.06 \pm 0.05\ \text{nb} \quad \text{.. (UA2).}\end{aligned} \qquad \text{... (6-1-5)}$$

All these results are in good agreement with the theoretically predicted values.

6.2 Transverse Mass Distribution of the W boson

We examined a transverse mass distribution of the 22 W candidates. The transverse mass is defined by the equation

$$M_t = \sqrt{2 \cdot E_t^e \cdot E_t^{miss} (1 - \cos\Delta\varphi^{ev})}$$

... (6-2-1)

where E_t^e is the transverse energy of electron, E_t^{miss} is the missing transverse energy, and $\Delta\varphi^{ev}$ is the difference in azimuth between the momentum vectors of electron and neutrino; the φ of neutrino is assumed to be the φ of the missing Et vector. The transverse mass distribution of the W candidates is plotted in Fig. 6-2-1 together with the Monte Carlo events. The data is in agreement with the expectation from a Monte Carlo simulation in which the W mass is assumed to be 83.4 GeV.

CHAPTER 7

Conclusion

The data corresponding to 27.4 nb^{-1} have been analyzed. By applying the cuts to select events which include a high Pt isolated electron and a large amount of missing transverse energy, we have obtained 22 $W \rightarrow ev$ candidates. The several distributions of the W candidates are in good agreement with the Monte Carlo simulation. Background estimations are made by the Monte Carlo simulation and the visual inspection using the CDF event display program. We have found 0.7 ± 0.5 events of QCD jets, 1 event of $Z^0 \rightarrow e^+e^-$ and 1.4 ± 0.4 events of $W \rightarrow \tau\nu$, followed by $\tau \rightarrow e\nu\nu$. Subtraction of background from the 22 W candidates yields 18.9 ± 4.7 $W \rightarrow ev$ events. The overall efficiency detecting the W bosons in the η range $-1.1 < \eta < 1.1$ is estimated to be 0.33 ± 0.03 (sta) ± 0.03 (sys) by the Monte Carlo simulation and the visual inspection. Subtracting the backgrounds and correcting for the efficiency, we have obtained $\sigma \cdot B(W \rightarrow ev) = 2.1 \pm 0.6$ (sta) ± 0.4 (sys) nb, where the first error includes statistical and the uncertainty in the track reconstruction and the second error includes systematic due to the uncertainty in the luminosity measurement and the uncertainty in the estimation of the geometrical acceptance by using different sets of structure functions. The result is in good agreement with the theoretically predicted values based on the Drell-Yan mechanism including higher order QCD corrections.

Appendix A

The CDF Collaboration

F.Abe[p], D.Amidei[c], G.Apollinari[k], G.Ascoli[g], M.Atac[d], P.Auchincloss[n], A.R.Baden[f], A. Barbaro-Galtieri[i], V.E.Barnes[l], E.Barsotti[d], F.Bedeschi[k], S.Belforte[k], G.Bellettini[k], J.Bellinger[q], J.Bensinger[b], A.Beretvas[n], P.Berge[d], S.Bertolucci[e], S.Bhadra[g], M.Binkley[d], R.Blair[a], C.Blocker[b], J.Bofill[d], A.W.Booth[d], G.Brandenburg[f], A.Brenner[d], D.Brown[f], A.Byon[l], K.L.Byrum[q], M.Campbell[c], R.Carey[f], W.Carithers[i], D.Carlsmith[q], J.T.Carroll[d], R.Cashmore[1], F.Cervelli[k], K.Chadwick[l,d], T.Chapin[m], G.Chiarelli[k], W.Chinowsky[i], S.Cihangir[o], D.Cline[q], D.Connor[j], M. Contreras[b], J.Cooper[d], M.Cordelli[e], M.Curatolo[e], C.Day[d], R.DelFabbro[k], M.Dell'Orso[k], L.DeMortier[b], T.Devlin[n], D.DiBitonto[o], R.Diebold[a], F.Dittus[d], A.DiVirgilio[k], R.Downing[g], G. Drake[d], T.Droege[d], M.Eaton[f], J.E.Elias[d], R.Ely[i], S.Errede[g], B.Esposito[e], A.Feldman[f], B.Flaugher[n], E.Focardi[k], G.W.Foster[d], M.Franklin[f,g], J.Freeman[d], H.Frisch[c], Y.Fukui[h], S.Galeotti[k], I.Gaines[d], A.F.Garfinkel[l], P.Giannetti[k], N.Giokaris[m], P.Giromini[e], L.Gladney[j], M.Gold[i], K.Goulianos[m], J.Grimson[d], C.Grosso-Pilcher[c], C.Haber[i], S.R.Hahn[l], R.Handler[q], D.Hanssen[d], R.M.Harris[i], J.Hauser[c], Y.Hayashide[p], T.Hessing[o], R.Hollebeek[j], L.Holloway[g], P.Hu[n], B.Hubbard[i], P.Hurst[g], J.Huth[d], M.Ito[p], J.Jaske[q], H.Jensen[d], R.P.Johnson[d], U.Joshi[n], R.W.Kadel[d], T.Kamon[o], S.Kanda[p], I.Karliner[g], H.Kautzky[d], K.Kazlauskis[n], E.Kearns[f], R.Kephart[d], P.Kesten[b], H.Keutelian[g], Y.Kikuchi[p], S.Kim[p], L.Kirsch[b], S.Kobayashi[2], K.Kondo[p], U.Kruse[g], S.E.Kuhlmann[l], A.T.Laasanen[l], W.Li[a], T.Liss[c], N.Lockyer[j], F.Marchetto[o], R.Markeloff[q], L.A. Markosky[q], M.Masuzawa[p], P.McIntyre[o], A.Menzione[k], T.Meyer[o], S.Mikamo[h], M.Miller[j], T.Mimashi[p], S.Miscetti[e], M.Mishina[h], S.Miyashita[p], H.Miyata[p], N.Mondal[q], S.Mori[p], Y.Morita[p], A.Mukherjee[d], A.Murakami[2], Y.Muraki[3], C.Nelson[d], C.Newman-Holmes[d], L.Nodulman[a], J.O'Meara[d], G.Ott[q], T.Ozaki[p], S.Palanque[4], R.Paoletti[k], A.Para[d], D.Passuello[k], J.Patrick[d], R.Perchonok[d], T.J.Phillips[f], H.Piekarz[b], R.Plunkett[m], L.Pondrom[q], J.Proudfoot[a], G.Punzi[k], D.Quarrie[d], K.Ragan[j], G.Redlinger[c], R.Rezmer[a], J.Rhoades[q], L.Ristori[k], T.Rohaly[j], A.Roodman[c], H.Sanders[c], A.Sansoni[e], R.Sard[g], V.Scarpine[g], P.Schlabach[g], E.E.Schmidt[d], P.Schoessow[a], M.H.Schub[l], R.Schwitters[f], A.Scribano[k], S.Segler[d], M.Sekiguchi[p], P.Sestini[k], M.Shapiro[f], M.Sheaff[q], M.Shibata[p], M.Shochet[c], J.Siegrist[i], V.Simaitis[g], J.K.Simmons[l], P.Sinervo[j], M.Sivertz[5], J.Skarha[q], D.A.Smith[g], F.Snider[c], L.Spencer[b], R.St.Denis[f], A.Stefanini[k], Y.Takaiwa[p], K.Takikawa[p], S.Tarem[b], D.Theriot[d], J.Ting[c], A.Tollestrup[d], G.Tonelli[k], W.Trischuk[f], Y.Tsay[c], K.Turner[d], F.Ukegawa[p], D.Underwood[a], C.vanIngen[d], R.VanBerg[j], R.Vidal[d], R.G.Wagner[a], R.L.Wagner[d], J.Walsh[j], T.Watts[n], R.Webb[o], T.Westhusing[g], S.White[m], V.White[d], A.Wicklund[a], H.H.Williams[j], T.Winch[q], R.Yamada[d], T.Yamanouchi[d], A.Yamashita[p], K.Yasuoka[p], G.P.Yeh[d], J.Yoh[d], F.Zetti[k]

CDF Member Institutions

[a] Argonne National Laboratory- [b] Brandeis University- [c] University of Chicago
[d] Fermi National Accelerator Laboratory- [e] INFN, Laboratori Nazionali di Frascati, Italy
[f] Harvard University- [g] University of Illinois- [h] KEK, Japan
[i] Lawrence Berkeley Laboratory-[j] University of Pennsylvania
[k] INFN, University and Scuola Normale Superiore of Pisa, Italy- [l] Purdue University
[m] Rockefeller University- [n] Rutgers University- [o] Texas A&M University
[p] University of Tsukuba, Japan- [q] University of Wisconsin

Visitors

[1] Oxford University, England- [2] Saga University, Japan
[3] ICRR, Tokyo University, Japan- [4] CEN, Saclay, France-
[5] Haverford College, Haverford, PA.

Appendix - B The Weinberg-Salam Standard Model

In the Weinberg - Salam standard model, The full Lagrangian is given by[6-1]

$$L = \sum_{f=u,d,\nu,e} [\, i \bar{f} \gamma^{\mu} (\partial_{\mu} - i g \frac{\tau^{\alpha}}{2} (\frac{1-\gamma_5}{2}) W_{\mu\alpha} - i \frac{g'}{2} (\frac{1-\gamma_5}{2}) Y_L B_{\mu} - i \frac{g'}{2} (\frac{1+\gamma_5}{2}) Y_R B_{\mu}) f \,]$$

$$- \frac{1}{4} \sum_{\alpha} (\partial_{\mu} W_{\nu\alpha} - \partial_{\nu} W_{\mu\alpha} + g \varepsilon_{\alpha bc} W_{\mu b} W_{\nu c})^2$$

$$- \frac{1}{4} (\partial_{\mu} B_{\nu} - \partial_{\nu} B_{\mu})^2 + (D_{\mu} \phi)^{+} (D^{\mu} \phi) - [\, - \mu^2 \phi^{+} \phi + \lambda (\phi^{+} \phi)^2 \,]$$

$$- \sum_{f = u,d,\nu,e} \Gamma_f \bar{f}_L f_R \bar{\phi} \quad + \quad \text{h.c.}$$

... B-1

where the covariant derivative is expressed as

$$D_{\mu} = \partial_{\mu} - i g \frac{\tau^{\alpha}}{2} W_{\mu\alpha} - i g' \frac{B_{\mu}}{2}$$

... B-2

According to the local gauge invariance, the Lagrangian for the coupling of the gauge bosons to the Higgs scalers is

$$[\, (\partial_{\mu} - i \frac{1}{2} g W_{\mu} \tau - i \frac{1}{2} g' I B_{\mu}) \phi \,] \cdot [\, \ldots \,]^{\dagger} - V (\phi^{+} \phi)$$

... B-3

and the potential is

$$V (\phi^{+} \phi) = - \mu^2 \phi^{+} \phi + \lambda (\phi^{+} \phi)^2$$

... B-4

Transforming the B_{μ} and $W_{\mu}{}^3$ as

$$B_{\mu} = \cos\theta_w A_{\mu} + \sin\theta_w Z_{\mu}$$
$$W_{\mu}{}^3 = \sin\theta_w A_{\mu} - \cos\theta_w Z_{\mu}$$

... B-5

and picking up the terms involving B_μ and $W_\mu{}^3$ from the equation B-3

$$-i\left[\frac{g}{2}W_\mu^3\tau_3+\frac{g'}{2}I\,B_\mu\right]\phi$$

$$=-i\left[A_\mu\left(g\sin\theta_w\frac{1}{2}\tau_3+g'\cos\theta_w\frac{1}{2}I\right)+Z_\mu\left(g'\sin\theta_w\frac{1}{2}I-g\cos\theta_w\frac{1}{2}\tau_3\right)\right]\phi$$

... B-6

where θ_w is the Weinberg angle. It is possible to choose the vacuum expectation value for complex scaler fields as follows

$$\phi=\phi_{vac}=\begin{bmatrix}0\\ \frac{v}{\sqrt{2}}\end{bmatrix}$$

... B-7

and if

$$g\sin\theta_w=g'\cos\theta_w \quad (\text{or } \tan\theta_w=g'/g),$$

... B-8

the field A_μ remains massless.

The part of B-3 that gives rise to non-zero masses for $W_\mu{}^1$, $W_\mu{}^2$ and Z_μ is

$$\left[\left[\frac{g}{2}\begin{bmatrix}0 & W_\mu^1-iW_\mu^2\\ W_\mu^1+iW_\mu^2 & 0\end{bmatrix}+\frac{g\sin\theta_w}{2}\begin{bmatrix}(\tan\theta_w-\cot\theta_w)Z_\mu & 0\\ 0 & (\tan\theta_w+\cot\theta_w)Z_\mu\end{bmatrix}\right]\begin{bmatrix}0\\ \frac{v}{\sqrt{2}}\end{bmatrix}\right]$$

$$x\begin{bmatrix}\cdots\end{bmatrix}^+$$

$$=\frac{g^2v^2}{4}\left[W_\mu^+W^{\mu+}+\frac{1}{2\cos^2\theta_w}Z_\mu Z^\mu\right].$$

... B-9

where

$$W_\mu^\pm=\frac{1}{\sqrt{2}}(W_\mu^1\mp iW_\mu^2)$$

... B-10

are the fields of the charged vector bosons. Thus for the charged boson $W_\mu{}^+$, the mass is given by

$$M_w=\frac{gv}{2}$$

... B-11

and for the neutral boson Z_μ the mass is

$$M_z=\frac{gv}{2\cos\theta_w}=\frac{M_w}{\cos\theta_w}$$

... B-12

From the connection to the low-energy phenomenology via

$$\frac{G_F}{\sqrt{2}}=\frac{g^2}{8M_w^2}$$

... B-13

and the relation

$$g\sin\theta_w=e,$$

... B-14

the W mass is expressed as

$$M_w=\left[\frac{\pi\alpha}{\sqrt{2}\,G_F\sin^2\theta_w}\right]^2$$

$$\approx\frac{37.3}{\sin\theta w}\ \text{GeV/c}^2.$$

... B-15

Appendix C Luminosity determination in CDF[C-1]

The integrated luminosity is calculated as the number of BBC E•W coincidences divided by the part of the Pbar-P total cross section seen by the BBC. The average luminosity is just this number divided by the live time. The BBC cross section can be measured in the standard fashion outlined in the run plan by simultaneously measuring the BBC rate and the total Pbat-P cross section using the Forward Silicon. Unfortunately, it is not done successfully during the past run, so it is necessary to estimate the cross section only by using the information from BBC.

In order to estimate the BBC cross section, the total cross section must be broken up into its various components, elastic, diffractive and hard core (inelastic minus single and double diffractive), and the BBC acceptance for each determined. The acceptance used here are those determined from the simulation using a Monte Carlo simulation program developed in the Rockefeller University.

To estimate the total cross section at $\sqrt{s}$ = 1800 GeV, the predictions from the recent literature have been used. These predictions span a range of only 74 mb to 80 mb where both extremes come from a paper by Block and Cahn[C-2]. The smaller value is arrived at by extrapolating from lower energy data and assuming that the cross section is asymptotically constant at very high energies by locally proportional to $\log^2 s$, while the larger value results from assuming the cross section to continue to evolve proportionally to $\log^2 s$. Taking the mean of these two values the total cross section is estimated to be

$$\sigma_{tot} = (77 \pm 6) \text{ mb} \qquad \text{... (C-1)}$$

where the error is chosen simply to allow the value to comfortably span the entire range of the predictions.

Next the elastic cross section is assumed to be as follows. UA4 has measured[C-3] the ratio σ_{el}/σ_{tot} at a center of mass energy of 546 GeV. They find $\sigma_{el}/\sigma_{tot} = 0.215 \pm 0.005$. Taking the ratio of UA5 elastic and total cross sections, a value 0.194 at 200 GeV and 0.230 at 900 GeV are assumed. Another prediction is given by Goulianos[C-4] for $\sqrt{s}$ = 1800 GeV to be σ_{el}/σ_{tot} = 0.229. This gives

$$\sigma_{el} = (17.6 \pm 1.6) \text{ mb} \qquad \text{... (C-2)}$$

where the error results from the uncertainty in the total cross section above, and the uncertainty in the ratio.

Given the above values for σ_{tot} and σ_{el}, the inelastic cross section is given by

$$\sigma_{in} = \sigma_{tot} - \sigma_{el} = (59.4 \pm 4.7) \text{ mb} \qquad \text{... (C-3)}$$

The inelastic cross section itself breaks up into three components, hard core, s_o, and single and double diffractive, s_{sd} and s_{dd} respectively. UA5 has measured[C-5] the single diffractive cross section to be (7.8 ± 1.2) mb at 900 GeV. In CDF convention, this value should be multiplied by 2. From the analysis of BBC scalers by Giokaris and Goulianos[C-6], the single diffractive cross section is given by

$$\sigma_{sd} = (15.0 \pm 5.0) \text{ mb} \qquad \text{... (C-4)}$$

and the double diffractive cross section is given by

$$\sigma_{dd} = (4.2 \pm 1.0) \text{ mb} \qquad \text{... (C-5)}$$

where the error is assumed to be a conservative 25 %.

Using these values, s_o is expressed as

$$\sigma_o = \sigma_{in} - \sigma_{sd} - \sigma_{dd} = (40.2 \pm 6.9) \text{ mb}$$

... (C-6)

and, finally, using the Rockefeller Monte Carlo acceptances for the BBC we get

$$\sigma_{BBC} = 0.134\,\sigma_{sd} + 0.618\,\sigma_{dd} + 0.924\,\sigma_{o}\,.$$

... (C-7)

The integrated luminosity is calculated as

$$\int L\,dt = \frac{\text{Number of events observed at BBC}}{\sigma_{BBC}}\,.$$

... (C-8)

Appendix D Neutron Problem of the Gas Calorimeters

During the collision run especially in forward hadron calorimeter, many trigger events were observed than expected from the luminosity. These are now thought as events caused by slow neutron produced in the beam pipe or somewhere and comes into the gas calorimeters and it knocks out the proton through the following process;

n + p --> n + slow p (order 1 MeV),

and it would deposit of order 1/3 MeV energy in a gas per centimeter. For CDF gas calorimeters, the effect of that neutron is estimated as follows,

	PEM	PHA	FEM	FHA	CEM	CHA
# of layers	34	20	28	13	30	30
Equiv. μ "energy" (MeV)	250?	3,000?	250?	4,000?	300	2,200
Min. Ioni. / layer (MeV)	7.4	150	8.9	308	10	73
Sensing material	Gas	Gas	Gas	Gas	Scinti	Scinti
Sensing material thickness (mm)	7	10	7 ?	10	5	10
Energy loss of MIP (KeV) in a layer *	2.7	3.8	2.7	3.8	1,005	2,010
"Energy" from 1/3 MeV proton (GeV)	0.91	13.1	1.10	27.0	0.003	0.012

* 3.8 KeV / cm is assumed for the gas of Ar : ethane = 50 : 50.

Appendix E Electromagnetic shower simulation in CDFSIM[E-1]

The electromagnetic shower simulation in CDFSIM is based on the results of a beam test study carried out in 1984 by using the CDF endplug electromagnetic calorimeter. The structure of the endplug electromagnetic calorimeter is described in chapter 2. The calorimeter consists of 34 pairs of a proportional chamber and a lead sheet, and it enables us to study event by event shower profiles. The calorimeter was exposed to positron and positive pion beams whose energies were from 10 GeV to 200 GeV. Pad signals of a 30 degree sector and 34 anode signals of the proportional chambers were read out.

The longitudinal shower profile is fitted with the well-known function $y=A\cdot t^{\alpha}\cdot\exp(-\beta t)$, where t is in radiation length. A scatter plot of event by event α and β is shown in Fig. E-1. As shown in Fig. E-1, these two parameters seem to have strong positive correlation each other. The correlation factor $C_{\alpha\beta}$, which is defined by

$$C_{\alpha\beta} = \frac{<\alpha\beta>}{\sqrt{(<\alpha^2> - <\alpha>^2)\cdot(<\beta^2> - <\beta>^2)}} \qquad \text{... (E-1)}$$

was about 0.8 over all incident energy. Since event by event shower maximum is given by α/β, the positive correlation means that the shower maximum does not move so much but the width of the longitudinal shower profile varies event by event for incident particles with a constant energy.

The energy deposit of the k-th event to the i-th longitudinal segment of a calorimeter, E_{ik} is given by the following formula

$$E_{ik} = \int_{\Delta i} y_k(t)\,dt + R\cdot r_k\cdot\sqrt{\int_{\Delta i} y_k(t)\,dt} \qquad \text{... (E-2)}$$

where $y_k(t)$ is a shower profile for k-th event whose integration is normalized to the incident energy, Δi is an integration region of the i-th segment, r_k is a random number which follows Gaussian distribution with $\sigma=1$, $\mu=1$ and R is a detector dependent over all resolution parameter. When the energy deposit in the segment is small, Poisson like distributions are used as the fluctuation in the second term instead of Gaussian distribution. Correlation between energy deposits in segments causes the fluctuation of the first term. If the leakage behind the calorimeter is small enough, the energy resolution have nothing to do with the profile, but it is determined by R as $\sigma/E=R/\sqrt{E}$. Choosing the resolution parameter R for each calorimeter, we can use common shower profile for all detectors.

The event by event shower profile $y_k(t)$ is essentially determined by two parameters α_k and β_k. Both parameters can be decomposed to fixed terms and fluctuating terms.

$$\alpha_k = <\alpha> + \Delta\alpha_k$$
$$\beta_k = <\beta> + \Delta\beta_k \qquad \text{... (E-3)}$$

The mean value of the Gaussian fit mentioned above can be regarded as these fixed term $<\alpha>$ and $<\beta>$. Distributions of these fluctuating term should be consistent with test beam results and they should satisfy the correlation between α and β. In order to generate such pair of random numbers, the following procedure is carried out.

1. σ_α, σ_β and $C_{\alpha\beta}$ are calculated as a function of incident energy.
2. A 2 x 2 symmetric matrix M whose elements are σ_α^2 σ_β^2 and $C_{\alpha\beta}\sigma_\alpha\sigma_\beta$ is made.
$$M = \begin{bmatrix} \sigma_\alpha^2 & C_{\alpha\beta}\sigma_\alpha\sigma_\beta \\ C_{\alpha\beta}\sigma_\alpha\sigma_\beta & \sigma_\beta^2 \end{bmatrix}$$
3. Two eigenvalues and an unitary matrix are obtained by disgonalizing this matrix M.
$$D = \begin{bmatrix} d_1^2 & 0 \\ 0 & d_2^2 \end{bmatrix} = U^{\dagger}MU$$
4. Two independent random numbers are extracted from two Gaussian type distributions whose sigmas are equal to the square roots of the eigen values.
$$w = \begin{bmatrix} w_{1k} \\ w_{2k} \end{bmatrix} \qquad <w_1> = 0,\ <w_1^2> = d_1^2,\ <w_2> = 0,\ <w_2^2> = d_2^2$$

5. Transforming these two independent ramdom numbers by the unitary matrix, the correlated pair $\Delta\alpha_k$, $\Delta\beta_k$ is obtained.

$$\begin{bmatrix} \alpha_k \\ \beta_k \end{bmatrix} = Uw$$

For transverse profile of an EM shower, two components of Gaussian functions which have three parameters S_1, S_2 and A_1 are used.

$$P(r) = A_1 \cdot N_1 \cdot \exp\left(-\frac{r^2}{2 \cdot S_1^2}\right) + A_2 \cdot N_2 \cdot \exp\left(-\frac{r^2}{2 \cdot S_2^2}\right)$$

... (E-4)

where

r	:	distance from shower center,
S_1	:	narrow component of EM shower (cm),
S_2	:	wide component of EM shower (cm),
N_1	:	normalization factor for narrow component which is a function of S_1,
N_2	:	normalization factor for wide component which is a function of S_2,
A_1	:	relative intensity for narrow component,
A_2	:	relative intensity for wide component = 1 - A_1.

The narrow component may come from the hard part of the shower secondaries with high energy, and the wide one the soft part of the shower secondaries with lower energy. The depth dependence of S_1 and S_2 are assumed to be

$$S = (a + b \cdot X_0)\, X_{eq} / E_c,$$

... (E-5)

where X_0, X_{eq} and E_c are

X_0	:	distance in radiation length,
X_{eq}	:	equivalent radiation length of the calorimeter,
E_c	:	critical energy of the material in MeV.

Both parameters a and b are estimated from test beam analysis results as

	a	b
S_1	0.0	0.389
S_2	8.19	0.0

The above list shows only parameter S_1 depends on the depth. In parameter A_1, we assumed constant value 0.6.

Fig. E-2 shows j-crack response in CDFSIM program (A_1 = 0.6) compared with the test beam result. The same type of response for A_1 = 0.76 is given in Fig. E-3. Both case are in good agreement with the test beam results.

References

Chapter 1

[1-1] S.D. Drell and T-M Yan, Phys. Rev. Lett. 25, 316 (1970).

[1-2] C.Quigg, Rev. Mod. Phys. 49, 297 (1977).

[1-3] G. Altarelli, R.K. Ellis, M. Greco, and G. Martinelli, Nucl. Phys B246, 12 (1984)
G. Altarelli, R.K. Ellis, and G. Martinelli, Z.Phys. C27, 617 (1985)

[1-4] F. Abe et al., The CDF Detector: An Overview, Fermilab Pub-88/25/-E, submitted to Nucl. Instrum. Methods.
Design Report for the Fermilab Collider Detector Facility (1981).

[1-5] S. Weinberg, Phys. Rev. Lett. 19, 1264 (1967); A. Salam, Elementary Particle Theory: Relativistic Groups and Analyticity (Nobel Symposium No. 8), edited by N.Svartholm, Almqvist and Wiksell, Stockholm, 1968, p. 367.

[1-6] UA1 Collab. G. Arnison et al., Phys. Lett. 122B, 103 (1983).

[1-7] UA2 Collab. M. Banner et al., Phys. Lett. 122B, 476 (1983).

[1-8] D.W.Duke, J.F.Owens, Phys. Rev. D30, 49 (1984).

Chapter 2

[2-1] F. Snider et al., Nucl. Instr. and Meth. A268 (1988) 75.

[2-2] F. Bedeschi et al., Nucl. Instr. and Meth. A268 (1988) 50.

[2-3] L. Balka et al., Nucl. Instr. and Meth. A267 (1988) 272.

[2-4] S.R.Hahn et al., Nucl. Instr. and Meth. A267 (1988) 351.

[2-5] K. Yasuoka et al., Nucl. Instr. and Meth. A267 (1988) 315.

[2-6] Y. Fukui et al., Nucl. Instr. and Meth. A267 (1988) 280.

[2-7] G. Brandenburg et al., Nucl. Instr. and Meth. A267 (1988) 257.

[2-8] S. Bertolucci et al., Nucl. Instr. and Meth. A267 (1988) 301.

[2-9] CDF Design Report (1981) p100.

[2-10] S. Cihangir et al., Nucl. Instr. and Meth. A267 (1988) 249.

Chapter 3

[3-1] S.Kim. private communication.

[3-2] Y.Hayashide. Doctor thesis. "Characteristics of CDF endplug electromagnetic calorimeter". Univ. of Tsukuba. UTPP-26 (1986).

Chapter 4

[4-1] G.Drake, T.F.Droege, C.A.Nelson, K.J.Turner and T.K.Ohska, IEEE Trans. Nucl. Sc., MS-33 No.1 (1986) 92.

[4-2] G.Drake, T.F.Droege, S.R.Hahn, R.Van Berg, H.H.Williams, T.M.Liss, R.G.Wagner and S.Inaba, IEEE Trans. Nucl. Sc., MS-33 No. 1 (1986) 893.

Chapter 5

[5-1] F. Paige and S.D. Protopopescu, ISAJET Monte Carlo, BNL 38034 (1986)

[5-2] UA1 Collab. G.Arnison et al., Nuovo Cimento Lett. 44 (1985) 1.

Chapter 6

[6-1] E. Eichten, Fermilab-conf-85/178-T, May (1986).

[6-2] UA1 Collab. C.Albajar et al., Phys. Lett. 198B 271 (1987).

[6-3] UA2 Collab. J.A.Appel et al., Z.Phys. C30, 1 (1986).

Appendix C

[C-1] T.M.Liss, CDF Note No. 522.

[C-2] M.M.Block and R.N.Cahn, Phys. Lett., 188B, 143 (1987).

[C-3] M.Bozzo et al., Phys. Lett., 147B, 392 (1984).

[C-4] K.Goulianos, Private communication.

[C-5] R.E.Ansorge et al., Z. Phys. C, 33, 175 (1986).

[C-6] N.Giokaris and K.Goulianos, Private communication.

Appendix E

[E-1] Y.Hayashide and T.Kamon, CDF Note No. 287, June 28, 1985.

Table Captions

Chapter 1

Table 1-2 A summary of the quantitative results coming from the analysis of the W, Z particles in UA1, UA2 and CDF.

Chapter 2

Table 2-3-1 Mechanical parameters of the CTC.

Table 2-3-2 Performance specification of the CTC.

Table 2-5-1 Central electromagnetic calorimeter summary.

Table 2-5-2 Coefficients in the response function for towers 0 to 9.

Table 2-6-1 Material thickness of the plug EM calorimeter.

Table 2-6-2 The types and numbers of signals of the plug EM calorimeter.

Table 2-6-3 Longitudinal layer configuration of the plug EM calorimeter.

Table 2-6-4 Mechanical parameters of the plug EM calorimeter.

Table 2-6-5 Performance of the plug EM calorimeter.

Chapter 3

Table 3-1-2-1 Source capacitance distribution of a part of the plug EM calorimeter 2 nd segment.

Table 3-1-2-2 Source capacitance distribution of a part of the plug EM calorimeter 1 st segment.

Table 3-1-2-3 Source capacitance distribution of a part of the plug EM calorimeter 3 rd segment.

Table 3-2-1 Coefficients of 4-th order polynomials for R_1 mean and its sigma, R_2 mean and its sigma as a function of energy.

Table 3-2-2 Coefficients of 4-th order polynomials for the matrix element of M as a

function of energy.

Chapter 5

Table 5-3-1 Cuts for electron identification. Both the loose one and the tight one for the central region and the plug region are presented.

Table 5-4-1 Cuts for W identification (W cuts) for the central region. This is the same as the central tight cuts plus $\chi = E_t^{miss} \cdot E_t^{miss}/\Sigma E_t > 5$ GeV.

Table 5-5-1 A list of the events which pass the central tight cuts (53 events). There are 22 events of W candidates in the upper part of the list.

Table 5-5-2 W sample and estimated backgrounds.

Figure Captions

Chapter 1

Fig. 1-1-1 A perspective view of the CDF detector showing the central detector and the forward and backward detectors.

Fig. 1-1-2 A cut-away view through the forward half of CDF. The detector is forward-backward symmetric about the interaction point.

Fig. 1-1-3 Hadron calorimeter towers in one of eight identical η-φ quadrants ($\Delta\varphi = 90°$, $\eta > 0$).The heavy lines indicate module or chamber boundaries. The EM calorimeters have complete φ-coverage out to $\eta = 4.2$.

Fig. 1-2-1 The Feynman diagrams for the W production up to and including terms of order α_s in proton-antiproton collisions.

Fig. 1-2-2 The up quark distribution, $xu(x,Q^2)$, of Duke and Owens parametrzation (1984) with $\Lambda = 200$ MeV as a function of x for various Q^2. The solid, dashed, dot-dashed and dense dotted lines correspond to $Q^2 = 10^2$, 10^3, 10^4 and 10^5 GeV^2, respectively.

Fig. 1-2-3 The down quark distribution, $xd(x,Q^2)$, of Duke and Owens parametrization (1984) with $\Lambda = 200$ MeV as a function of x for various Q^2. The solid, dashed, dot-dashed and dense dotted lines correspond to $Q^2 = 10^2$, 10^3, 10^4 and 10^5 GeV^2, respectively.

Fig. 1-2-4 The gluon distribution, $xG(x,Q^2)$, of Duke and Owens parametrization (1984) with $\Lambda = 200$ MeV as a function of x for various Q^2. The solid, dashed, dot-dashed and dense dotted lines correspond to $Q^2 = 10^2$, 10^3, 10^4 and 10^5 GeV^2, respectively.

Fig. 1-2-5 The strange quark (sea) distribution, $xs_s(x,Q^2)$, of Duke and Owens parametrization (1984) with $\Lambda = 200$ MeV as a function of x for various Q^2. The solid, dashed, dot-dashed and dense dotted lines correspond to $Q^2 =$

10^2, 10^3, 10^4 and 10^5 GeV^2, respectively.

Chapter 2

Fig. 2-1-1 A beam's eye view of one of the beam-beam counter planes.

Fig. 2-2-1 Two of the eight Vertex Time Projection Chamber (VTPC) modules.

Fig. 2-3-1 An endplate of the Central Tracking Chamber (CTC) showing the arrangement of the blocks which hold the 84 layers of sense wires.

Fig. 2-5-1 Schematic of a wedge module of the CDF central calorimeter showing the coordinate system used for the response map.

Fig. 2-5-2-1 Reproducibility of the calibration procedure for four wedges. The arrow indicates the expected shift of + 0.22 % in the beam / source ratio due to the 30 year half-life of ^{137}Cs. The rms error is 0.6 %.

Fig. 2-5-2-2 (a) Reference points used for the response map.

Fig. 2-5-2-2 (b) Tower coordinate system used for response map.

Fig. 2-5-2-3 Typical raw data of response map with 50 GeV electrons.

Fig. 2-5-2-4 Typical three dimensional representation of the response function.

Fig. 2-6-1 Isometric view of a quadrant showing the projective pad tower structure and the longitudinal layers.

Fig. 2-6-2 Exploded view of a layer of the proportional tube array, the p.c. board with pad patterns, and the p.c. board for ground plane.

Fig. 2-6-3 Patterns of the outer pick-up electrodes, pad.

Fig. 2-6-4 Patterns of the outer pick-up electrodes, θ-strip.

Fig. 2-6-5 Patterns of the outer pick-up electrodes, φ-strip.

Fig. 2-6-6 Plastic anode wire support.

Fig. 2-7-1 The pad geometry of a chamber of a forward electromagnetic calorimeter at layer 10.

Fig. 2-8-1 A central hadron calorimeter module. A light guide is sketched: scintillators in successive layers are read from opposite θ-sides. For each tower light is collected by two symmetrical positioned guides.

Fig. 2-8-2 A endwall calorimeter module. Module side faces are equipped with steel tubes positioned on the center lines of the towers and used for insertion of linear γ sources. The movable point source is also schematically drawn: the source, moving inside a steel tube, traverses all the towers at a fixed longitudinal depth along scintillator centerlines.

Chapter 3

Fig. 3-1-1-1 A circuit diagram of a charge amplifier for pad readout.

Fig. 3-1-1-2 A circuit diagram of a calibration circuit of an charge amplifier card. It is common for 24 channels.

Fig. 3-1-2-1 Source capacitance distribution along η direction. The solid line represents the distribution for the 2 nd segment, the dashed line for the 1 st segment and the dot-dashed line represents the 3 rd segment.

Fig. 3-1-3-1 Longitudinal shower profile of various energy of electron beam.

Fig. 3-1-3-2 Parameters of empirical shower function $y=A \cdot e^{\alpha} \cdot \exp(-\beta t)$ as a function of incident energy at 1.8 kV. The upper curve is for α, and lower curve is for β.

Fig. 3-1-3-3 The ratio α/β at 1.8 kV. This quantity represents shower maximum position.

Fig. 3-1-3-4 Expected longitudinal shower leakage into the plug hadron calorimeter at various angles, ie. 15°, 20°, 25°, 30° and 35° as a function of energy.

Fig. 3-1-3-5 Expected longitudinal shower leakage lost at front iron plate at various angles, ie. 15°, 20°, 25°, 30° and 35° as a function of energy.

Fig. 3-1-3-6 High voltage dependence of the shower parameters α, β and α/β. Those parameters have a slight high voltage dependence because of gas gain saturation of a shower.

Fig. 3-1-3-7 Response of each layer normalized to the response at 1.65 kV. The ratio

are further normalized for their absolute values using the ratios at the last eight layers.

Fig. 3-1-3-8 Pulse height as a function of operational high voltages for 100 GeV electron for anode signal and pad signal.

Fig. 3-1-3-9 Energy resolution measured in pad at 1.8 kV.

Fig. 3-1-3-10 Energy resolution for 100 GeV electron as a function of operational high voltages measured in pad.

Fig. 3-1-3-11 Energy dependence of calorimeter response at 1.8 kV for anode signal. The curve is fitted with a function $y=B\cdot E+C\cdot E^2$. The upper left curve is a linearity curve at $\theta = 15°$, and the upper right curve is a deviation from the linear line $y=B\cdot E$. The lower left curve is a linearity curve at $\theta = 24.9°$, and lower right curve is a deviation from the linear line $y=B\cdot E$.

Fig. 3-1-3-12 Energy dependence of calorimeter response at 1.8 kV for anode signal. The curve is fitted with a function $y=B\cdot E+C\cdot E^2$. The upper left curve is a linearity curve at $\theta = 21.0°$, and the upper right curve is a deviation from the linear line $y=B\cdot E$. The lower left curve is a linearity curve at $\theta = 29.7°$, and lower right curve is a deviation from the linear line $y=B\cdot E$.

Fig. 3-1-3-13 Energy dependence of calorimeter response at 1.8 kV for pad signal. The curve is fitted with a function $y=B\cdot E+C\cdot E^2$. The upper left curve is a linearity curve at $\theta = 15.0°$, and the upper right curve is a deviation from the linear line $y=B\cdot E$. The lower left curve is a linearity curve at $\theta = 24.9°$, and lower right curve is a deviation from the linear line $y=B\cdot E$.

Fig. 3-1-3-14 Energy dependence of calorimeter response at 1.8 kV for pad signal. The curve is fitted with a function $y=B\cdot E+C\cdot E^2$. The upper left curve is a linearity curve at $\theta = 21.0°$, and the upper right curve is a deviation from the linear line $y=B\cdot E$. The lower left curve is a linearity curve at $\theta = 29.7°$, and lower right curve is a deviation from the linear line $y=B\cdot E$.

Fig. 3-1-3-15 Energy dependence of the calorimeter response at 1.8 kV at $\theta = 21°$, and predicted linearity curve at 1.7 kV at the same position.

Fig. 3-1-3-16 Predicted curve at 1.7 kV for observed charge to energy conversion for pad signal. The upper left curve is at $\theta = 15.0°$, and the lower left curve is at $\theta = 24.9°$.

Fig. 3-1-3-17 Predicted curve at 1.7 kV for observed charge to energy conversion for pad signal. The upper left curve is at $\theta = 21.0°$, and the lower left curve is at $\theta = 29.7°$.

Fig. 3-1-3-18 Coefficient ratio C/B at 1.70 kV, where C and B are the coefficients of a fitting function $y=B\cdot q+C\cdot q^2$ to the curve of energy as a function of observed charge. The upper curve is for anode signal and the lower curve if for pad signal.

Fig. 3-1-3-19 Coefficient ratio C/B at 1.80 kV, where C and B are the coefficients of a fitting function $y=B\cdot q+C\cdot q^2$ to the curve of energy as a function of observed charge. The upper curve is for anode signal and the lower curve if for pad signal.

Fig. 3-1-4-1 A gas gain monitor tube located in the plug EM calorimeter. The same size of plastic tubes and anode wires are used. A 1μ Ci Fe^{55} radioactive line source is put on the surface of the plastic tube.

Fig. 3-1-4-2 Pulse height distribution observed in the gas gain monitor tube.

Fig. 3-2-1 R_1 (E1/(E0+E1+E2)) distribution for various energies of electron beams. The distribution becomes sharp as incident energy goes up.

Fig. 3-2-2 R_2 (E2/(E0+E1+E2)) distribution for various energies of electron beams. The distribution becomes sharp as incident energy goes up.

Fig. 3-2-3 Correlation between R_1 and R_2. The correlation is strong for low energy

electron beam.

Fig. 3-2-4 R_1 mean and sigma, R_2 mean and sigma as a function of incident energy. The dashed lines are parametrization in the form of 4-th order polynomials presented in Table 3-2-1.

Fig. 3-2-5 Matrix elements as a function of incident energy. The dashed lines are parametrization in the form of 4-th order polynomials as presented in Table 3-2-2.

Fig. 3-2-6 The generalized chi-2 distribution for various energies of electrons calculated from Eq. 3-2-2. The distributions are almost the same shape. The solid line is a fit function in the form of $Y=Ae^{B*E}$.

Fig. 3-2-7 The coefficient B distribution defined above as a function of incident electron energy. The B is energy independent.

Fig. 3-2-8 E_{had}/EM_{tot} distribution for 100 GeV electron.

Fig. 3-2-9 E_{had}/EM_{tot} distribution for 200 GeV electron.

Chapter 4

Fig. 4-1-1 Timing diagram of the RABBIT readout system. The normal BAT (used in the central and F/B calorimeter) and the plug BAT are slightly different and shown separately.

Chapter 5

Fig. 5-1-1 Electron clustering algorithm.

Fig. 5-3-1 Analysis stream of data reduction for W boson study.

Fig. 5-3-2 Distributions of parameters (a)Isolation, (b)HAD/EM, (c)Et of EM cluster and (d)E/p. The solid lines represent the data in 134 DST's and the dashed lines are the Monte Carlo simulation of W -> e ν events.

Fig. 5-3-3 A distribution of the missing transverse energy divided by the square root of the summation of the scalar Et $E_t^{miss}/\sqrt{\sum Et}$.

(a) The x component of the missing transverse energy divided by the square root of the summation of the scalar Et $E_t^{miss}/\sqrt{\sum Et}$.

(b) The y component of the missing transverse energy divided by the square root of the summation of the scalar Et $E_t^{miss}/\sqrt{\sum Et}$.

The curves are fitted with a Gaussian distribution. The σ in the graphs are both 0.60±0.01.

Fig. 5-3-4 Distributions of the missing transverse energy for 1,000 simulated two jet events in which both jet have at least 20 GeV transverse energy.

(a) The x component of the missing transverse energy divided by the square root of the summation of a scalar Et $E_t^{miss}/\sqrt{\sum Et}$. The σ of the distribution is 0.57 ± 0.01.

(b) The y component of the missing transverse energy divided by the square root of the summation of a scalar Et $E_t^{miss}/\sqrt{\sum Et}$. The σ of the distribution is 0.57 ± 0.01.

(c) The missing transverse energy divided by the square root of the summation of a scalar Et $E_t^{miss}/\sqrt{\sum Et}$.

(d) The scalar Et.

Fig. 5-3-5 Distributions of the missing transverse energy for 1,000 simulated two jet events in which both jet have at least 40 GeV transverse energy.

(a) The x component of the missing transverse energy divided by the square root of the summation of a scalar Et $E_t^{miss}/\sqrt{\sum Et}$. The σ of the distribution is 0.59 ± 0.01.

(b) The y component of the missing transverse energy divided by the square root of the summation of a scalar Et $E_t^{miss}/\sqrt{\sum Et}$. The σ of the distribution is 0.59 ± 0.01.

(c) The missing transverse energy divided by the square root of the summation of a scalar Et $E_t^{miss}/\sqrt{\sum Et}$.

(d) The scalar Et.

Fig. 5-4-1 The missing Et significance distribution (χ) of the events satisfying the tight curs. The straight line at lower χ is a fitting line in the form $y = A \cdot \exp(-\chi/2\sigma^2)$ by using the points of $\chi < 5$ GeV. The inner curves are Monte Carlo simulations The lower one is W -> e ν events and the upper one is the summation of W -> e ν events and W -> τ ν events, followed by τ -> e ν ν. The lower curve is normalized so that the area is equal to the 22 events.

Fig. 5-4-2 Distributions of the W sample (22 events, solid line) in comparison with the Monte Carlo events (dashed line). (a)Isolation, (b)HAD/EM, (c)Et, and (d)$(E/p - 1)/\sigma_{E/p}$.

Fig. 5-4-3 Distributions of the W sample (22 events, solid line) in comparison with Monte Carlo events (dashed line). (a)x(ctc)-x(strip) and (b)z(ctc)-z(strip).

Fig. 5-5-1 Scatter plot of isolation I versus normalized missing transverse energy χ for 210 events. There are 22 W -> e ν candidates in the area $0 < I < 0.1$ and $\chi > 5$ GeV clearly separated from QCD backgrounds.

Fig. 5-5-2 The missing transverse energy versus the electron transverse energy for the W sample (22 events). Error bars in the missing transverse energies are calculated as $\Delta E_t^{miss} = (0.60 \pm 0.01)\sqrt{\sum Et}$.

Fig. 5-5-3 (1)-(22)
Event display for the 22 W sample. Run 7170, event 72 (5-5-3(1)) is regarded as QCD two jet event, and Run 7700, event 6524 (5-5-3(20)) is regarded as Z^0 -> e^+e^- , in which one electron goes to central tower 9 which does not have enough longitudinal coverage.

Chapter 6

Fig. 6-1-1 Total production cross section for W bosons. The middle solid line represents theoretical predictions by Altarelli et al.[5-1]. The upper and lower solid lines are theoretical error obtained by varying the sets of parton distributions, the value of Λ and also the choice of $\alpha_s(\langle q_t^2 \rangle)$ or $\alpha(Q^2)$ in the first order terms. The data points are $\sigma \cdot B(W \to e \nu)$ observed at CDF, UA1[6-2] and UA2[6-3] divided by 0.089 which is estimated branching fraction of decay mode W -> e ν[1-3].

Fig. 6-2-1 Transverse mass distribution of the W sample (22 events) evaluated from the Et of electron and neutrino. The dashed line is ISAJET 5.20 W->e ν Monte Carlo events with CDF simulation program. (2,000 events).

Appendix E

Fig. E-1 Distribution of event by event α vs β for 100 GeV positron.

Fig. E-2 Average response of central EM calorimeter (Wedge 1) as a function of test beam position. The calorimeter was exposed to 50 GeV electrons. The horizontal axis is the beam position from the boundary of two wedges at the depth of the strip chamber. The solid line and open circles refer to CDFSIM V3.0 and test beam result, respectively. In CDFSIM V3.0, the following values are used; $S_1 = 0.61$, $S_2 = 2.2$, $A_1 = 0.6$ at the depth of the strip chamber.

Fig. E-3 Average response of central EM calorimeter (Wedge 1) as a function of test beam position. The calorimeter was exposed to 50 GeV electrons. The horizontal axis is the beam position from the boundary of two wedges at the depth of the strip chamber. The solid line and open circles refer to CDFSIM V3.0 and test beam result, respectively. In this case, $S_1 = 0.61$, $S_2 = 2.2$, $A_1 = 0.76$ are used at the depth of the strip chamber.

Table 1-2 Parameters for the Intermediate Vector Bosons.

	UA1	UA2	CDF
M_W (GeV/c^2)	$83.5\ ^{+1.1}_{-1.0} \pm 2.7$[a1]	$80.2 \pm 0.6 \pm 0.5$[b1]	
Γ_W (GeV/c^2)	≤ 6.5 (90 % C.L.)[a1]		
M_Z (GeV/c^2)	$93.0 \pm 1.4 \pm 3.0$[a1]	$91.5 \pm 1.2 \pm 1.7$[b1]	
Γ_Z (GeV/c^2)	≤ 8.3 (90 % C.L.)[a1]	< 5.6 (90 % C.L.)[b1]	
$\sin^2\theta_W$	0.194 ± 0.032[a1]	$0.232 \pm 0.003 \pm 0.008$[b1]	
ρ	$1.026 \pm 0.037 \pm 0.019$ [a1]	$1.001 \pm 0.028 \pm 0.006$[b1]	
$\sigma \cdot B(W \to e\nu)$ (nb)	$0.63 \pm 0.04 \pm 0.10$ (630 GeV) [a2]	$0.53 \pm 0.06 \pm 0.05$ (630 GeV) [b2]	$2.1 \pm 0.6 \pm 0.4$
$\sigma \cdot B(Z \to e^+e^-)$ (nb)	$0.071 \pm 0.011 \pm 0.011$ (630 GeV) [a2]	$0.052 \pm 0.019 \pm 0.004$ (630 GeV) [b2]	
R(*1)	$9.1^{+1.7}_{-1.2}$[a2]	$7.2^{+1.7}_{-1.2}$[b1]	
N_ν	≤ 5.9 (90 % C.L.)[a2]		

*1 $R = (\sigma \cdot B)_W / (\sigma \cdot B)_Z$

[a1] UA1 Collab. G. Arnison et al., Europhys. Lett. 1, 327 (1986)

[a2] UA1 Collab. C.Albajar et al., Phys. Lett. 198B, 271 (1987)

[b1] UA2 Collab. R. Ansari et al., Phys. Lett. 186B, 440 (1987)

[b2] UA2 Collab. J. A. Appel et al., Z. Phys. C 30, 1 (1986)

Table 2-3-1 Mechanical Parameters of the CTC

NUMBER OF LAYERS	84
NUMBER OF SUPER LAYERS	9
STEREO ANGLE	A S A S A S A S A
	0° +3° 0° -3° 0° +3° 0° -3° 0°
NUMBER OF SUPER CELLS	30 42 48 60 72 84 96 108 120
NUMBER OF SENSE WIRES/CELL	12 6 12 6 12 6 12 6 12
SENSE WIRE SPACING	10 mm in plane of wires
TILT ANGLE	45°
ENDPLATE	2" Aluminium
OUTER CAN	0.250" Aluminium
INNER SUPPORT CYLINDER	0.080" Carbon Fiber Reinforced Plastic
GAS	Argon-Ethane-Ethyl Alcohol
	(49.65 % : 49.65 % : 0.7 %)
DRIFT FIELD (E_0)	~1500 V/cm
DRIFT FIELD UNIFORMITY	dE_0/E_0 ~ 1.5 % (rms)

Table 2-3-2 Performance Specification of the CTC

GAIN	3×10^4
RESOLUTION	< 200 μm per wire
EFFICIENCY	> 0.98 per point
DOUBLE TRACK RESOLUTION	< 5 mm or 100 nsec
MAXIMUM DRIFT DISTANCE	35 mm
MAXIMUM HITS PER WIRE	> 7
STEREO ANGLE	±3°
Z RESOLUTION	< 0.200 mm / sin 3° ~ 4 mm
MOMENTUM RESOLUTION	dPt / Pt < 0.001 * Pt (in GeV at 90°)

Table 2-5-1 Central Electromagnetic Calorimeter Summary

Modules	
12/arch + 2 spare	50
Length	98 in.
Width	15° in φ
	(17.9 in. at 68+ in. from beam line)
Depth (including base plate)	13.6 in.
Weight	2 metric tons
Towers	
10/module	478
Length	Δη 0.11 (1/2 of width)
Thickness	18 X_0, 1 L_{abs} (+coil etc.)
Layers	20 - 30 lead
	21 - 31 scintillator
	1 strip chamber
Lead	1/8 in. alminum clad
Scintillator	5 mm SCSN-38 polystyrene
Wavelength shifter	3 mm Y7 UVA acrylic
Photomultiplier tubes (956 channels)	Hamamatsu R580 (1.5 in.)
Chambers	
Depth	5.9 X_0 (including coil)
Wire channels (64/module)	3072
Strip channels (128/module)	6130
Angular coverage	
θ	about 39° - 141°
φ	complete
Pseudorapidity	about ±1.1
Performance (high = 30+ GeV)	
pe/GeV	100+/tube
Energy resolution σ/E (GeV)	13.5 %/√E
Position resolution (high)	± 2 mm
Strip/wire PH correlation	8-10 %
Wire PH resolution (high)	± 25 %
Hadron rejection (at 50 GeV)	2-3 x 10^{-3}
without strip chamber information	

Table 2-5-2

COEFFICIENTS IN RESPONSE FUNCTION S(X,Z')

Parameter	Tower 0	Tower 1	Tower 2	Tower 3	Tower 4
p_1	1.00±0.001	1.00±0.001	0.998±0.001	1.00±0.001	0.999±0.001
p_2 ($\times 10^{-5}$)	1.71±0.77	3.43±3.40	0.106±0.124	9.36±7.50	14.6±21.5
p_3	-0.790±0.020	0.587±0.087	0.923±0.100	0.496±0.068	0.425±0.128
p_4 ($\times 10^{-3}$)	1.83±1.17	-0.832±0.087	-0.941±0.099	-0.357±0.090	-0.529±0.107
p_5 ($\times 10^{-4}$)	-5.52±0.04	0.00	0.00	0.00	0.00
p_6	44.7±0.4	48.5±0.5	47.7±0.5	45.7±0.4	41.6±0.3
p_7	1.00	1.00	1.00	1.00	1.00
p_8 ($\times 10^{-2}$)	1.170±0.08	0.146±0.059	0.196±0.062	0.586±0.054	1.140±0.064
p_9 ($\times 10^{-3}$)	0.721 ($\times 10^{-8}$)	0.349±0.066	0.097±0.067	0.722±0.062	1.69±0.07
p_{10}	3.08±.11x10^{-26}	3.06±.09x10^{-26}	4.25±3.59x10^{-19}	1.39±.03x10^{-18}	5.72±.22x10^{-13}
p_{11}	2.491±.001	2.490±.001	1.782±.036	1.737±.001	1.196±.002
p_{12} ($\times 10^{-3}$)	-1.68±0.21	-0.164±0.093	-1.28±0.13	0.876±0.067	-0.374±0.122

Parameter	Tower 5	Tower 6	Tower 7	Tower 8	Tower 9
p_1	0.998±0.001	0.999±0.001	1.00±0.002	1.00±0.01	1.00±0.001
p_2 ($\times 10^{-5}$)	3.15±0.58	33.9±27.5	114±117	45.8±40.1	589±7.8
p_3	0.539±0.008	0.406±0.072	0.287±0.094	0.364±0.077	0.350±0.0003
p_4 ($\times 10^{-3}$)	-0.369±0.123	-1.17±0.13	-1.16±0.16	-0.555±0.115	-4.66±0.26
p_5 ($\times 10^{-7}$)	0.00	0.00	0.00	0.00	-3.01±2.33
p_6	43.0±0.3	48.2±0.5	46.0±0.5	49.9±0.5	50.9±0.9
p_7	1.00	1.00	1.00	1.00	1.00
p_8 ($\times 10^{-2}$)	1.13±0.06	0.645±0.07	-0.431±0.07	0.956±0.08	-10.6±0.6
p_9 ($\times 10^{-3}$)	1.17±0.07	0.125±0.08	1.69 ($\times 10^{-10}$)	0.054±0.09	12.5±1.0
p_{10} ($\times 10^{-13}$)	5.72±.25	5.72±.22	5.72±3.04	5.71±2.89	5.66±2.76
p_{11}	1.199±.002	1.190±.002	1.212±.023	1.212±.022	1.212±.021
p_{12} ($\times 10^{-3}$)	-0.145±0.124	0.396±0.149	-0.123±0.121	-0.502±0.168	6.46±0.28

Note: Values of p_{10} and p_{11} are replaced to 8.96x10^{-4} and 0.384 for $|x| \geq 23.5$ cm, respectively.

Table 2-6-1 Material Thickness of the plug EM calorimeter

	Physical Thickness	Radiation Length	Pion absorption Length
Front Cover Plate : Fe			
(z = 173.99 ~ 175.26 cm)	12.7 mm	0.722 X_0	0.05971 λ^{π}_{abs}
Each Sampling Layer			
(z = 175.26 ~ 226.06 cm)			
Lead Panel (Ca : 0.065 %, Sn : 0.7 %)	2.69 mm	0.480 X_0	0.0134 λ^{π}_{abs}
Chamber Layer			
Cu-Clad G-10	1.6 mm	0.013 X_0	0.0033 λ^{π}_{abs}
Conductive Plastic Tube			
(Wall:0.8 mm, ID:7.0x7.0 mm^2)	8.6 mm	0.007 X_0	0.0037 λ^{π}_{abs}
Cu-Clad G-10	1.6 mm	0.013 X_0	0.0033 λ^{π}_{abs}
Epoxy	0.2 mm		0.0003 λ^{π}_{abs}
50-μm G-10	0.05 mm		0.0001 λ^{π}_{abs}
(Only on Chambers with Strips)			
Total	12.1 mm	0.034 X_0	0.0107 λ^{π}_{abs}
Total Thickness (Front Cover Plate + 34 Sampling Layers)			
θ = 0°	51.4 cm	18.2 X_0	0.88 λ^{π}_{abs}
θ = 11° (1/cosθ = 1.02)		18.5 X_0	0.89 λ^{π}_{abs}
θ = 30° (1/cosθ = 1.15)		21.0 X_0	1.01 λ^{π}_{abs}

Table 2-6-2 The Types and the Number of the Signals of the Plug EM Calorimeter

	η	Δη	No. of η-segm.	Δφ	No. of φ-segm.	No. of Long-segm.	No. of Modules	Total No. of Channels
PADS	1.13 ~ 1.2	0.07						
	1.2 ~ 1.32	0.06						
	1.32 ~ 1.41	0.045						
	1.41 ~ 2.40	0.09						
			16	5°	72	3	2	6912
θ - strip	1.2 ~ 1.84	0.02	32	30°	12	1	2	768
φ - strip	1.2 ~ 1.84	6.4	1	1°	30	1	2	720
Anode wire : 156 wires in a Δφ=90° chamber are ganged together.								
Layer No. 1~29 : R=132 cm								
Layer No. 30~34 : R=125 cm								
				90°	4	34	2	272
Monitoring Tubes								48
Total								8720 Channels

Table 2-6-3 Longitudinal Layer Configuration of the Plug EM Calorimeter

@ θ = 11°	@ θ = 30°	Chamber Number		
1.24 X_0	1.41 X_0	1	.....	|
		2		| pad Longitudinal
		...		| Segment I
3.33 X_0	3.78 X_0	5	.....	| (1 - 5)
3.86 X_0	4.37 X_0	6	... θ-strip No.1	|
		7	..... φ-strip No.1	|
		8	... θ-strip No.2	|
		9	..... φ-strip No.2	|
		10	... θ-strip No.3	| pad Longitudinal
		11	..... φ-strip No.3	| Segment II
		12	... θ-strip No.4	| (6 - 29)
		13	..... φ-strip No.4	|
		14	... θ-strip No.5	|
8.57 X_0	9.71 X_0	15	..... φ-strip No.5	|
		16		|
		17		|
		...		|
15.89 X_0	18.01 X_0	29	.....	|
16.41 X_0	18.60 X_0	30	.....	|
		31	.....	| pad Longitudinal
		...		| Segment III
18.50 X_0	20.97 X_0	34	.....	| (30 - 34)

Table 2-6-4 Mechanical Parameters of the Plug EM Calorimeter

Gas Vessel

Outer Diameter	280.7 cm
Inner Diameter	61.0 cm at z=172.7 cm (Front End of Front Cover)
(θ = 10°)	81.5 cm at z=231.1 cm (Rear End of Rear Plate)
Total Weight with Calorimeter Loaded	12.4 metric tons
Total Inner Volume	2.9 m^3
Total Gas Volume	1.2 m^3

Chamber - Absorber Stack

Lead Absorber Panel	Ca : 0.065 %, Sn : 0.7 %
	2.69 mm Thick

Chamber Layer : Sandwich of P.C. Board with pad Pattern, Conductive Plastic Proportional Tube Array, and P.C. Board with Strip Pattern or Ground Plane.

Conductive Plastic Tube	Polystyrene with Fine Grain Carbon Powder
	60 ~ 100 kΩ/square
	I.D. = 7 x 7 mm^2, Wall = 0.8 mm Thick
Anode Wire	50 μm Gold Plated Tungsten
	Tension ~ 150 gr
P.C. Boards	1.6 mm Thick, Copper Clad
Gas	Ar - Ethane 50 % - 50 %
	Isopropyl alcohol (-3°C) 0.9 %
H.V.	1.7 kV (Monitoring Tubes : 1.9 kV)

Table 2-6-5 Performance of the Plug EM Calorimeter

Energy Resolution (pad)		28 % / $\sqrt{E}$
Angular Resolution :	Second pad Segment	$\Delta\theta$: 0.04° ~ 0.2°, $\Delta\varphi$: 0.2° ~ 0.3°
	θ-Strips	$\Delta\theta$: 0.04°
	φ-Strips	$\Delta\varphi$: 0.1°
Linearity at 200 GeV electron		-16 % (1.8 kV)
		-7 % (1.7 kV, -4 % leakage inclusive)
Gain Uniformity (Anode Wire)		rms $\leq$ 2.5 %
Gain Monitoring		rms $\leq$ 0.5 %
Pion Rejection (Electron efficiency 60~80 %)		500 ~ 1000 (100 GeV)

Cs for 2nd segment

NO												MEAN	R.M.S	
1	23.0	20.4	20.2	20.1	20.2	17.3	17.9	18.9	20.2	20.0	19.7	19.2		
2	28.0	24.2	24.1	23.8	24.0	22.6	24.1	23.0	23.8	23.2	22.4	22.0	19.0	1.4	7.2(%)
3	31.0	27.8	27.7	27.8	27.9	26.1	26.3	27.1	26.3	25.5	26.1	26.0	23.8	1.5	6.2(%)
4	73.0	68.9	31.6	31.6	32.3	28.5	31.7	31.3	31.0	31.1	30.1	29.5	27.3	1.5	5.5(%)
5	45.0	38.9	39.6	38.5	37.6	32.6	38.4	35.9	38.3	35.8	35.6	34.6	36.9	14.3	38.8(%)
6	50.0	46.4	47.8	46.8	45.3	46.8	43.4	41.2	41.7	43.0	42.9	40.2	37.4	3.1	8.3(%)
7	58.0	54.8	54.5	54.0	51.8	49.3	52.3	51.6	49.4	52.3	51.2	50.0	44.1	3.1	7.0(%)
8	72.0	67.9	67.7	66.0	63.1	55.6	61.3	61.4	64.0	62.0	58.2	59.1	52.4	2.5	4.8(%)
9	83.0	79.4	81.9	80.0	74.0	69.2	70.8	68.0	70.0	75.7	73.5	74.1	63.2	4.8	7.3(%)
10	97.0	93.1	96.5	95.0	96.4	81.9	86.9	84.9	91.7	92.1	87.2	90.8	75.7	4.7	6.3(%)
11	114.0	111.1	112.5	113.7	116.4	102.8	107.2	100.5	109.3	113.4	111.7	113.0	91.1	4.9	5.4(%)
12	63.0	63.8	64.9	66.8	69.2	60.2	65.9	65.8	64.2	66.4	68.1	68.0	110.9	3.9	3.5(%)
13	68.0	68.3	71.4	73.5	76.2	68.1	73.8	72.7	72.0	77.2	77.3	73.6	85.5	2.5	3.8(%)
14	98.0	97.0	100.0	114.7	123.0	111.3	122.0	118.7	114.7	120.4	124.6	119.2	72.7	3.3	4.6(%)
15	77.0	93.3	96.1	98.2	105.6	92.8	110.2	110.1	100.4	102.6	102.5	103.9	114.4	9.2	8.0(%)
16	34.0	47.8	51.8	39.6	59.1	49.5	60.3	57.8	48.9	51.5	55.3	63.3	99.4	9.1	9.1(%)
													51.4	8.6	16.7(%)

Table 3-1-2-1

Table 3-1-2-2

Cs for 1st segment

NO				MEAN	R.M.S	
1	3.8	3.3	3.7	3.6	0.2	6.7(%)
2	4.5	3.7	3.8	4.0	0.5	11.4(%)
3	5.7	3.8	4.4	4.6	1.0	20.5(%)
4	5.9	4.9	5.4	5.4	0.5	9.2(%)
5	6.6	5.8	5.3	5.9	0.6	10.9(%)
6	8.4	6.2	7.2	7.3	1.1	15.6(%)
7	10.5	8.1	8.8	9.1	1.2	13.4(%)
8	11.7	8.4	9.9	10.0	1.7	16.8(%)
9	14.4	10.2	12.7	12.5	2.1	16.9(%)
10	18.3	12.7	15.9	15.6	2.8	18.0(%)
11	14.8	15.8	18.9	16.5	2.2	13.1(%)
12	12.8	9.6	11.8	11.4	1.6	14.2(%)
13	15.4	10.7	13.0	13.0	2.3	17.9(%)
14	19.4	16.2	13.9	16.5	2.8	16.8(%)
15	15.6	12.8	15.5	14.6	1.6	10.9(%)
16	38.1	31.8	35.1	35.0	3.2	9.0(%)

Table 3-1-2-3

Cs for 3rd segment

NO				MEAN	R.M.S	
1	4.0	4.8	5.9	4.9	1.0	19.6(%)
2	6.2	7.0	6.8	6.7	0.4	6.3(%)
3	7.0	9.2	8.2	8.2	1.1	13.3(%)
4	8.6	9.7	9.2	9.2	0.6	6.0(%)
5	11.1	11.2	9.9	10.8	0.7	6.5(%)
6	11.6	12.8	9.0	11.1	1.9	17.4(%)
7	14.1	14.8	14.1	14.3	0.4	2.7(%)
8	16.3	17.0	15.6	16.3	0.7	4.0(%)
9	14.3	18.4	19.5	17.4	2.7	15.8(%)
10	17.3	18.5	19.1	18.3	0.9	5.0(%)
11	21.1	25.0	23.7	23.3	2.0	8.5(%)
12	18.8	16.1	15.5	16.8	1.8	10.6(%)
13	17.9	18.1	19.6	18.5	0.9	5.0(%)
14	0.1	0.1	0.1	0.1	0.0	0.0(%)
15	0.1	0.1	0.1	0.1	0.0	0.0(%)
16	0.1	0.1	0.1	0.1	0.0	0.0(%)

Table 3-2-1 **Coefficients of 4-th order polynomials for R_1 mean and its sigma, R_2 mean and its sigma as a function of energy.**

$Y(E) = C(0) + C(1)\cdot E + C(2)\cdot E^2 + C(3)\cdot E^3 + C(4)\cdot E^4$
(If E > 200 GeV, Y(E) = Y(200 GeV))

	C(0)	C(1)	C(2)	C(3)	C(4)
R_1 (mean)	0.164E+00	-.323E-02	0.346E-04	-.171E-06	0.314E-09
R_1 (σ)	0.664E-01	-.151E-02	0.181E-04	-.983E-07	0.195E-09
R_2 (mean)	0.815E+00	0.307E-02	-.360E-04	0.184E-06	-.343E-09
R_2 (σ)	0.659E-01	-.153E-02	0.177E-04	-.915E-07	0.173E-09

Table 3-2-2 **Coefficients of 4-th order polynomials for the matrix elements of M as a function of energy.**

$Y(E) = C(0) + C(1)\cdot E + C(2)\cdot E^2 + C(3)\cdot E^3 + C(4)\cdot E^4$
(If E > 200 GeV, Y(E) = Y(200 GeV))

	C(0)	C(1)	C(2)	C(3)	C(4)
M_{11}	0.339E-02	-.949E-04	0.111E-05	-.569E-08	0.106E-10
M_{12}	-.303E-02	0.912E-04	-.108E-05	0.560E-08	-.105E-10
M_{21}	-.303E-02	0.912E-04	-.108E-05	0.560E-08	-.105E-10
M_{22}	0.366E-02	-.113E-03	0.140E-05	-.746E-08	0.143E-10

Table 5-3-1 Cuts for Electron Identification

	Loose	Tight
Central		
- No. of tracks	= 1	= 1
- Had/EM	< 0.1	< 0.05
- E/p	< 1.8	< 1.8
- I (R < 0.7)	< 0.3	< 0.1
- Et of electron (GeV)	> 15	> 15
Endplug		
- No. of tracks	≤ 2	= 1
- Had/EM	< 0.05	< 0.05
- I (R < 0.7)	< 0.3	< 0.1
- Et of electron (GeV)	> 15	> 15

Table 5-4-1 Cuts for W Identification (W cuts)

Central	
- No. of tracks	= 1
- Had/EM	< 0.05
- E/p	< 1.8
- I (R < 0.7)	< 0.1
- Et of electron	> 15 GeV
- χ = Etmiss • Etmiss / ΣEt	> 5 GeV

Table 5-5-1

<<< Event List >>> Cuts on data: "Tight Electron Identification Criteria"

	RUN#	EVT#	# TRK	# WR	# STP	ETA	PHI	ET HAD	ET EM	HAD/EM	ISO(L) R<0.7	ISO(S) R<.25	C HR G	MET RES	TRK-ST	E/P	ET SUM	MET MAG	MET PHI
		(22 events)																	
W	7171	2000	1	3	3	0.08	2.91	0.7	45.3	0.15E-01	0.004	0.004	-1	18.4	41.8	1.20	78.4	38.0	6.14
W	7261	269	1	3	1	0.97	5.71	0.5	33.1	0.14E-01	0.054	0.003	1	26.9	0.7	1.05	49.6	37.8	2.55
W	7311	4687	1	2	1	-0.79	2.86	0.1	32.1	0.45E-02	0.076	0.016	-1	19.6	1.0	1.08	106.7	45.8	5.64
W	7311	5613	1	2	1	0.75	1.69	0.2	29.7	0.61E-02	0.023	0.003	1	18.6	0.5	0.98	65.3	34.9	5.22
W	7353	2610	1	2	1	-0.08	2.61	0.8	38.3	0.21E-01	0.032	0.016	-1	27.5	1.1	1.39	78.0	46.3	5.77
W	7438	38	1	3	1	0.43	1.31	0.8	36.0	0.21E-01	0.029	0.009	1	20.8	0.9	1.25	95.0	44.5	3.86
•	7438	38	2	3	2	0.66	0.1113	4.0	10.7	0.13E+01	0.064	0.018	1	20.8	21.8	2.63	95.0	44.5	3.86
W	7545	1874	1	2	2	-0.77	3.25	0.1	37.6	0.23E-02	0.029	0.002	-1	11.2	1.1	1.19	115.6	35.9	6.05
W	7545	2450	1	1	1	0.35	0.39	0.0	34.9	0.00E+00	0.012	0.000	1	24.3	1.0	1.52	66.7	40.3	3.51
W	7572	2332	1	2	1	-0.04	2.84	0.3	31.5	0.94E-02	0.049	0.020	-1	30.3	1.0	1.19	62.8	43.6	5.97
W	7582	1255	1	2	1	0.00	3.32	0.3	25.0	0.12E-01	0.011	0.000	1	23.2	0.4	0.99	55.7	35.9	0.21
W	7584	496	1	3	1	-0.53	2.19	0.3	45.0	0.64E-02	0.010	0.005	-1	17.9	0.8	0.98	97.0	41.7	5.42
W	7612	388	1	2	3	0.31	0.34	0.4	51.8	0.75E-02	0.000	0.000	-1	34.1	1.2	1.15	78.1	51.6	3.55
W	7613	2392	1	2	1	0.52	0.21	0.4	35.4	0.12E-01	0.003	0.000	1	22.5	4.7	1.46	60.5	36.9	3.47
W	7614	2359	1	3	2	-0.50	2.57	0.1	36.5	0.33E-02	0.025	0.003	1	24.5	0.8	1.07	71.0	41.7	5.66
W	7614	5305	1	2	1	-0.74	5.87	0.5	36.1	0.13E-01	0.045	0.000	1	19.7	0.7	0.85	69.4	36.9	2.77
W	7625	2730	1	2	1	-0.05	4.91	0.5	55.5	0.91E-02	0.013	0.006	-1	12.2	2.5	1.10	101.7	35.3	1.91
W	7681	5510	1	2	1	0.39	0.85	0.3	27.7	0.10E-01	0.020	0.008	-1	11.4	1.8	1.19	61.7	26.5	4.17
W	7687	1832	1	3	2	0.82	4.31	0.5	46.6	0.11E-01	0.005	0.000	1	18.9	0.4	1.10	104.8	44.5	1.33
W	7787	2937	1	3	2	-0.21	2.72	0.8	39.0	0.19E-01	0.043	0.000	1	19.2	0.8	1.09	120.2	48.1	5.76
W	7805	2045	1	3	1	-0.78	0.32	0.6	38.6	0.17E-01	0.023	0.012	1	15.4	1.2	0.85	76.8	34.3	3.50
Q	7170	72	1	2	0	-0.42	6.15	0.0	17.3	0.00E+00	0.091	0.017	-1	6.3	0.0	1.38	93.2	24.2	2.78
•	7170	72	1	2	2	-0.40	0.02	0.0	4.7	0.00E+00	0.333	0.000	1	6.3	16.8	0.22	93.2	24.2	2.78
Z	7700	6524	0	3	0	-1.18	0.39	6.9	9.7	0.72E+00	0.098	0.000	0	7.0			113.8	28.3	0.52
•	7700	6524	1	2	1	-0.13	3.48	0.2	47.0	0.47E-02	0.022	0.008	-1	7.0	0.4	1.05	113.8	28.3	0.52
		(other events)																	
Z	7744	5364	0	8	0	2.69	1.54	0.1	19.6	0.36E-02	0.299	0.021	0	1.1			86.2	9.6	2.84
•	7744	5364	1	2	1	0.19	4.81	0.3	22.0	0.13E-01	0.047	0.012	1	1.1	0.3	0.98	86.2	9.6	2.84
Z	7767	940	0	2	1	-1.20	6.09	0.1	22.6	0.54E-02	0.121	0.014	0	2.4			144.5	18.4	5.41
•	7767	940	1	3	1	0.64	2.95	0.5	32.6	0.17E-01	0.033	0.013	-1	2.4	0.4	0.97	144.5	18.4	5.41
Z	7288	1276	0	12	0	3.43	-3.48	0.0	7.6	0.00E+00	0.610	0.278	0	0.6			54.4	5.7	3.84
•	7288	1276	1	1	1	0.26	1.03	0.4	20.9	0.18E-01	0.029	0.000	-1	0.6	0.6	1.07	54.4	5.7	3.84
Z	7377	830	0	3	1	0.64	3.37	0.2	25.3	0.60E-02	0.327	0.047	0	2.4			108.2	16.1	3.64
•	7377	830	1	2	1	0.03	0.26	0.5	49.1	0.10E-01	0.072	0.068	1	2.4	1.6	0.98	108.2	16.1	3.64
Z	7769	4235	0	2	2	0.77	3.81	0.0	12.8	0.00E+00	0.016	0.010	0	0.1			106.6	3.5	2.87
•	7769	4235	1	2	1	0.51	5.75	0.1	34.6	0.34E-02	0.039	0.013	-1	0.1	1.0	1.08	106.6	3.5	2.87
•	7769	4235	1	11	0	1.79	2.14	0.1	28.2	0.30E-02	0.083	0.017	0	0.1	0.0	0.00	106.6	3.5	2.87
Q	7145	3427	1	1	1	0.62	1.14	0.0	15.6	0.00E+00	0.020	0.020	-1	0.7	0.6	0.96	55.1	6.4	4.20
•	7145	3427	1	2	1	0.50	4.49	1.0	5.9	0.18E+00	1.068	0.243	1	0.7	0.8	0.88	55.1	6.4	4.20
Q	7167	1692	1	2	1	-0.47	2.88	0.6	20.5	0.29E-01	0.087	0.025	-1	0.3	1.0	1.01	61.4	4.2	5.09
Q	7280	6233	1	3	2	0.12	1.72	0.8	21.6	0.37E-01	0.097	0.026	-1	0.6	10.6	1.77	80.4	7.1	4.90
Q	7287	2826	1	2	0	0.58	4.41	0.7	14.4	0.48E-01	0.039	0.039	1	0.0	0.0	1.03	48.5	1.5	4.60
Q	7331	2152	0	3	1	0.12	2.51	0.1	23.6	0.46E-02	0.235	0.050	0	3.6			112.2	20.0	3.98
•	7331	2152	1	2	1	0.38	6.13	0.2	33.4	0.56E-02	0.072	0.000	-1	3.6	3.2	1.10	112.2	20.0	3.98
Q	7353	2399	0	3	1	-0.23	3.51	0.3	6.1	0.43E-01	2.004	0.646	0	1.4			207.5	17.2	1.63
•	7353	2399	0	1	0	0.64	2.47	0.0	3.1	0.00E+00	1.322	0.056	0	1.4			207.5	17.2	1.63
•	7353	2399	1	3	1	1.16	6.18	1.0	49.3	0.20E-01	0.042	0.024	0	1.4	167.8	0.00	207.5	17.2	1.63
•	7353	2399	1	9	1	-0.87	1.91	2.4	17.7	0.13E+00	0.404	0.025	-1	1.4	54.0	8.73	207.5	17.2	1.63
•	7353	2399	1	3	2	-0.24	3.69	0.5	4.0	0.12E+00	2.566	1.406	1	1.4	2.2	0.81	207.5	17.2	1.63
•	7353	2399	3	3	4	0.92	3.84	3.3	7.2	0.47E+00	2.185	1.410	1	1.4	39.5	4.79	207.5	17.2	1.63
Q	7477	3287	1	2	1	0.29	2.78	0.5	15.6	0.32E-01	0.069	0.000	1	3.3	1.4	1.36	79.8	16.2	5.92
Q	7512	1909	1	1	1	0.11	2.58	0.2	18.1	0.14E-01	0.049	0.022	1	2.1	1.0	1.05	84.3	13.3	6.20
Q	7569	937	1	3	1	-0.85	2.50	0.7	15.8	0.43E-01	0.049	0.018	-1	0.3	4.7	1.42	64.8	4.1	2.58
Q	7572	****	0	2	2	-1.03	5.62	0.0	4.1	0.00E+00	1.230	0.025	0	0.6			95.5	7.8	4.17
•	7572	****	1	2	1	-0.97	0.39	0.4	17.4	0.20E-01	0.060	0.010	0	0.6	10.4	0.00	95.5	7.8	4.17
Q	7582	1705	1	2	1	-0.50	0.12	0.7	18.0	0.39E-01	0.084	0.084	-1	1.5	16.7	0.15	74.4	10.7	3.39
Q	7584	1024	0	3	1	1.57	2.83	0.0	11.0	0.00E+00	0.383	0.262	0	0.8			80.1	7.8	2.85
•	7584	1024	1	2	2	1.15	5.38	0.1	15.1	0.49E-02	0.097	0.011	0	0.8	24.2	0.00	80.1	7.8	2.85
Q	7585	3557	1	2	2	-0.52	0.05	0.6	17.0	0.37E-01	0.049	0.033	-1	0.7	31.0	1.10	78.1	7.2	2.54
Q	7614	3608	1	3	1	-0.82	5.89	1.4	26.8	0.49E-01	0.071	0.023	-1	1.2	0.8	0.95	82.5	9.8	3.48
Q	7625	1861	1	2	1	-0.71	0.23	0.1	17.5	0.55E-02	0.081	0.004	1	0.7	3.3	0.93	67.0	6.9	1.52
Q	7680	1422	1	2	1	0.18	6.01	0.0	15.6	0.00E+00	0.067	0.033	-1	1.8	1.2	1.07	90.7	12.8	2.78
•	7680	1422	1	3	1	0.19	2.72	0.1	4.8	0.26E-01	1.992	0.000	1	1.8	37.2	1.89	90.7	12.8	2.78
Q	7681	2096	1	2	1	-0.67	2.54	0.7	29.2	0.24E-01	0.051	0.012	-1	4.1	2.0	0.95	86.5	18.7	6.12
Q	7687	2892	1	2	2	-0.83	4.93	0.1	26.3	0.42E-02	0.051	0.000	1	2.4	2.1	1.08	70.6	13.0	1.80
Q	7687	4437	1	3	0	-0.73	5.35	0.8	40.9	0.19E-01	0.067	0.014	1	1.7	0.0	1.62	97.2	12.8	2.28
•	7687	4437	1	12	0	-1.98	1.90	1.6	12.3	0.13E+00	0.868	0.340	0	1.7	0.0	0.00	97.2	12.8	2.28
Q	7689	2862	0	2	1	-0.24	2.74	0.0	5.0	0.00E+00	0.916	0.549	0	0.1			60.7	2.3	2.49
•	7689	2862	1	3	3	-0.41	0.07	0.5	18.2	0.29E-01	0.100	0.007	-1	0.1	26.8	0.58	60.7	2.3	2.49
•	7689	2862	1	3	3	-0.58	3.78	0.7	7.5	0.90E-01	0.835	0.083	-1	0.1	23.7	1.00	60.7	2.3	2.49
Q	7700	3927	1	2	1	0.76	6.22	0.6	16.5	0.39E-01	0.033	0.009	-1	1.3	11.7	1.59	64.0	9.1	3.09
Q	7700	6384	1	2	1	1.20	2.00	0.0	19.7	0.00E+00	0.063	0.012	0	0.5	32.9	0.00	79.1	6.3	5.90
Q	7744	2049	1	3	0	-0.68	5.47	0.6	14.6	0.40E-01	0.047	0.036	1	0.4	0.0	1.08	71.1	5.0	3.39
Q	7770	157	1	2	0	0.65	0.51	0.1	19.8	0.58E-02	0.090	0.045	-1	1.0	0.0	1.10	57.8	7.7	3.64
Q	7787	2245	1	2	3	0.33	4.10	0.0	17.0	0.00E+00	0.078	0.000	1	2.8	0.3	1.05	60.3	12.9	1.16
Q	7804	1925	1	2	1	0.71	3.06	0.3	15.1	0.22E-01	0.082	0.029	-1	0.2	4.3	1.33	79.2	4.1	5.67

**** = 12436 W: W candidates, Z: Z candidates, Q: QCD events, •: same event as above

Table 5-5-2 W Sample

W --> eν candidates	22.0 ± 4.7	
QCD Backgrounds	0.7 ± 0.5	(calculation)
	(1 event from visual scan)	
W --> τν,		
τ --> eνν	1.4 ± 0.4	(Monte Carlo)
Z --> e + e	1	(visual scan)
Net W--> eν	18.9 ± 4.7	

Fig. 1-1-1

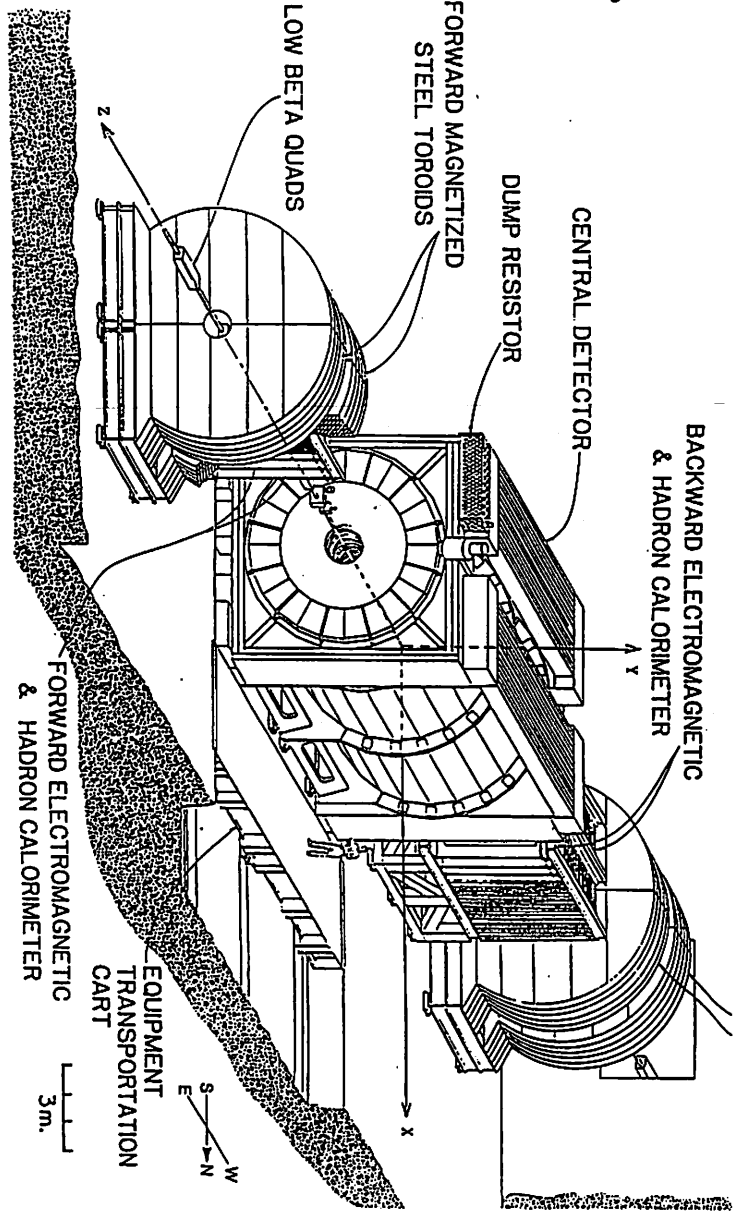

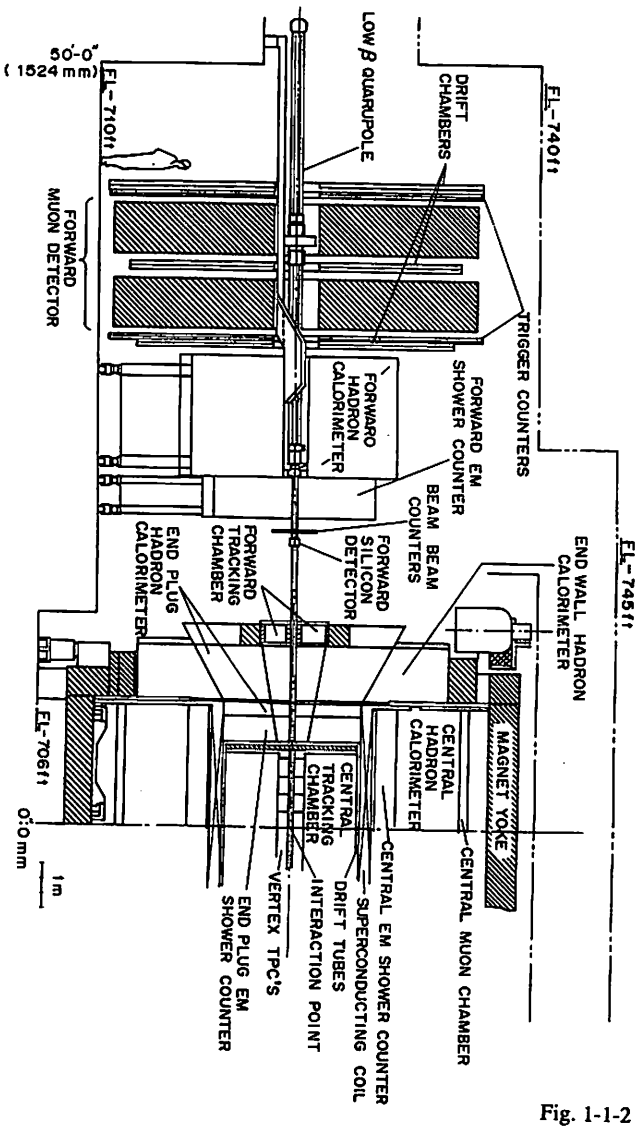

Fig. 1-1-2

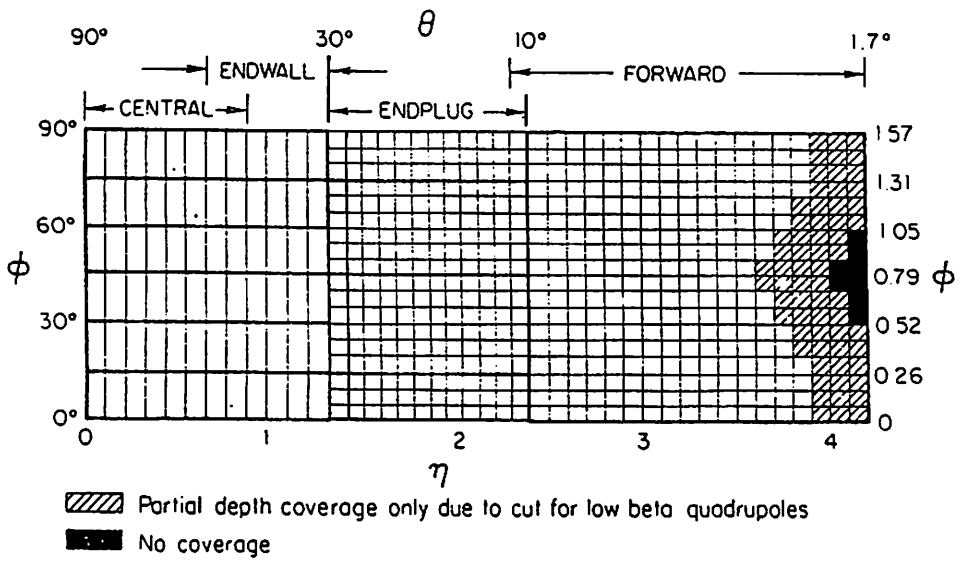

Fig. 1-1-3

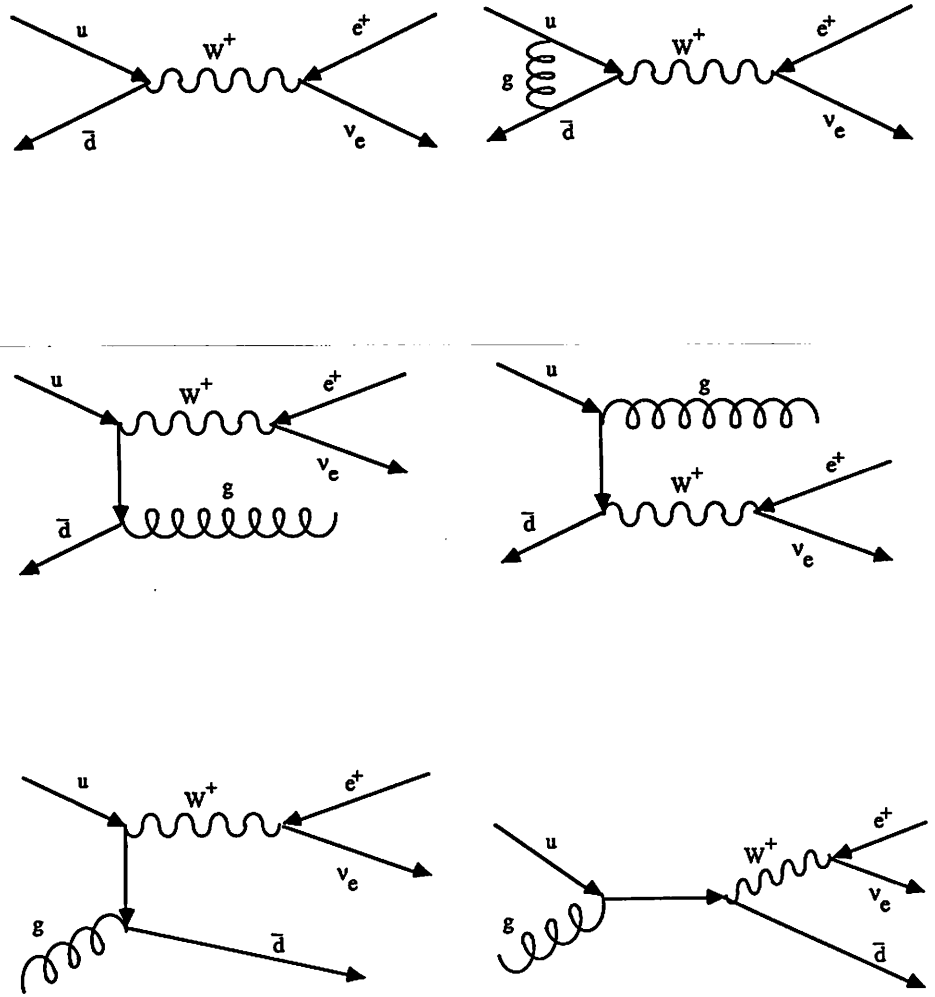

Fig. 1-2-1

Fig. 1-2-2

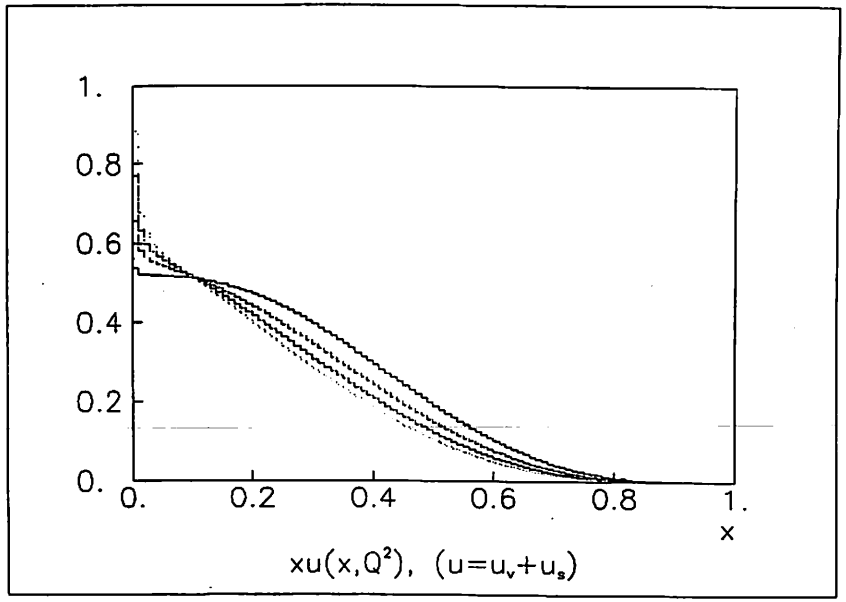

Fig. 1-2-3

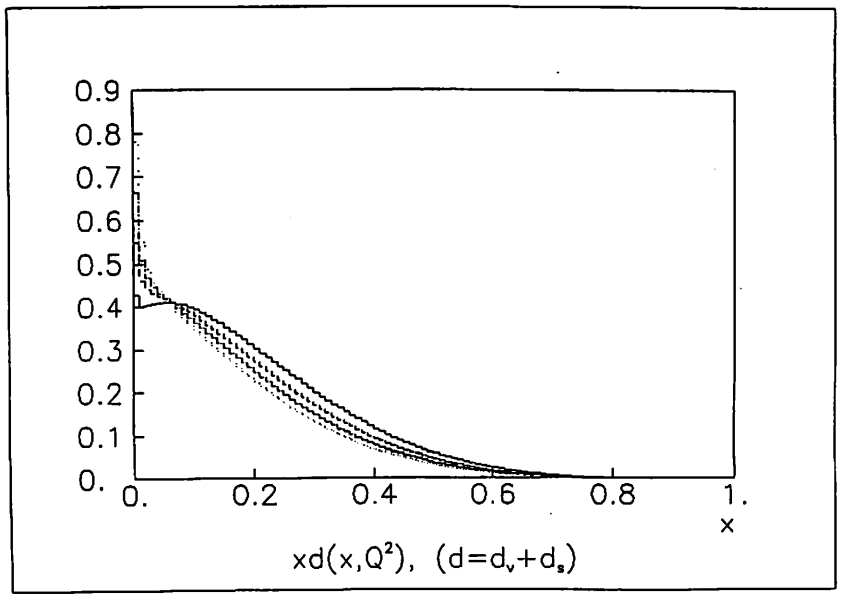

Fig. 1-2-4

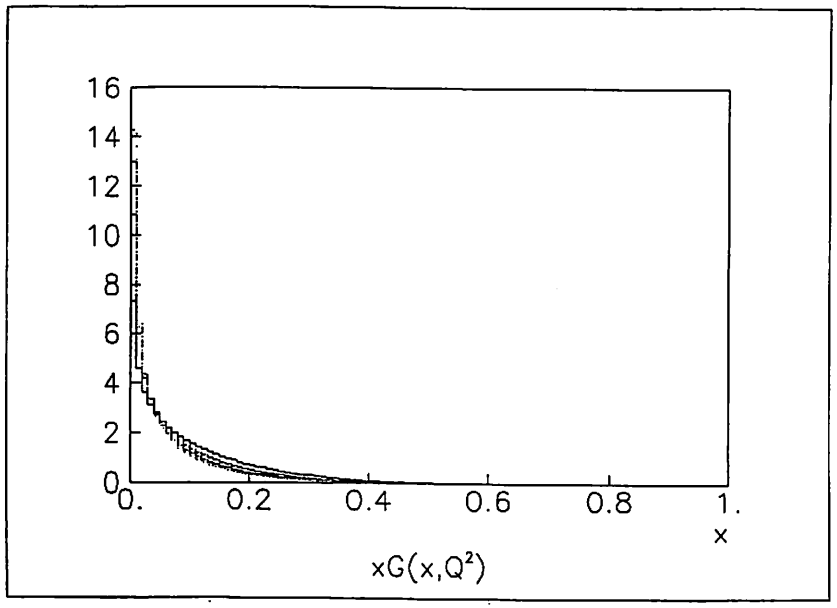

Fig. 1-2-5

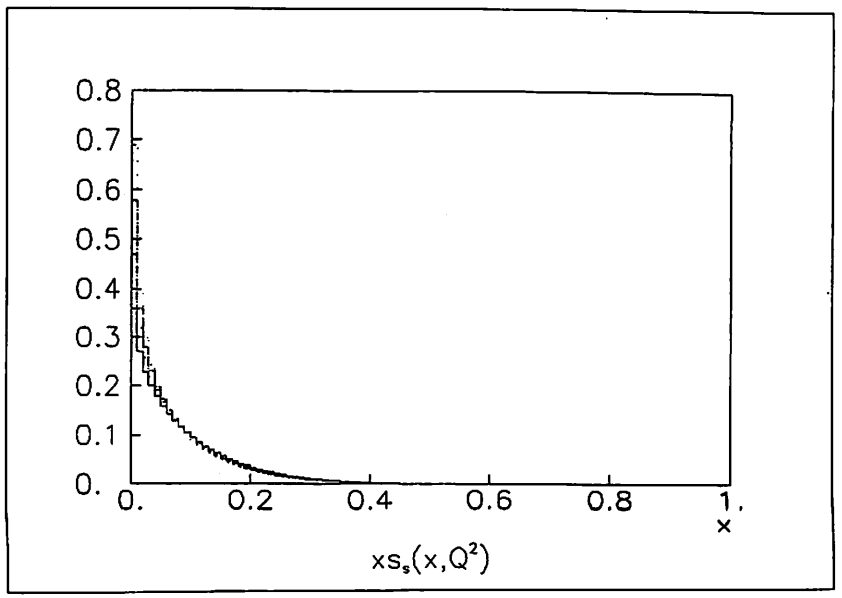

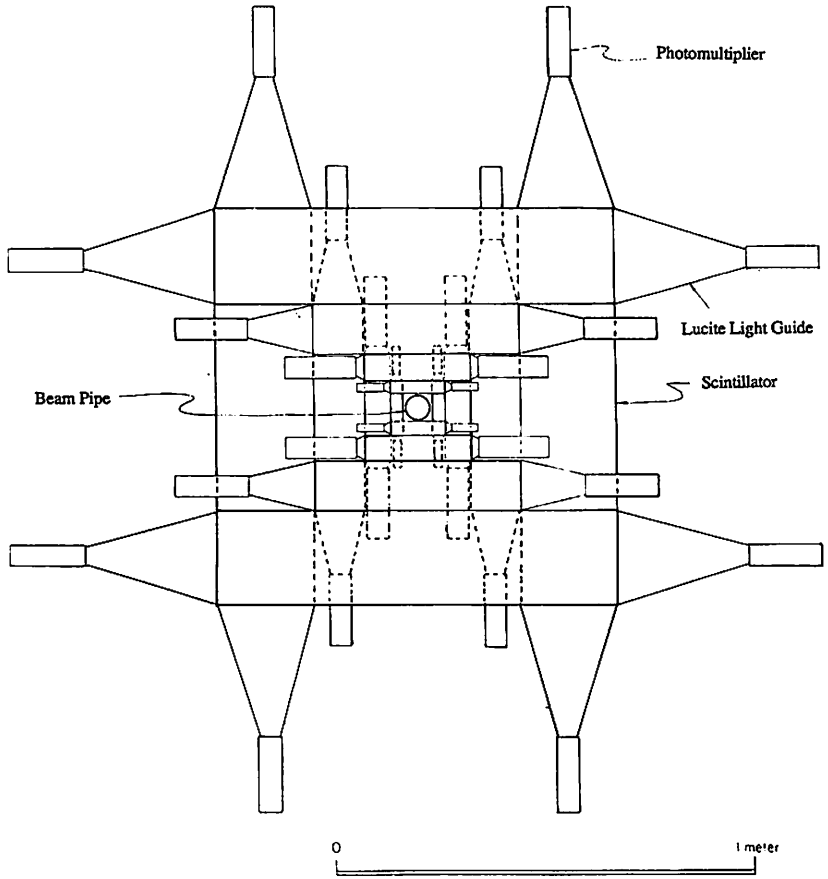

Fig 2-1-1

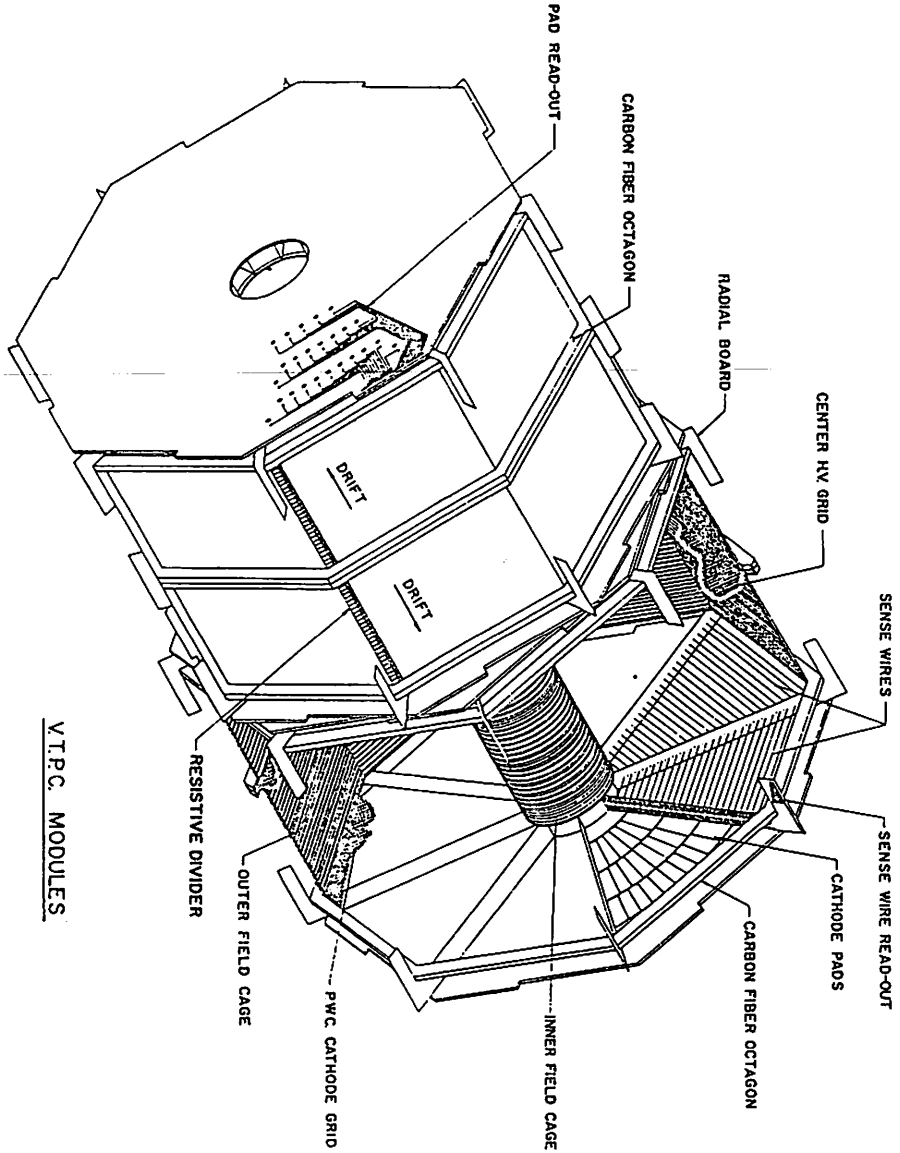

Fig. 2-2-1

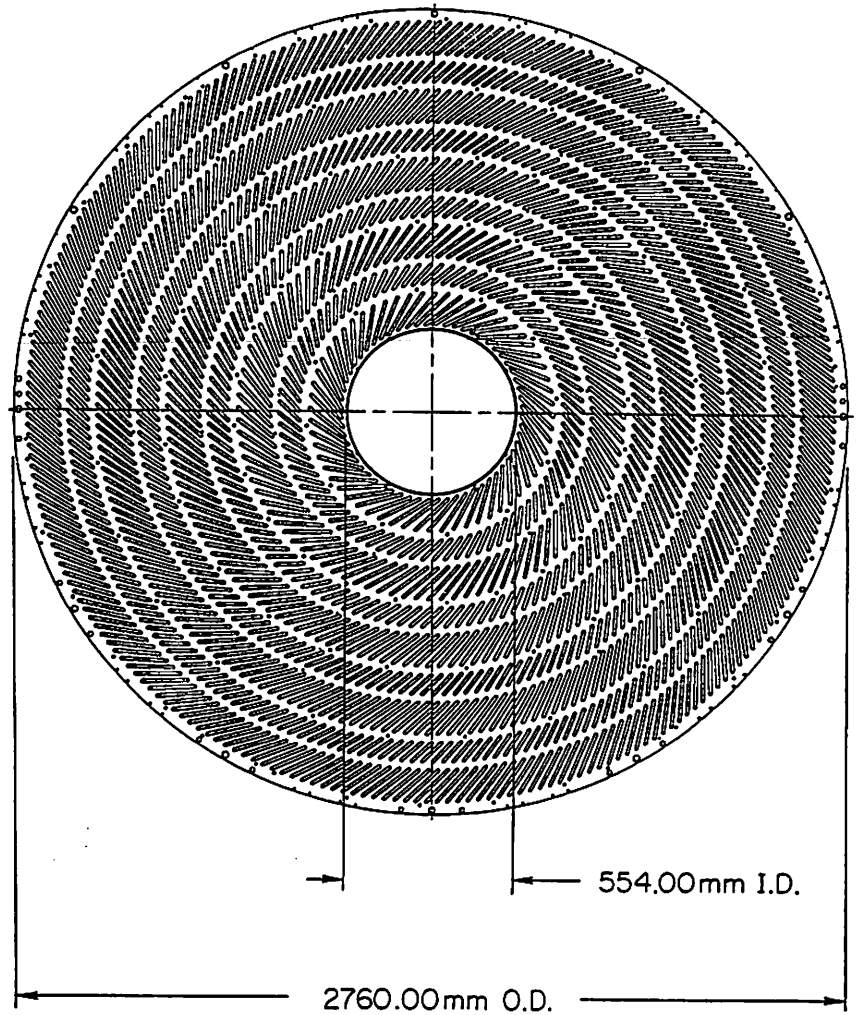

Fig. 2-3-1

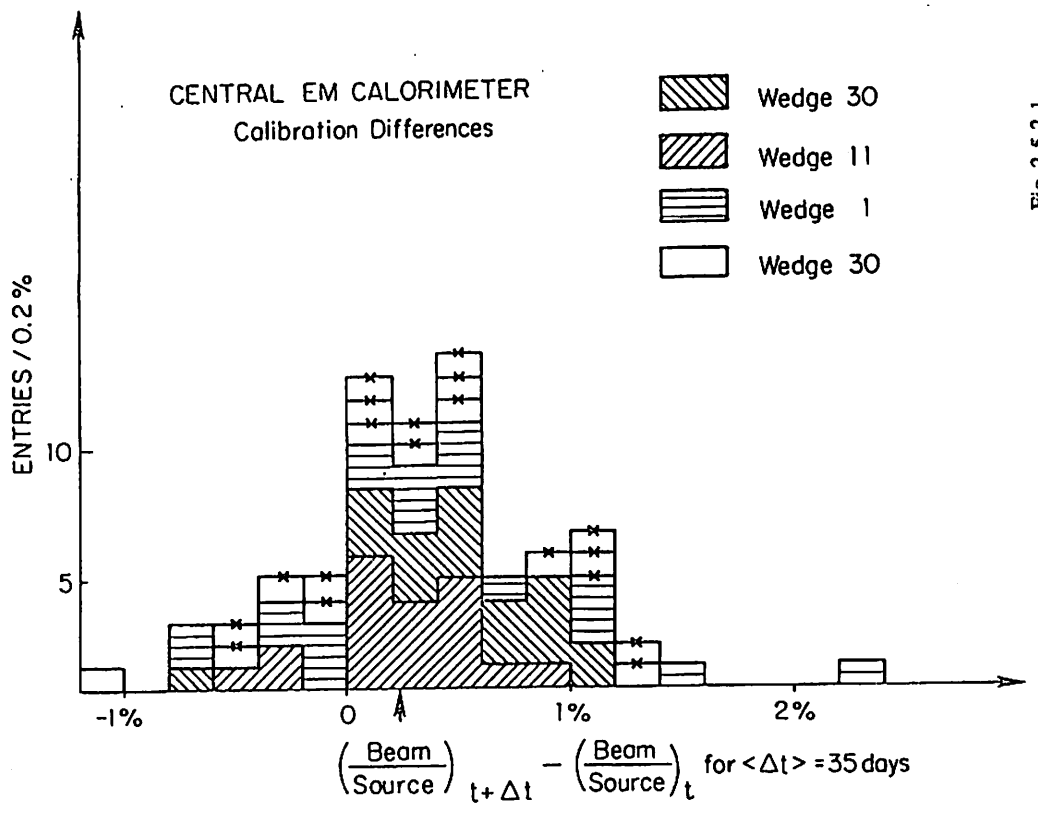

Fig. 2-5-2-1

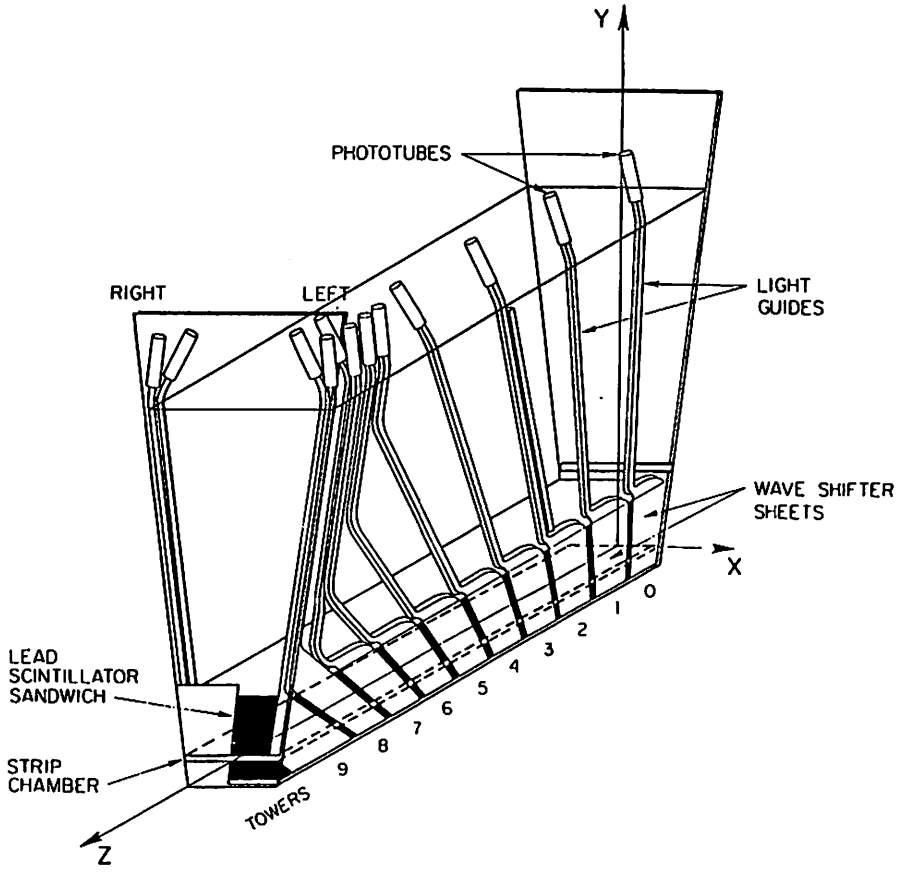

Fig. 2-5-1

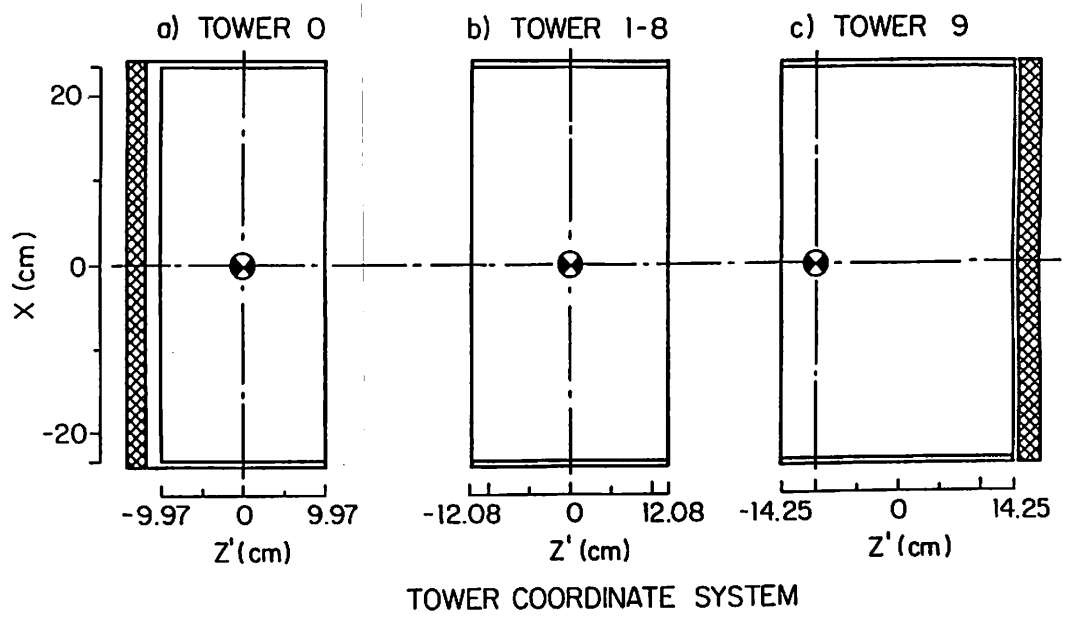

Fig. 2-5-2-2 (b)

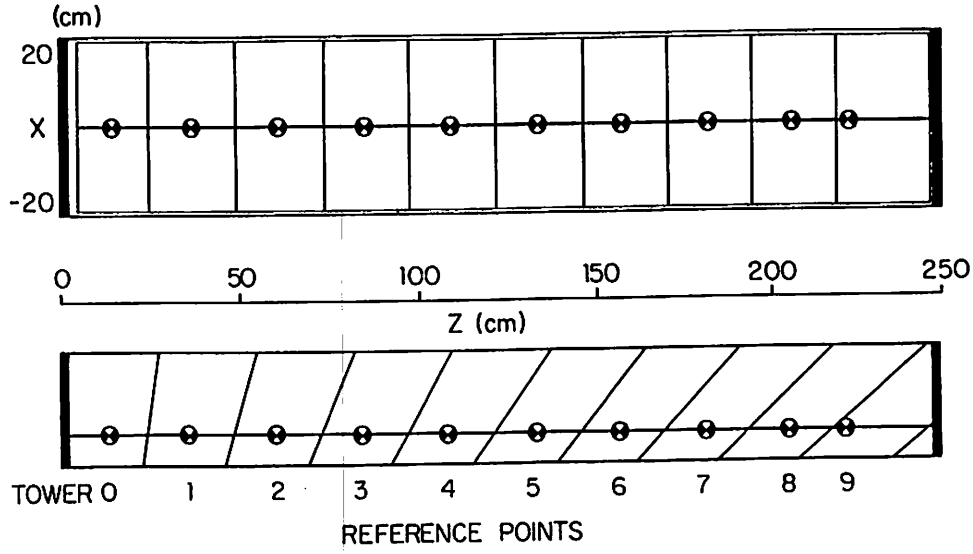

Fig. 2-5-2-2 (a)

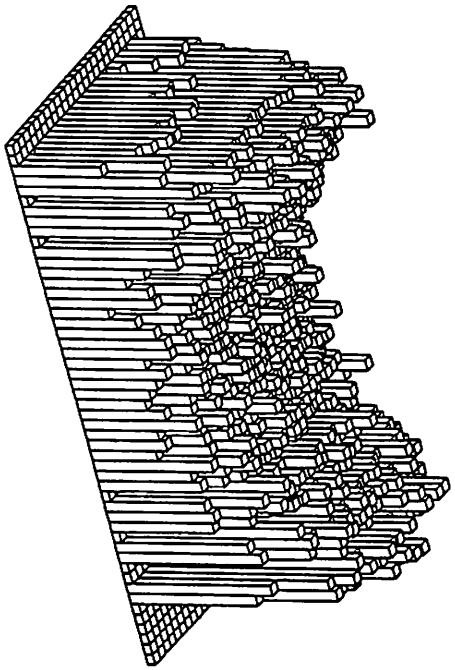

Fig. 2-5-2-3

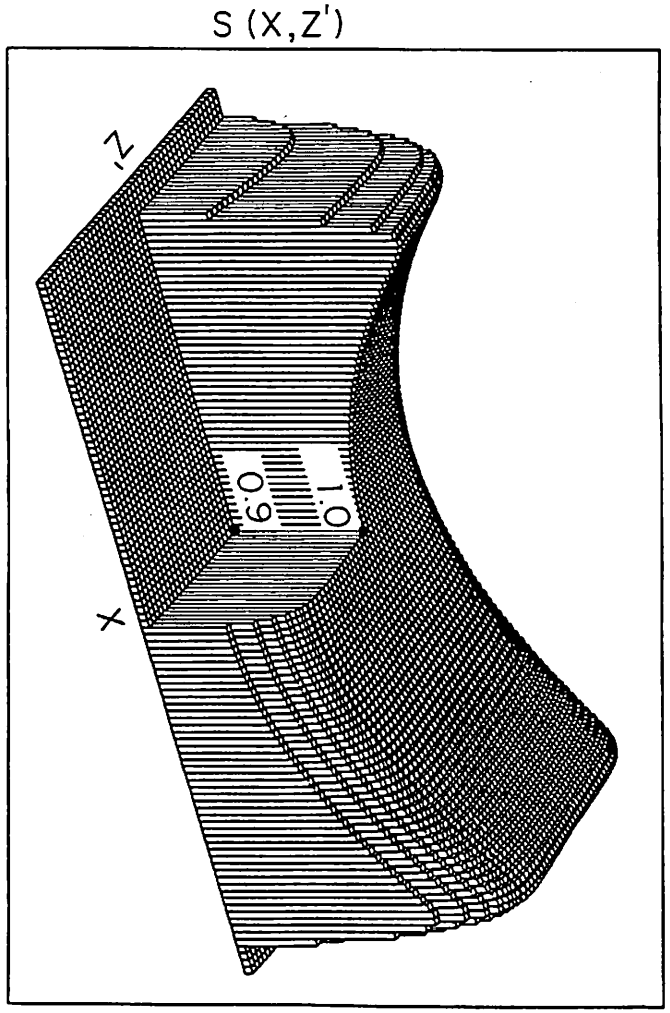

Fig. 2-5-2-4

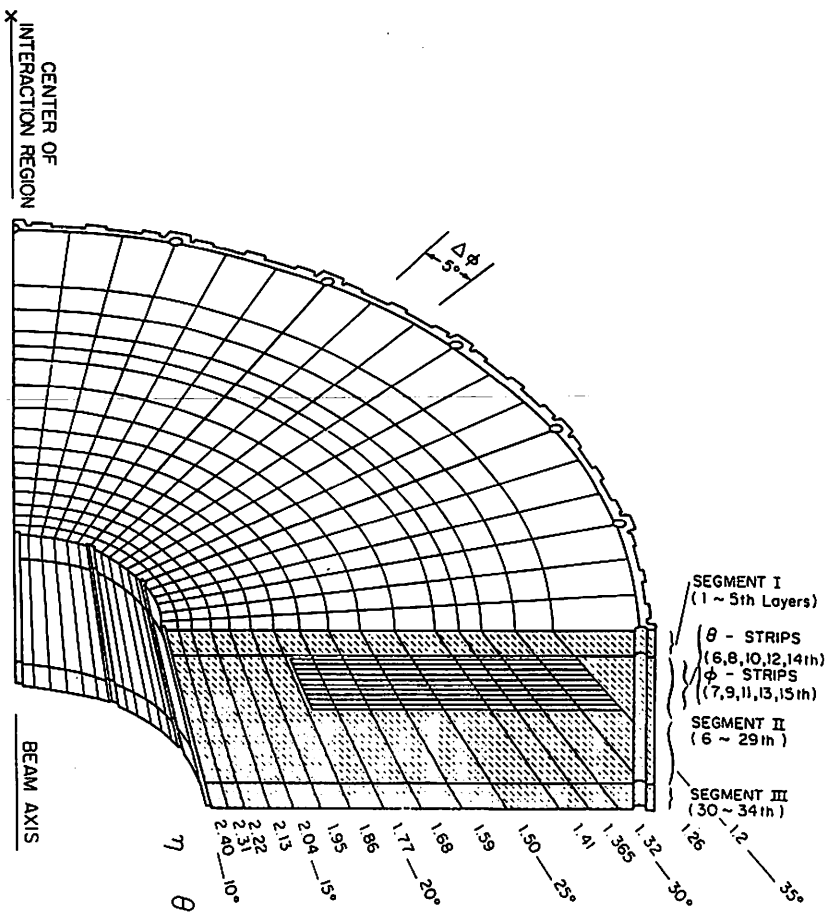

Fig. 2-6-1

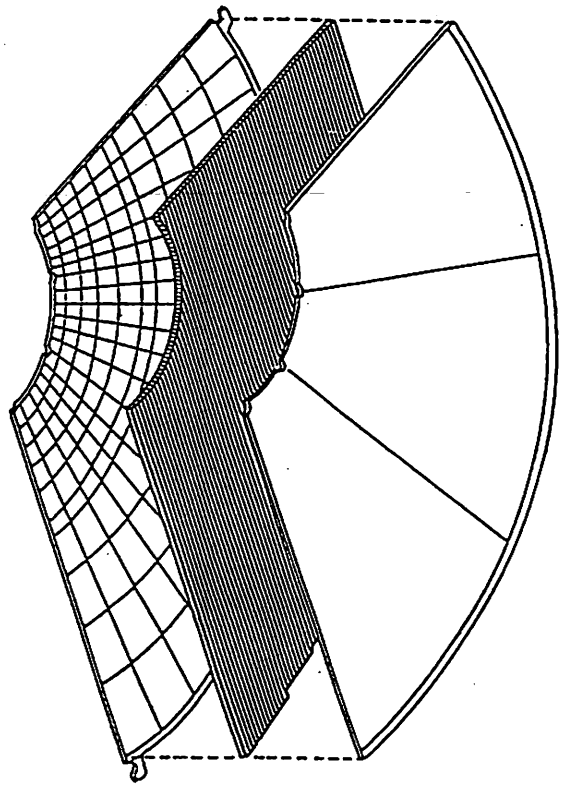

Fig. 2-6-2

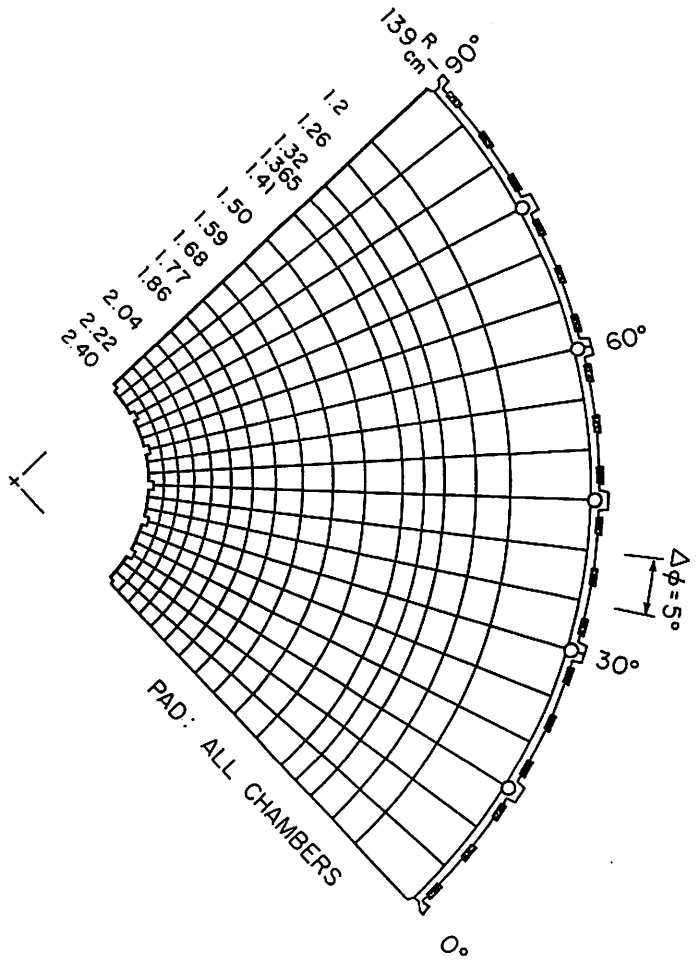

Fig. 2-6-3

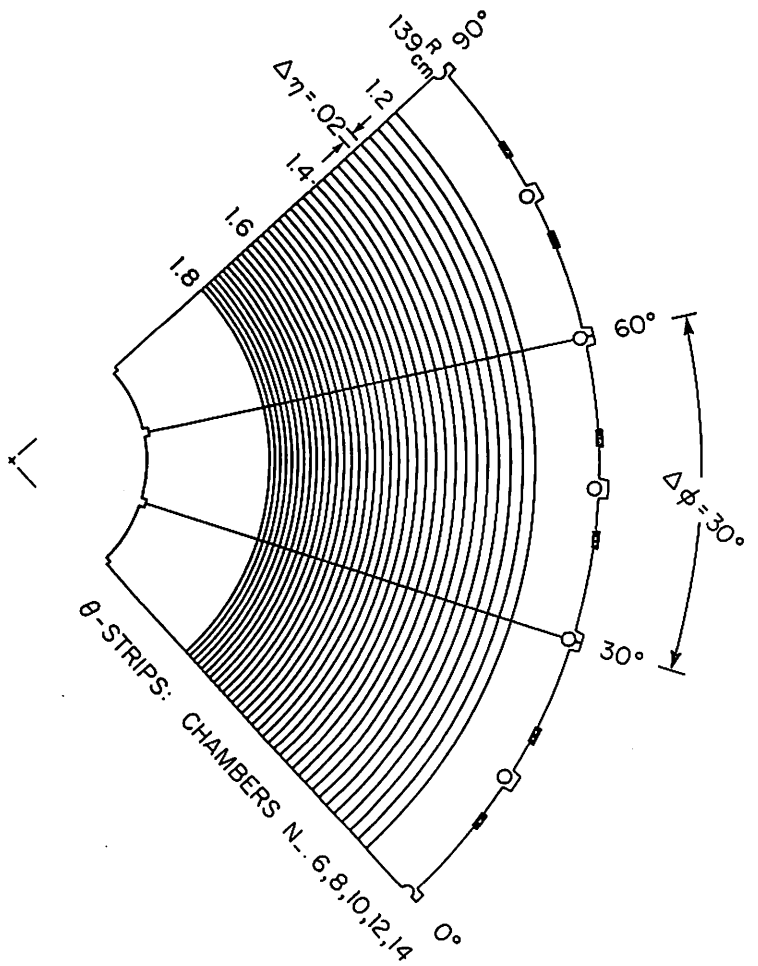

Fig. 2-6-4

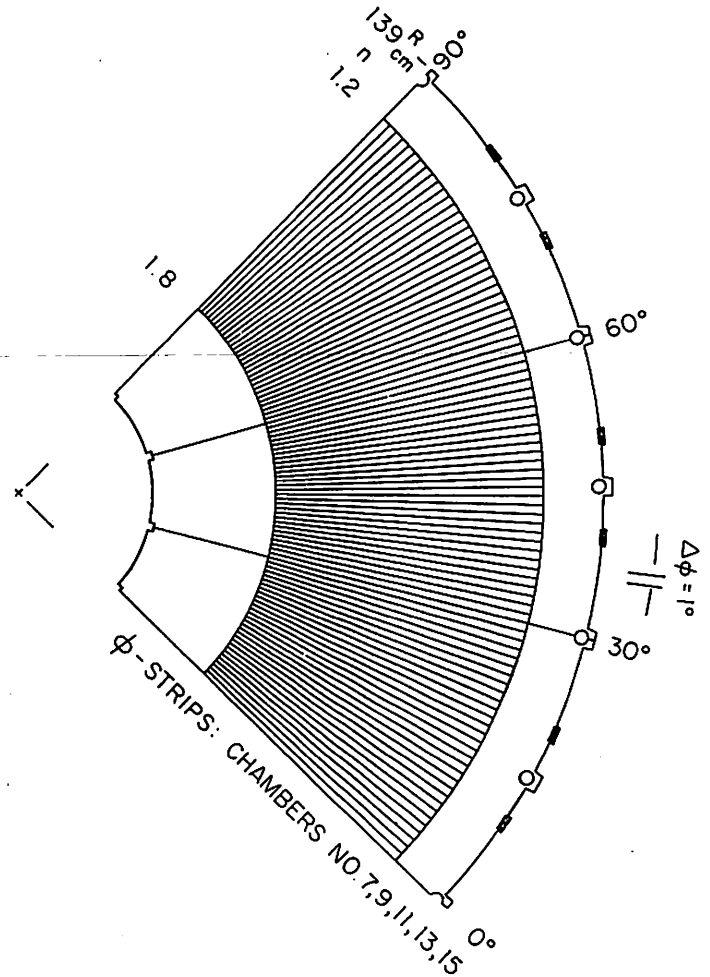

Fig. 2-6-5

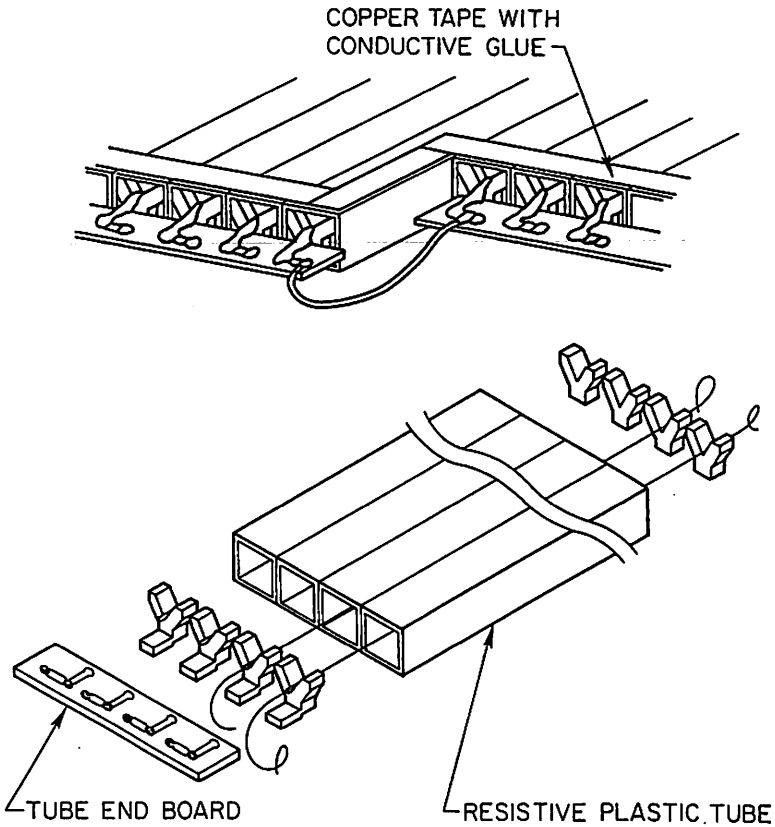

Fig. 2-6-6

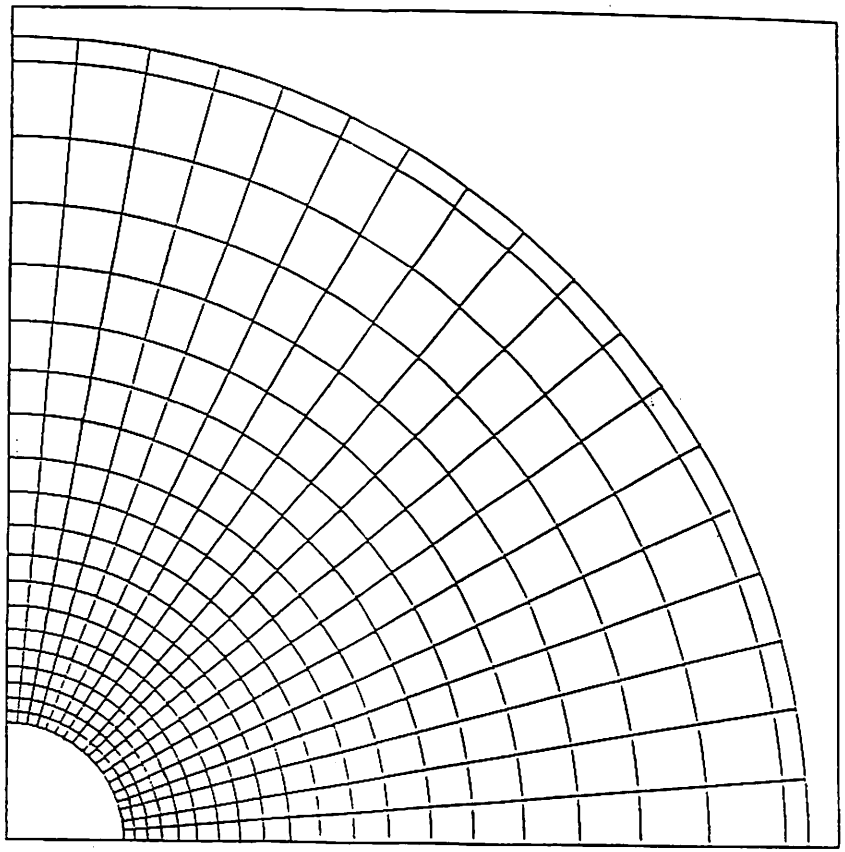

Fig. 2-7-1

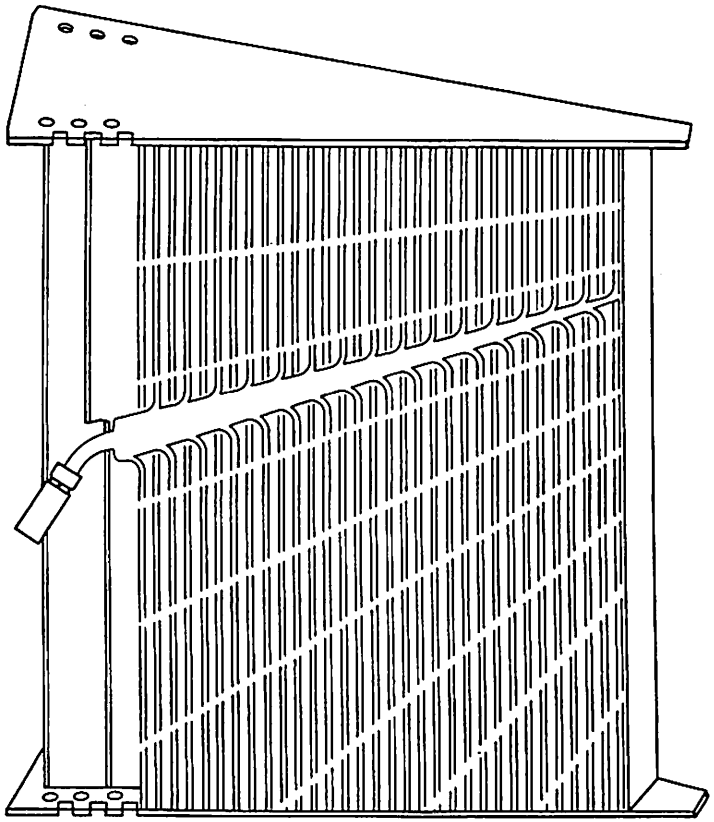

Fig. 2-8-1

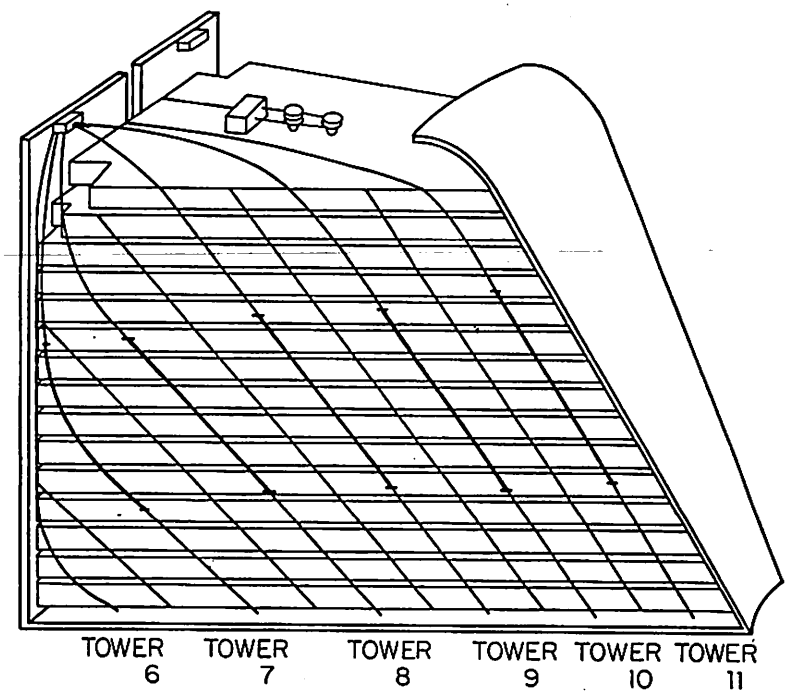

Fig. 2-8-2

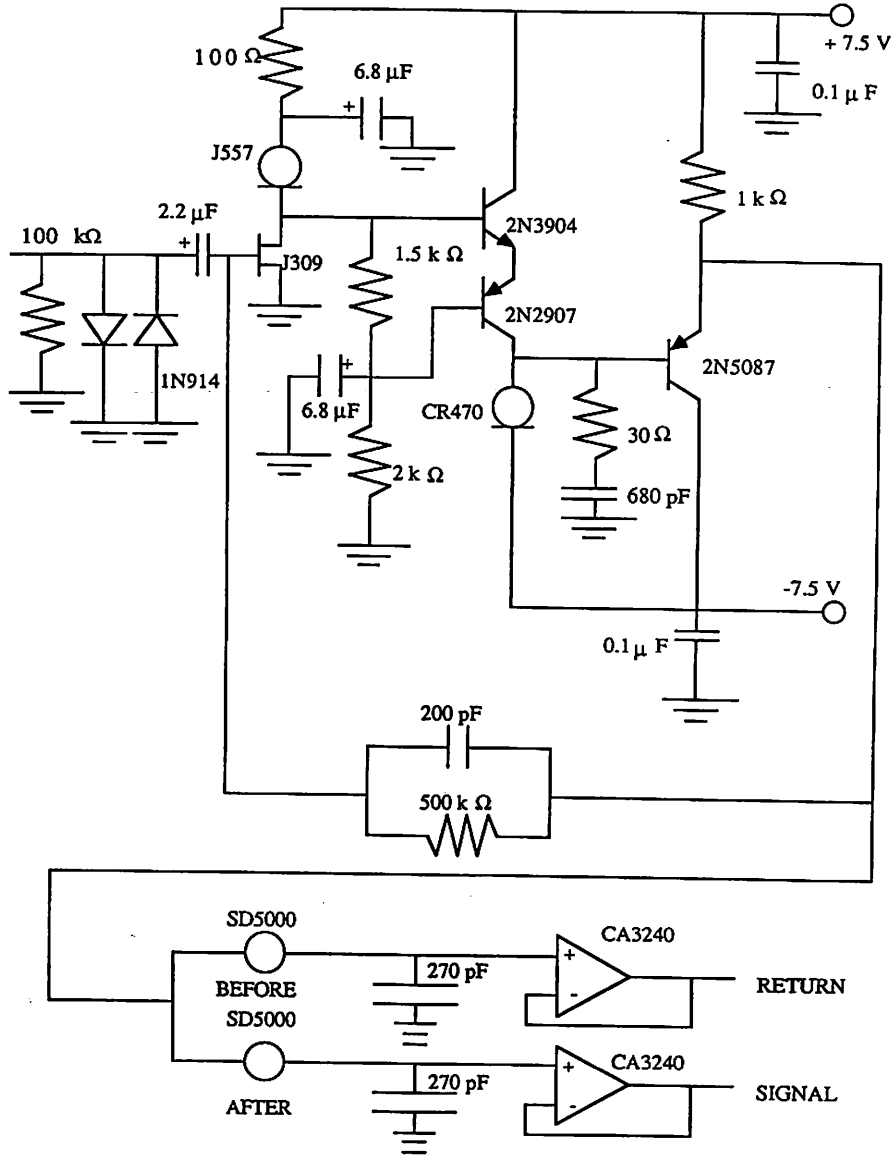

Fig. 3-1-1-1

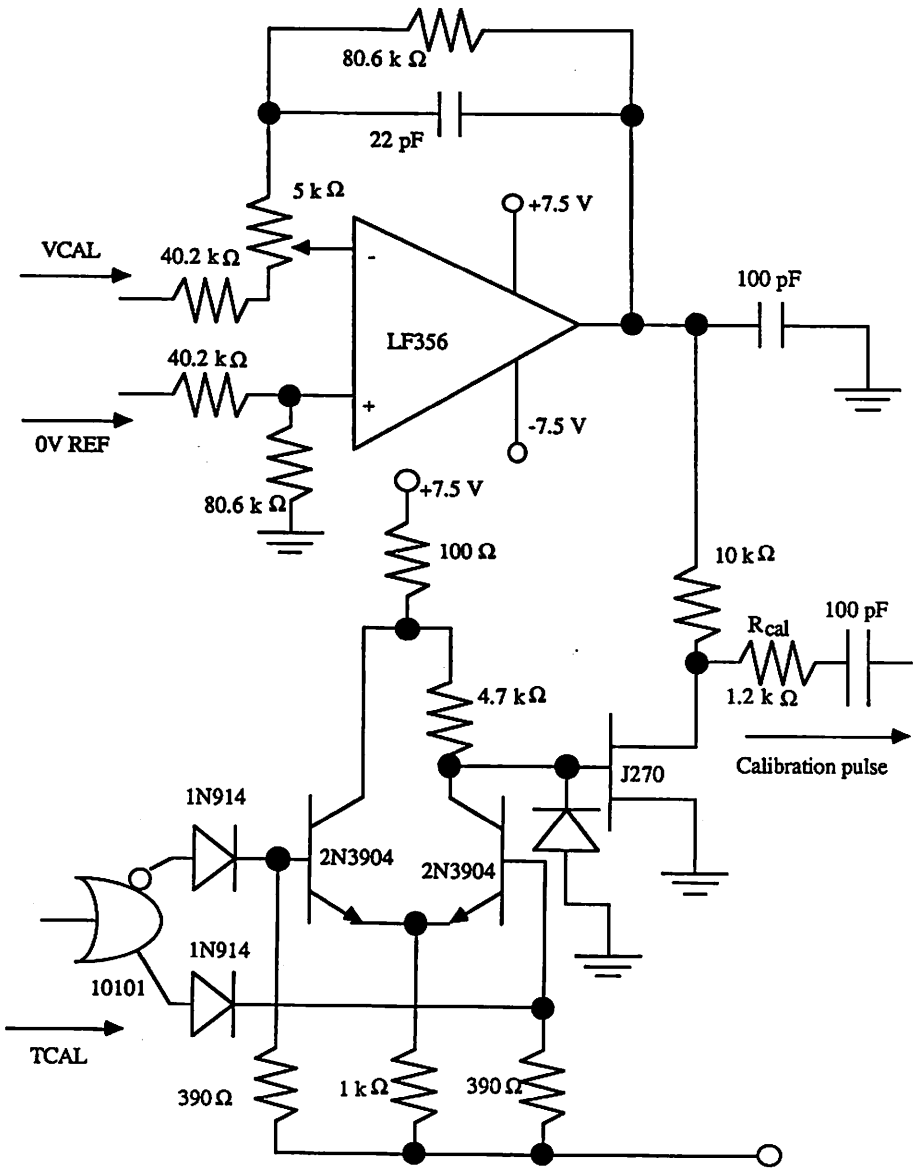

Fig. 3-1-1-2

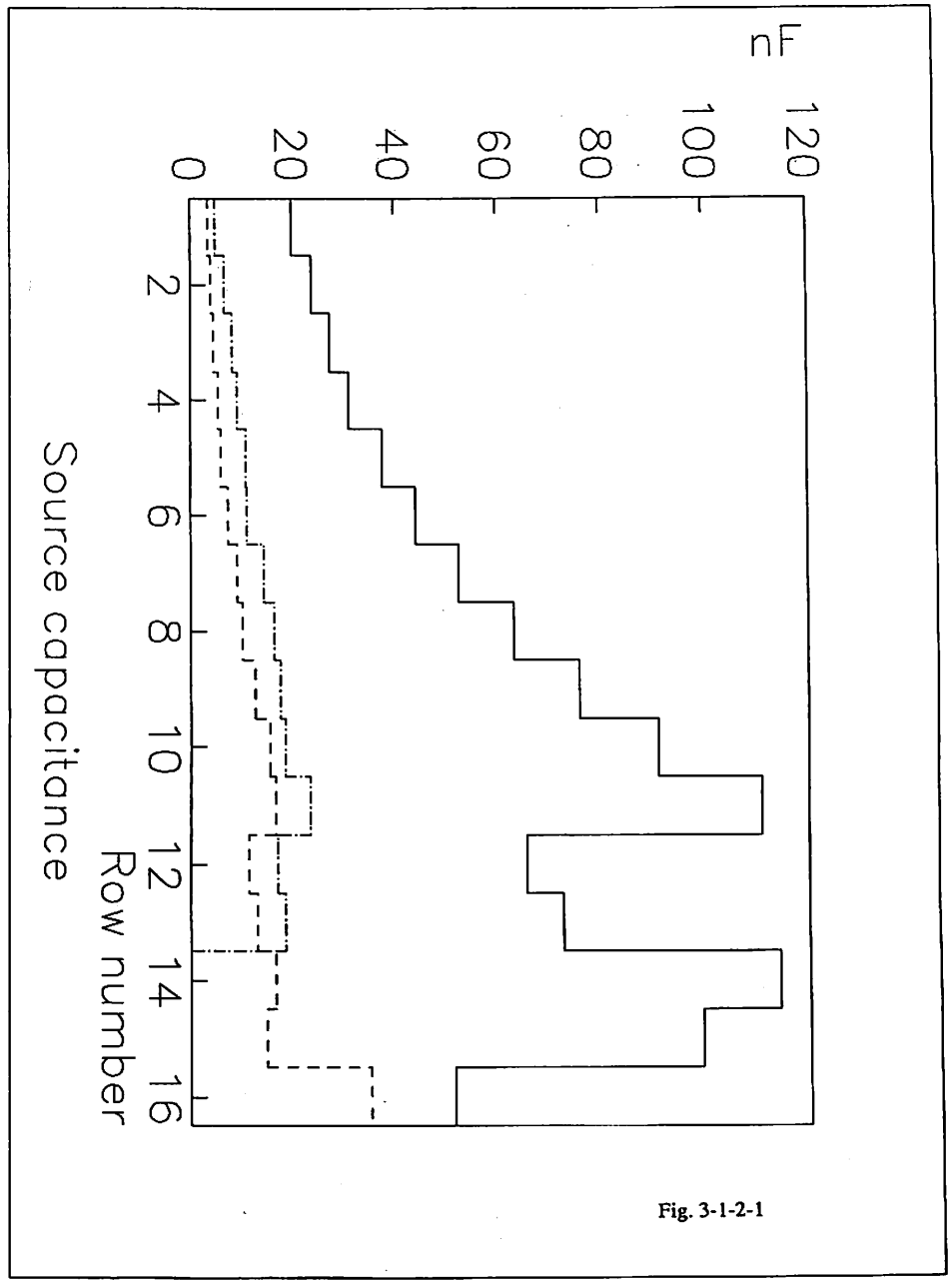

Fig. 3-1-2-1

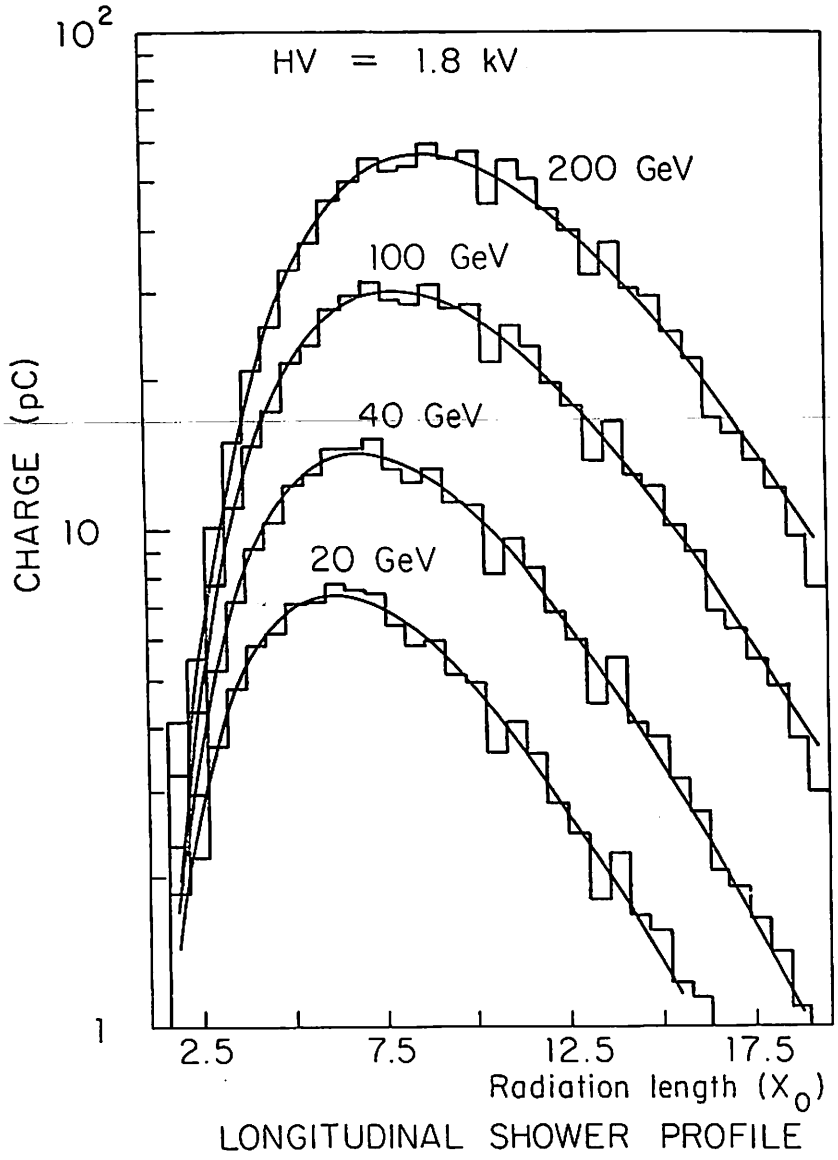

Fig. 3-1-3-1

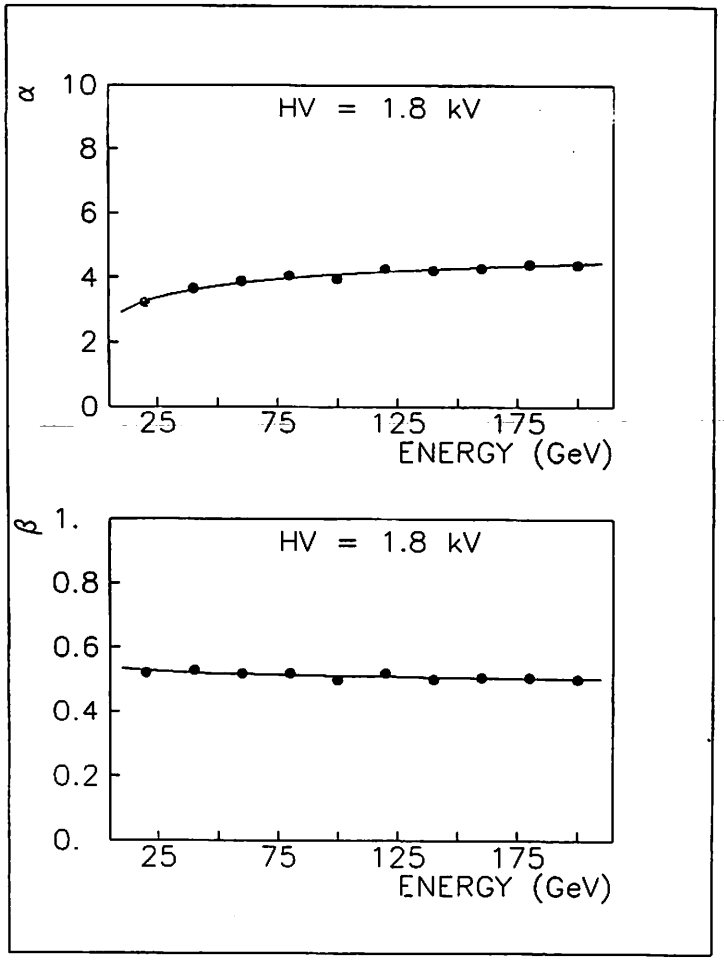

Fig. 3-1-3-2

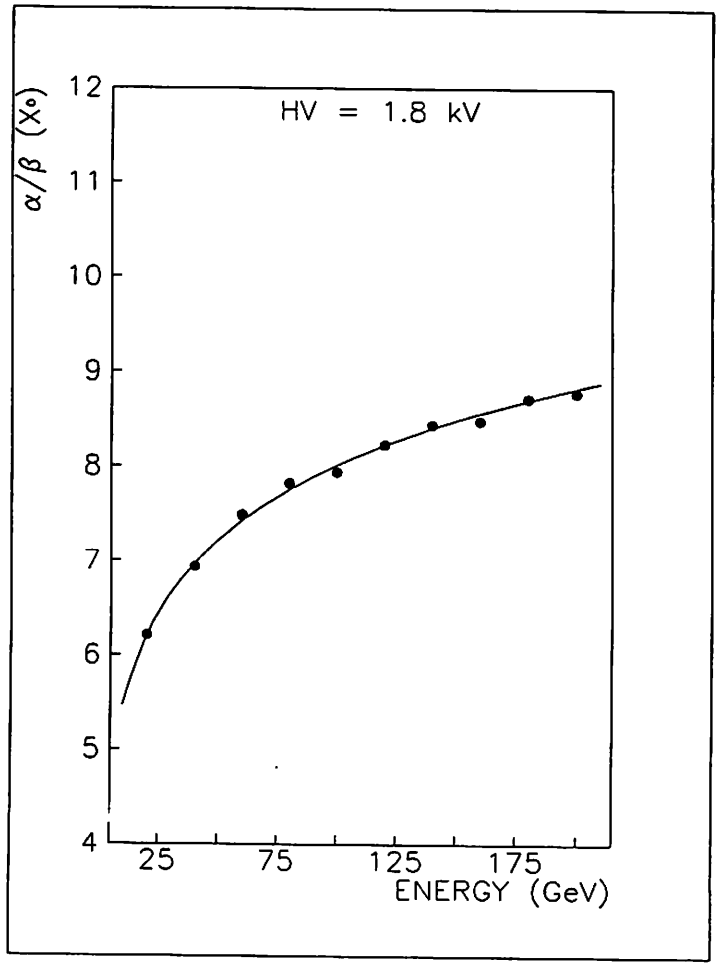

Fig. 3-1-3-3

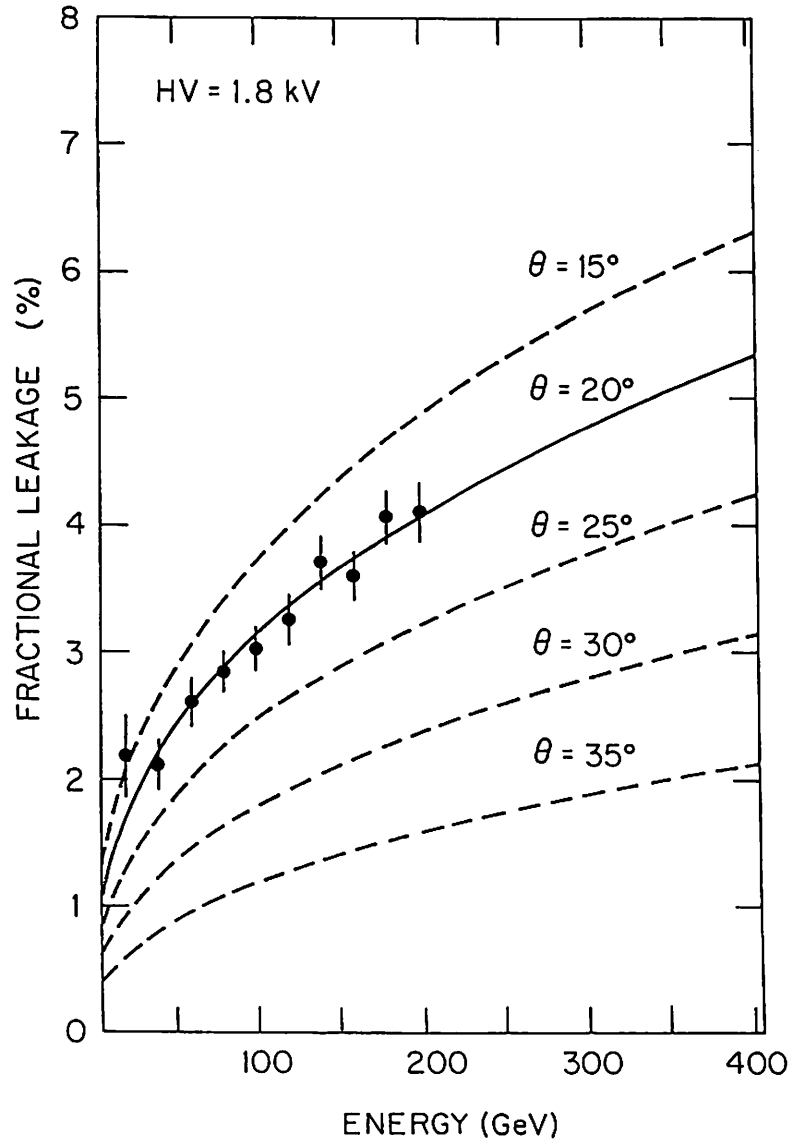

Fig. 3-1-3-4

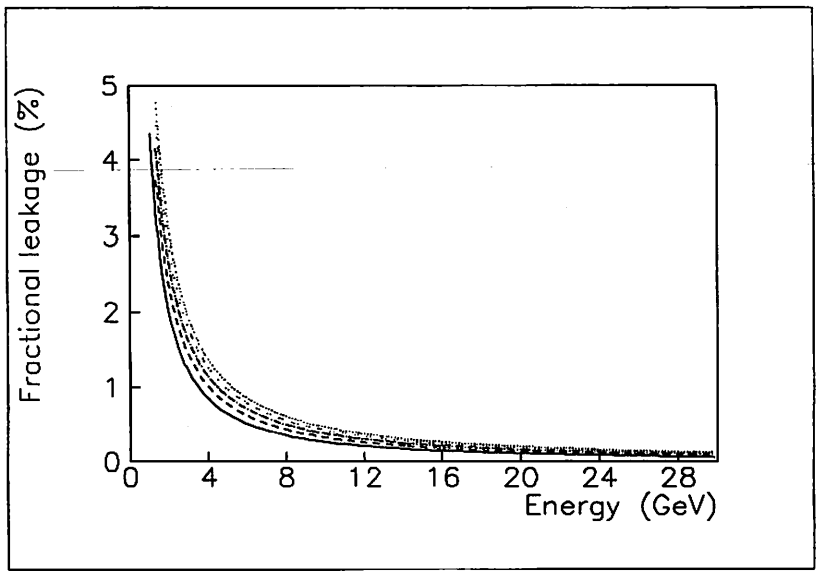

Fig. 3-1-3-5

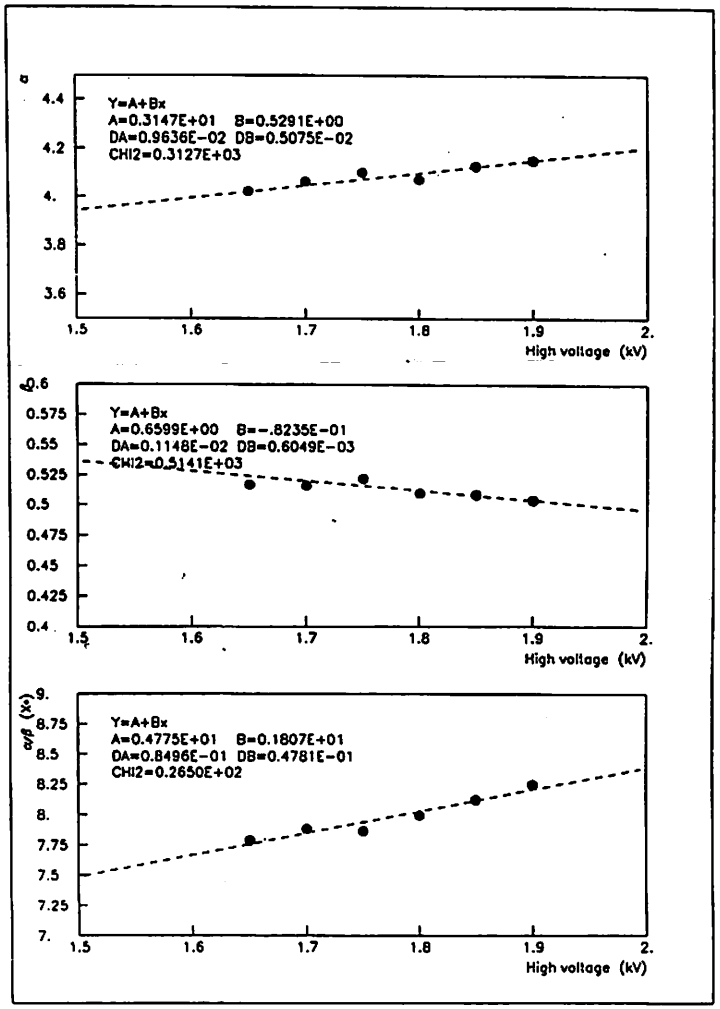

Fig. 3-1-3-6

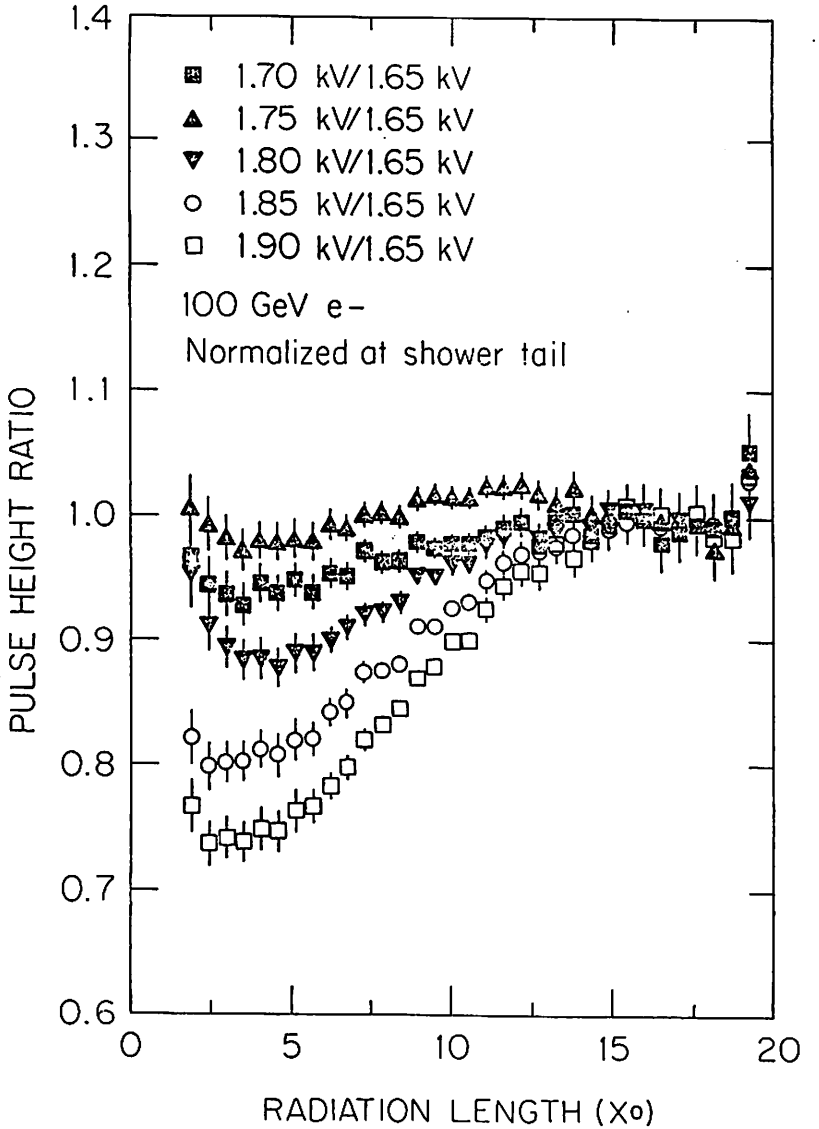

Fig. 3-1-3-7

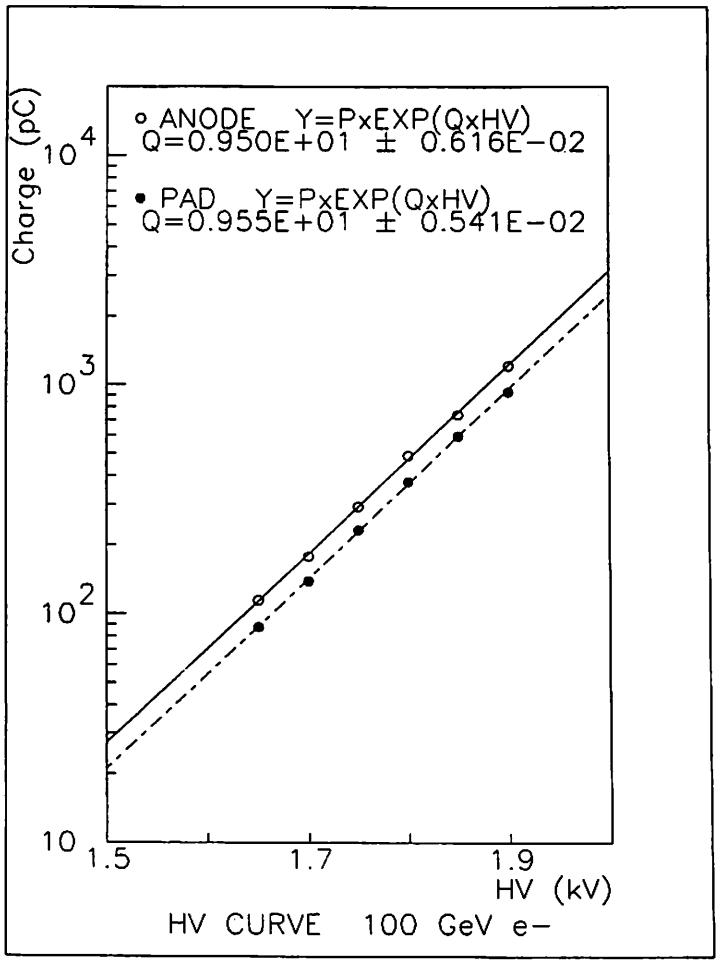

Fig. 3-1-3-8

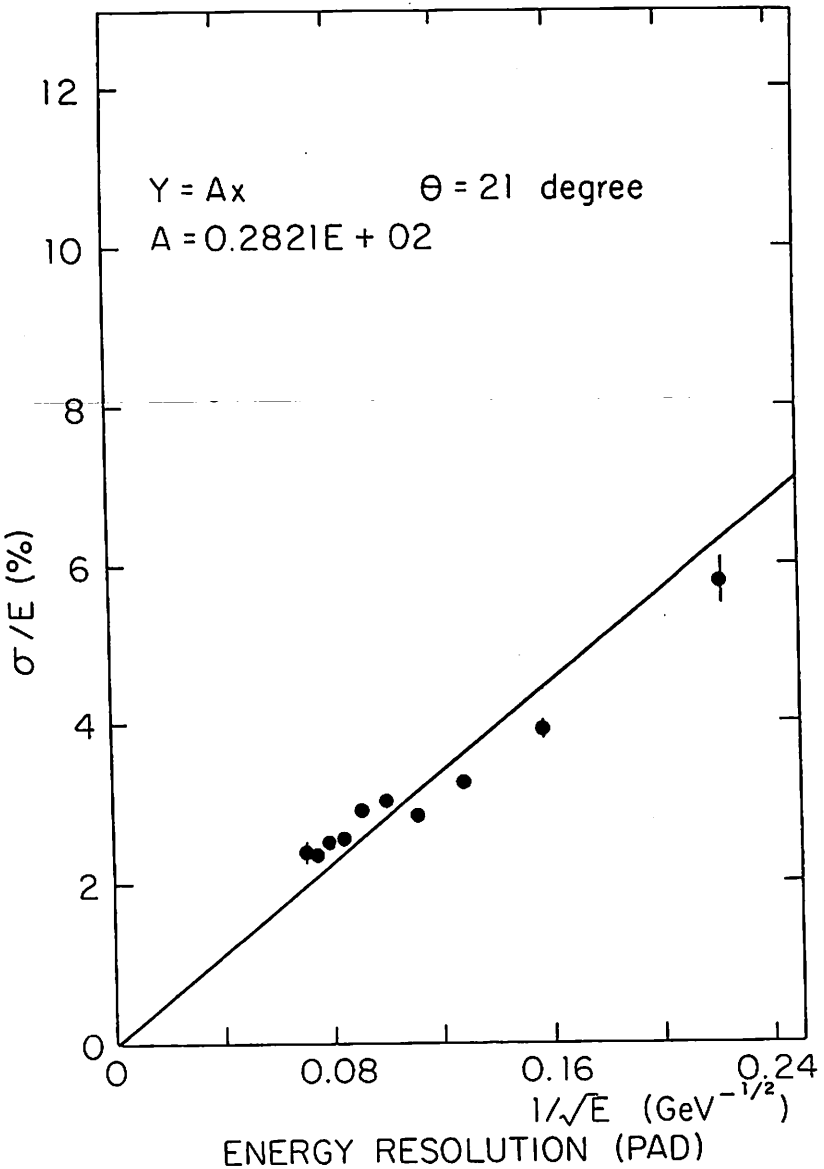

Fig. 3-1-3-9

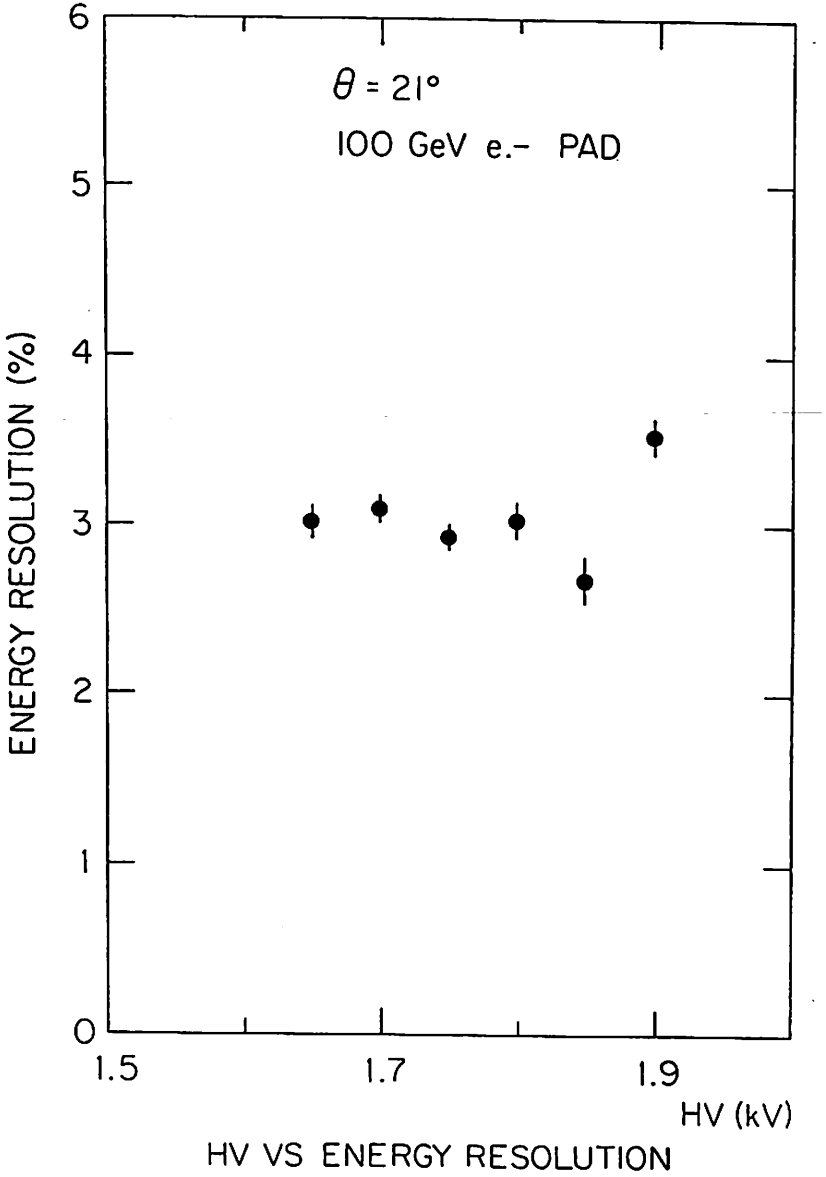

Fig. 3-1-3-10

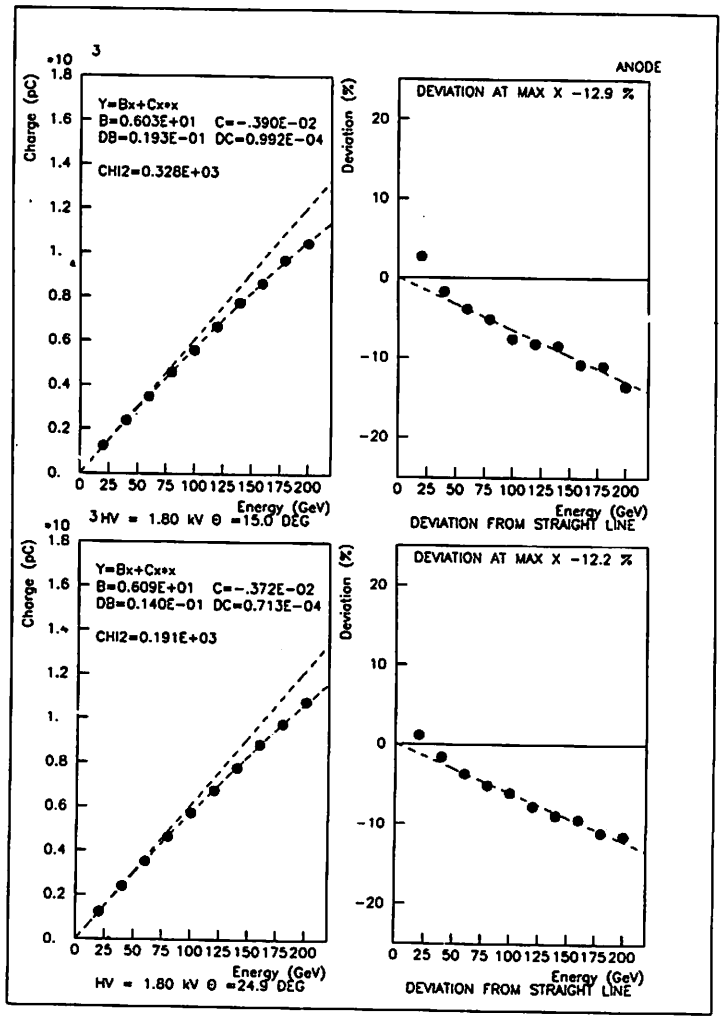

Fig. 3-1-3-11

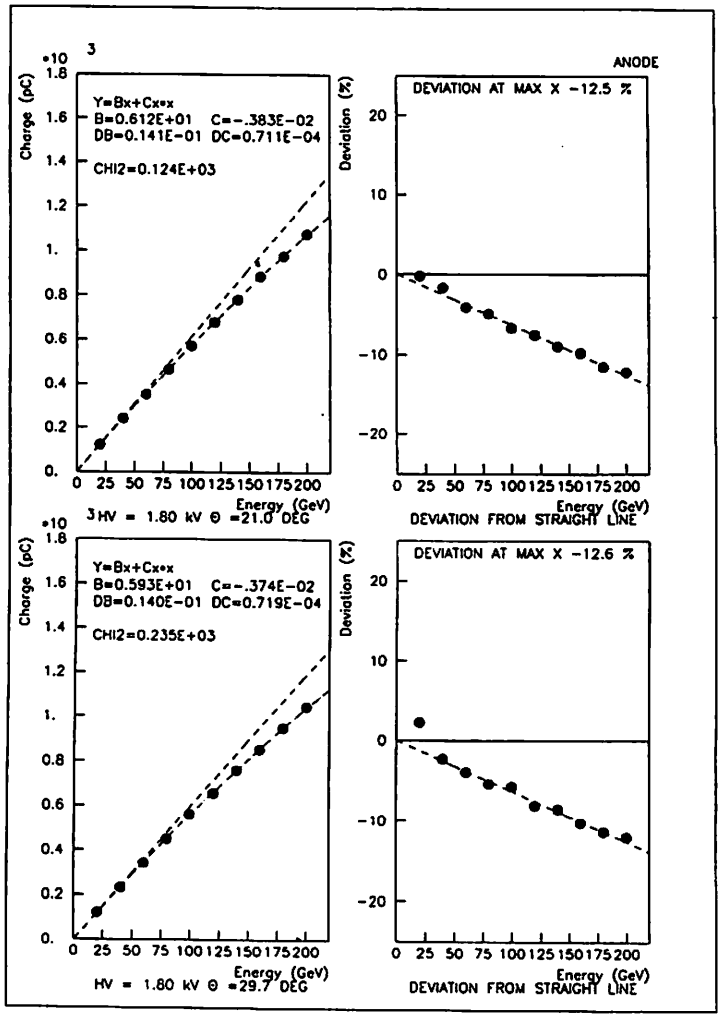

Fig. 3-1-3-12

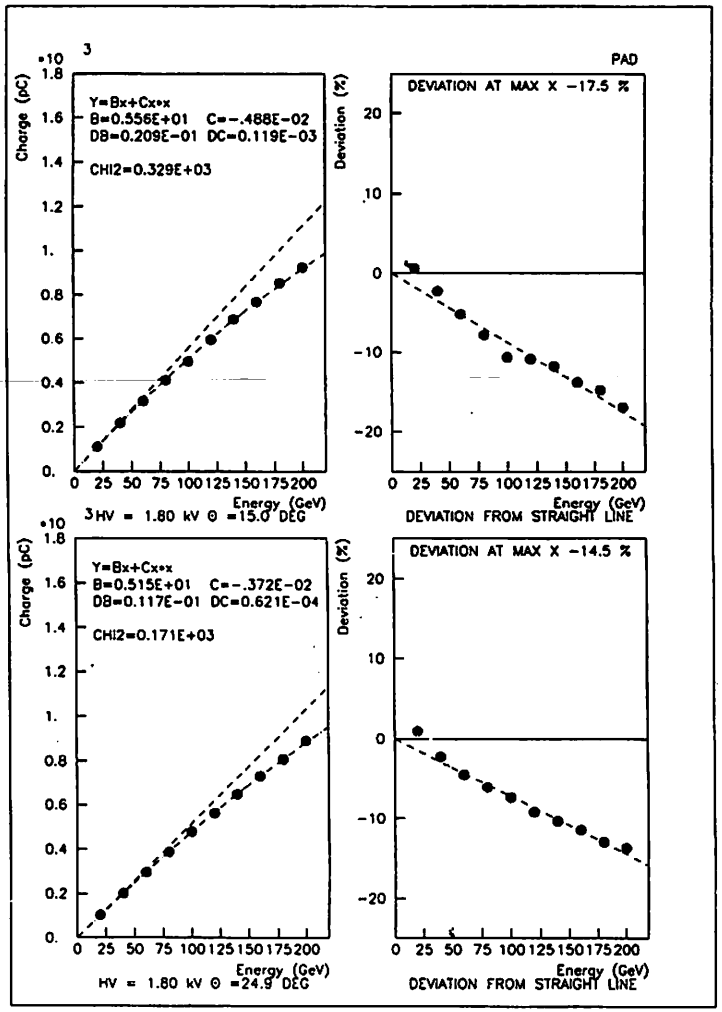

Fig. 3-1-3-13

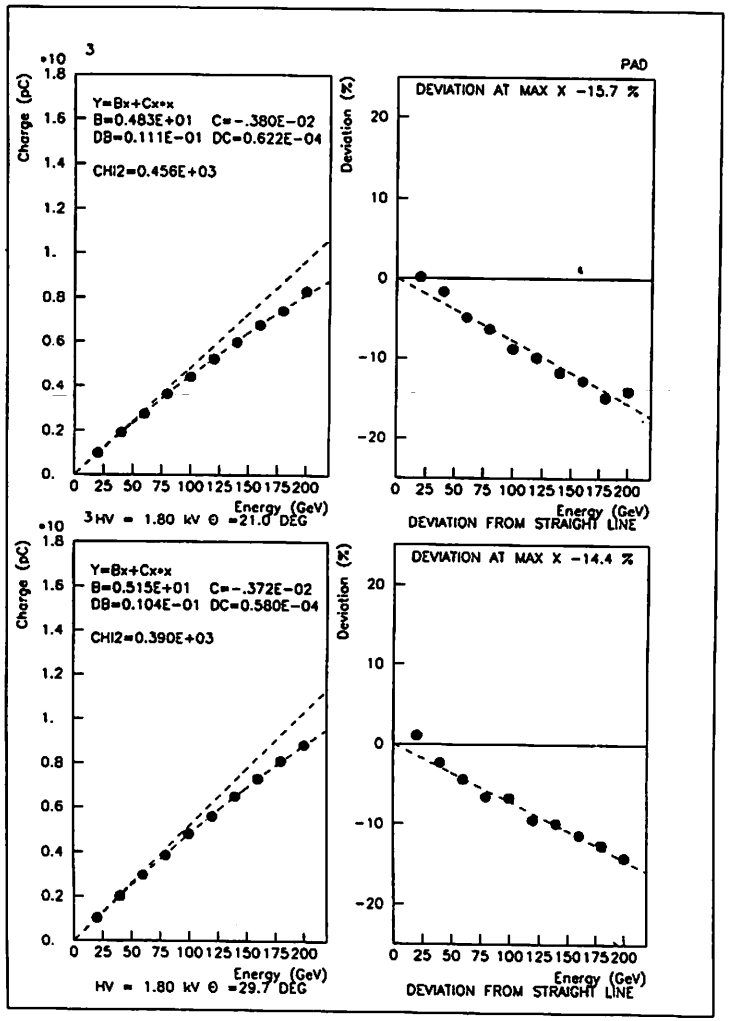

Fig. 3-1-3-14

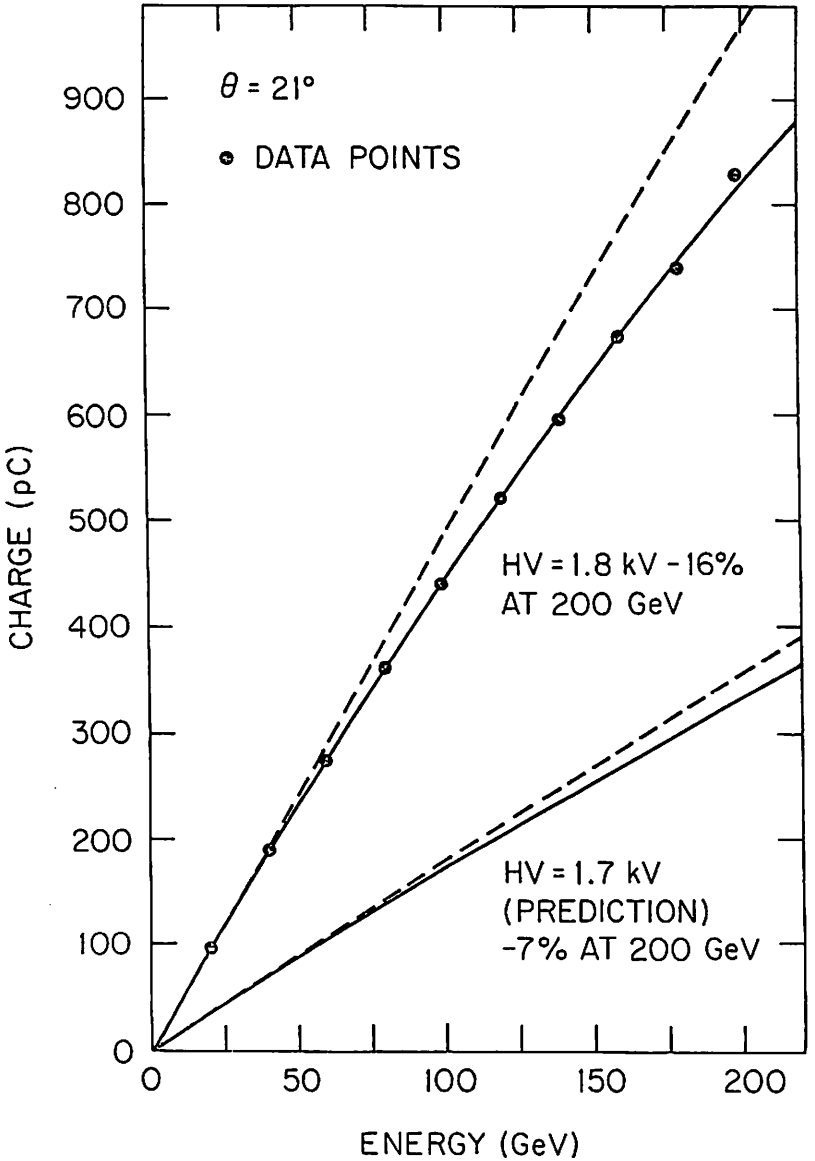

Fig. 3-1-3-15

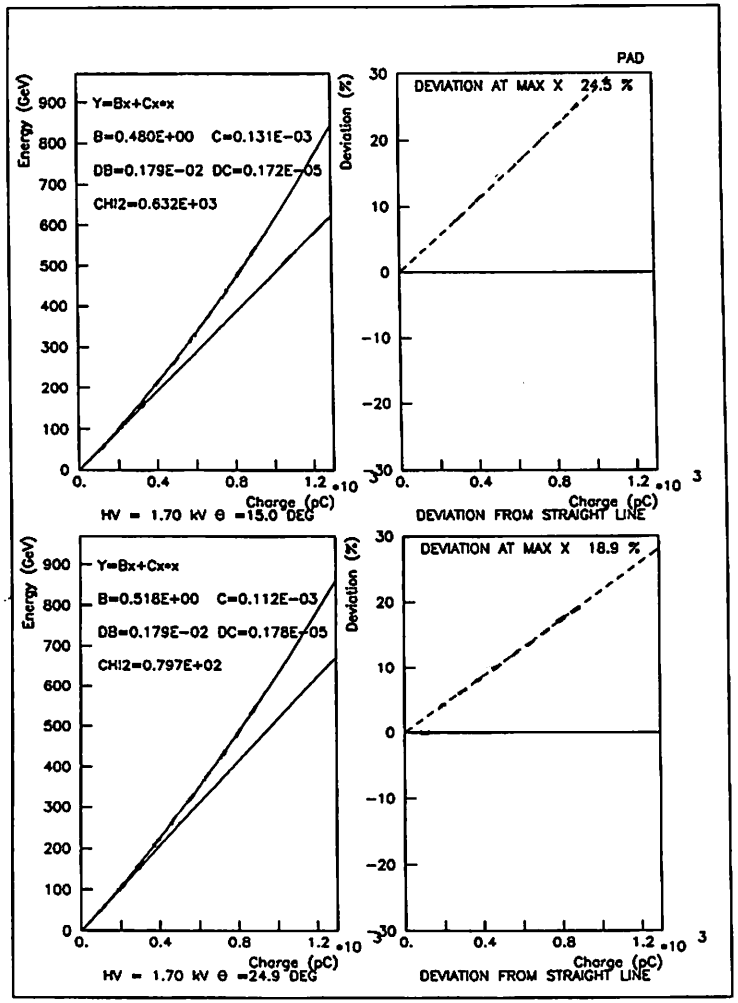

Fig. 3-1-3-16

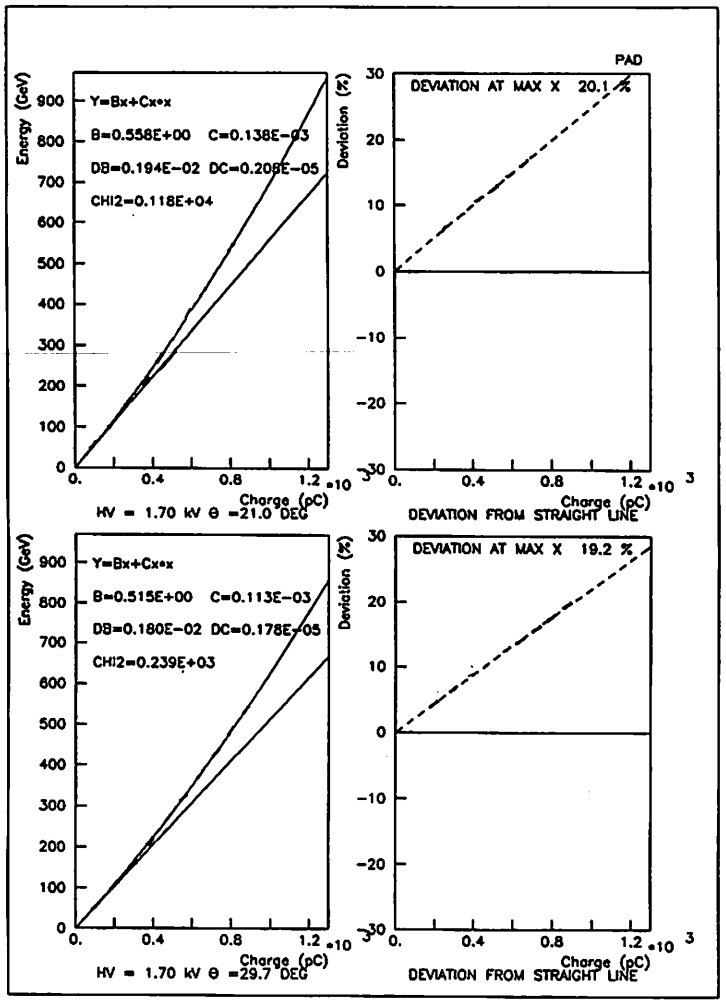

Fig. 3-1-3-17

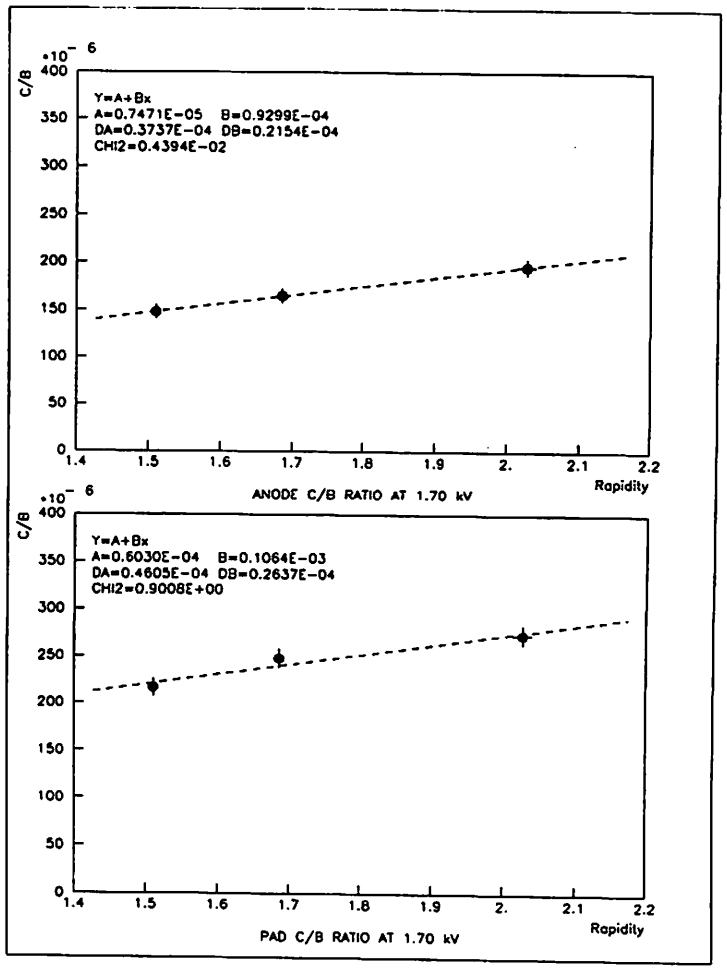

Fig. 3-1-3-18

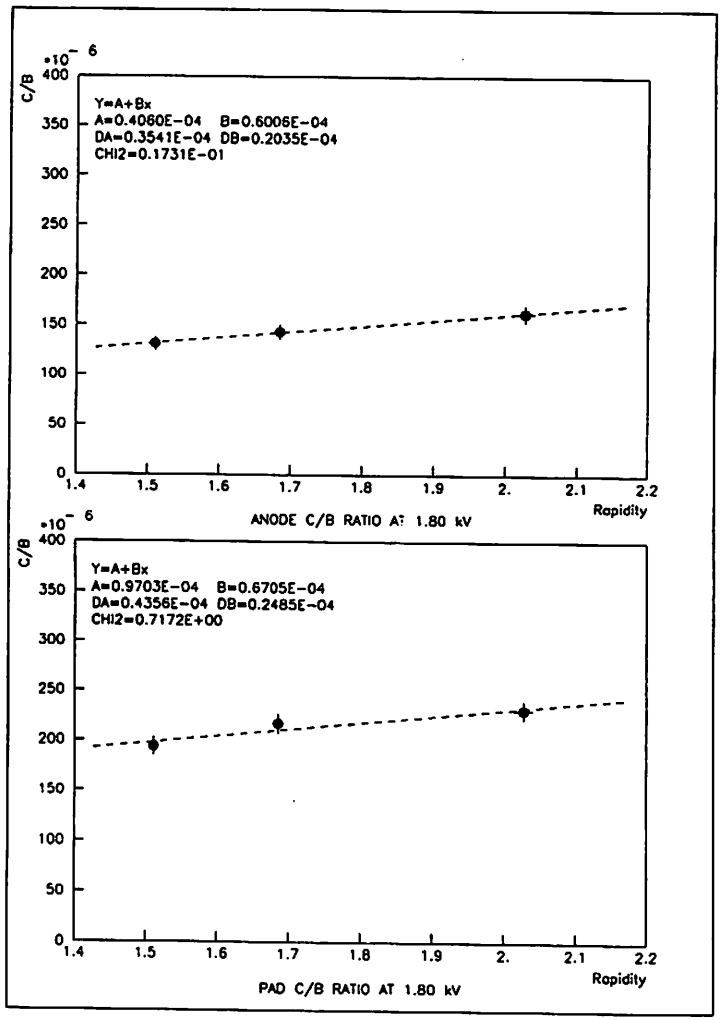

Fig. 3-1-3-19

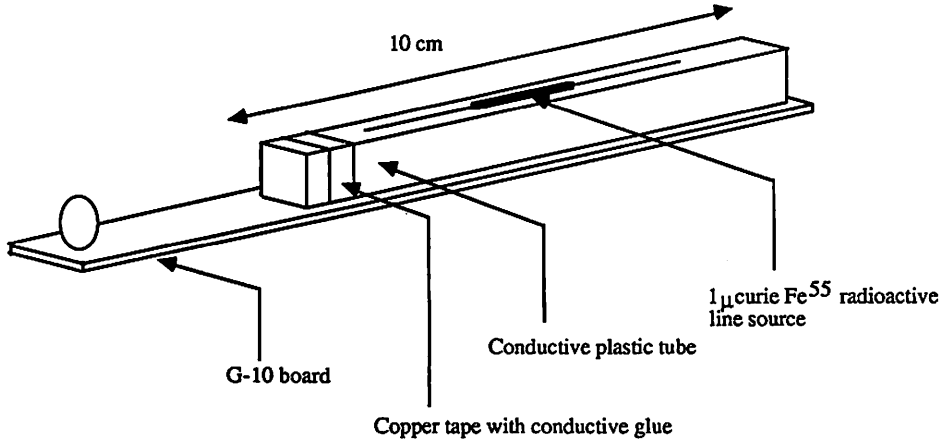

Fig. 3-1-4-1

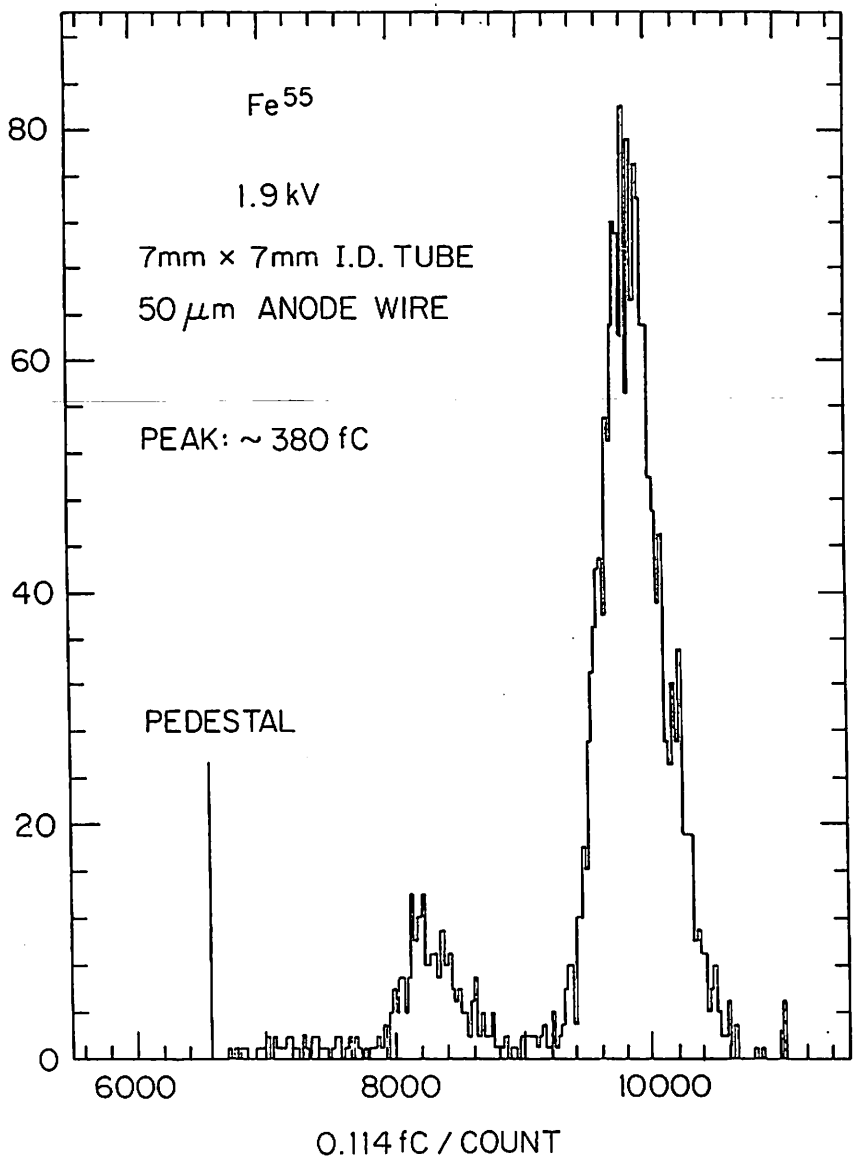

Fig. 3-1-4-2

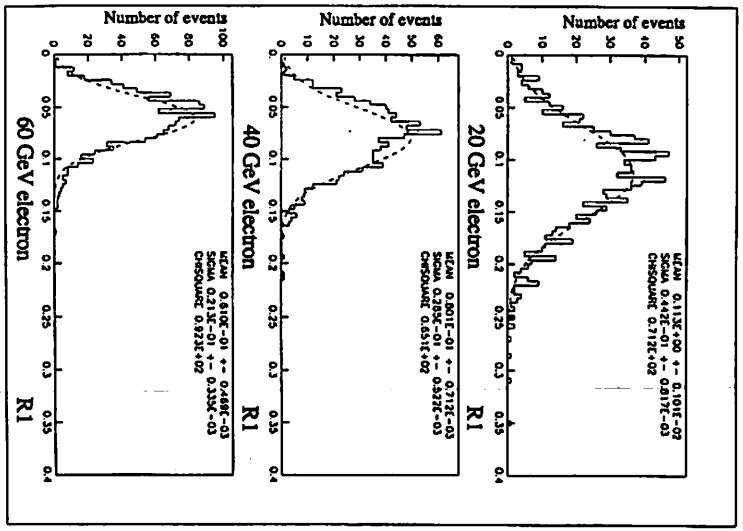

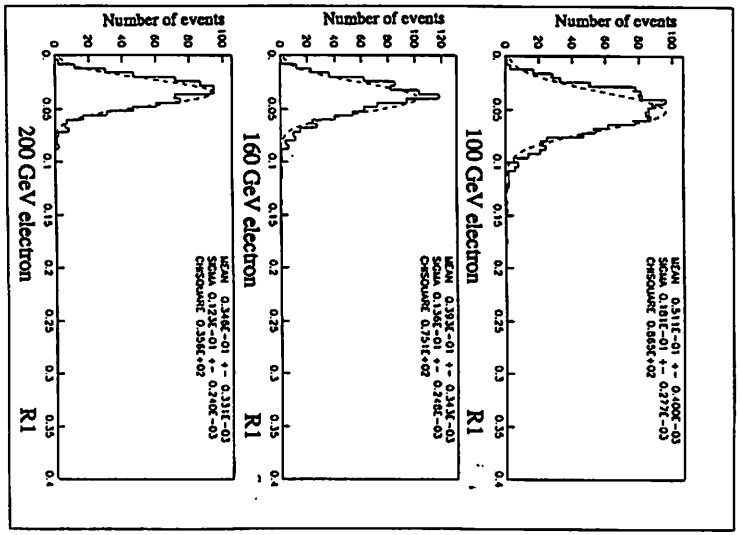

Fig. 3-2-1

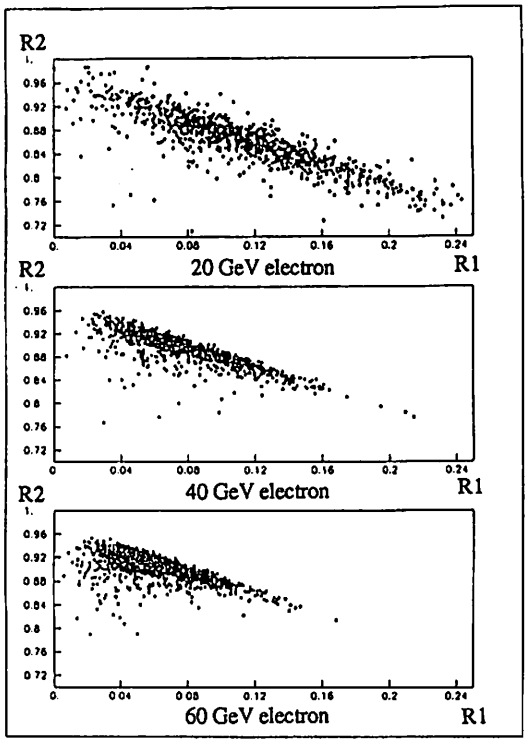

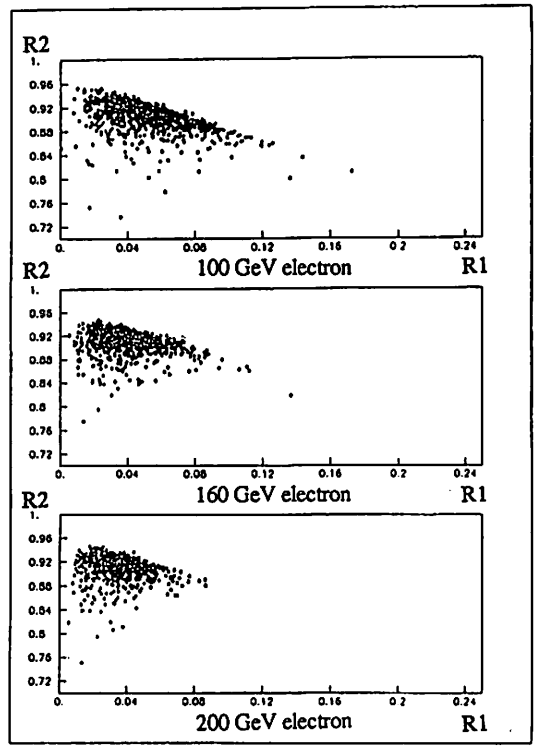

Fig. 3-2-3

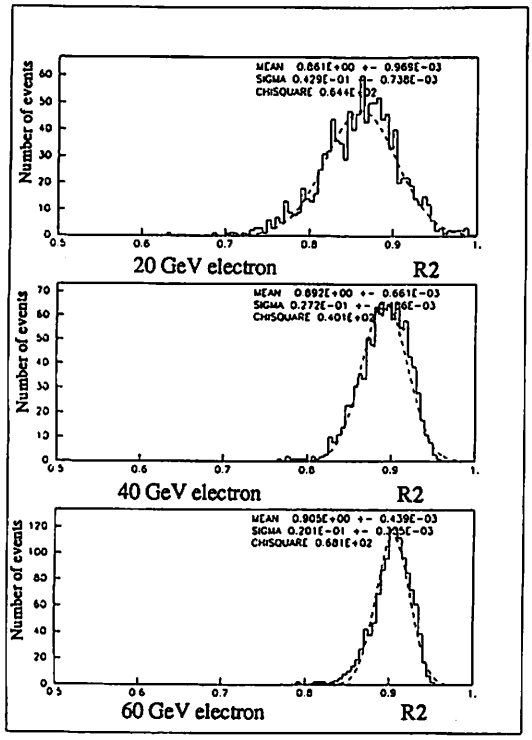

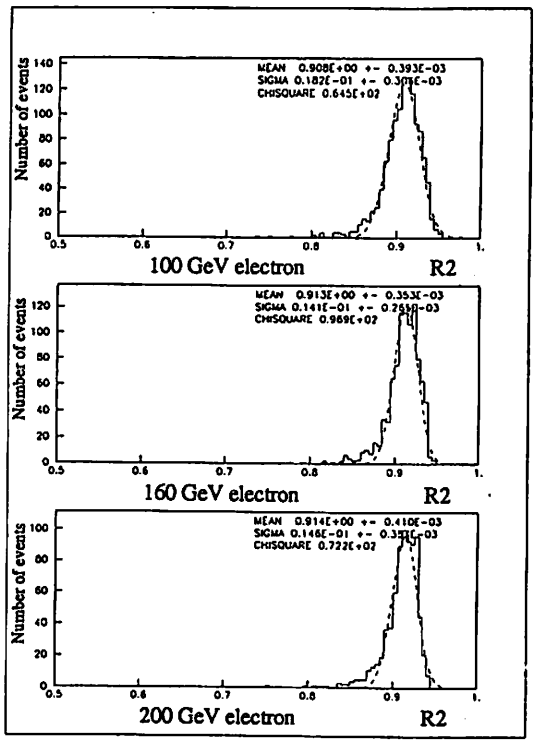

Fig. 3-2-2

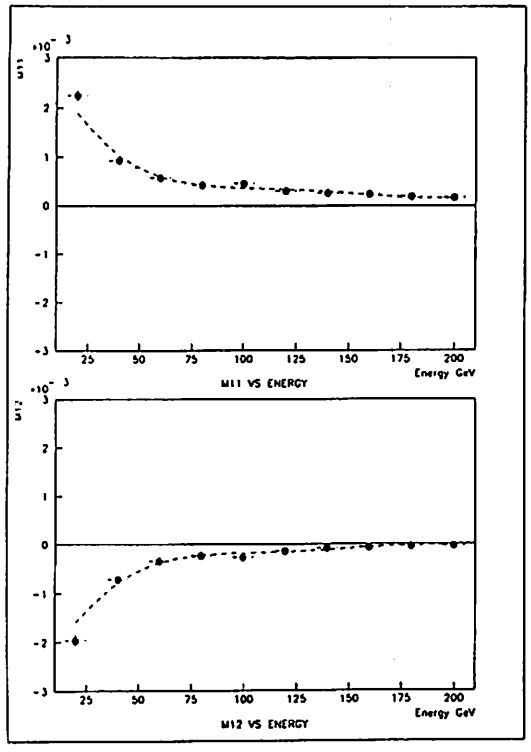

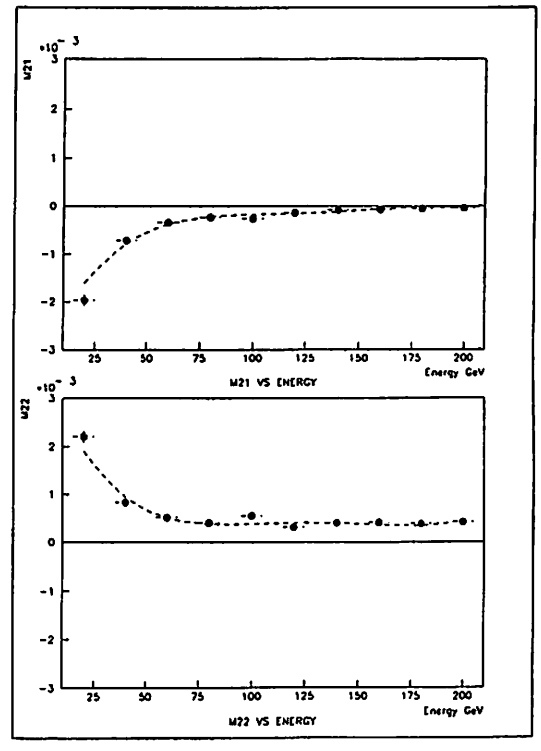

Fig. 3-2-5

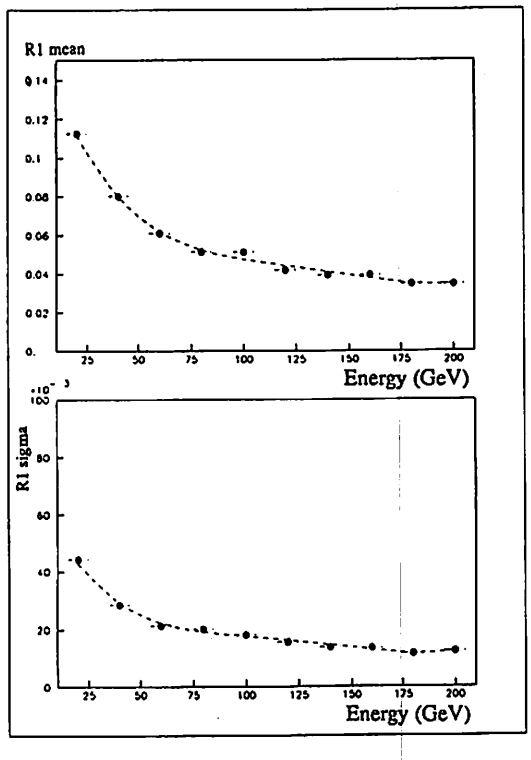

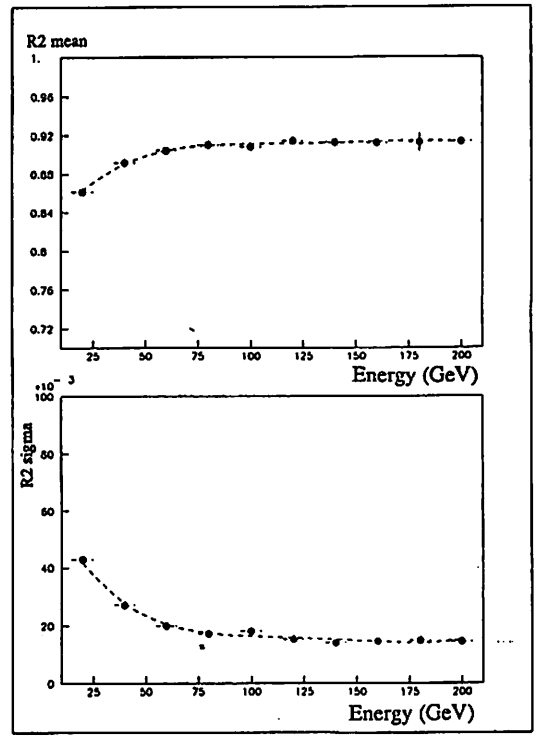

Fig. 3-2-4

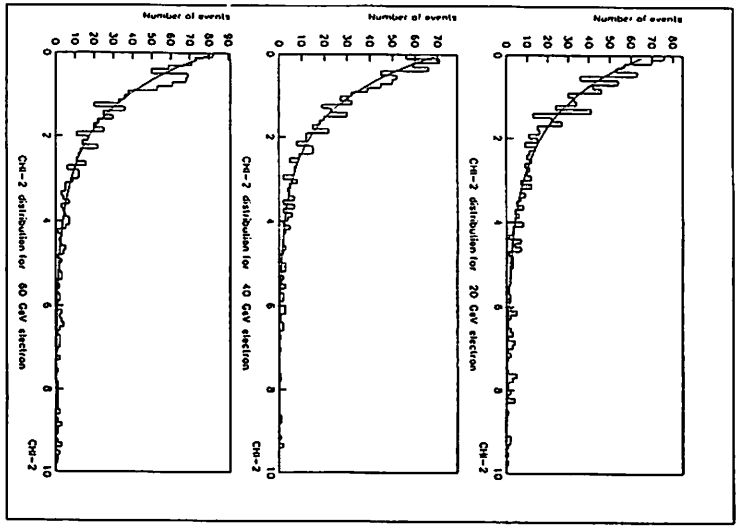

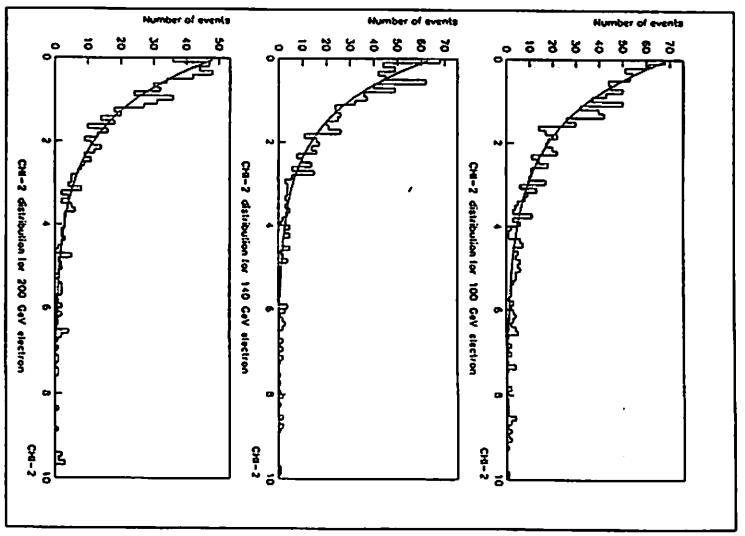

Fig. 3-2-6

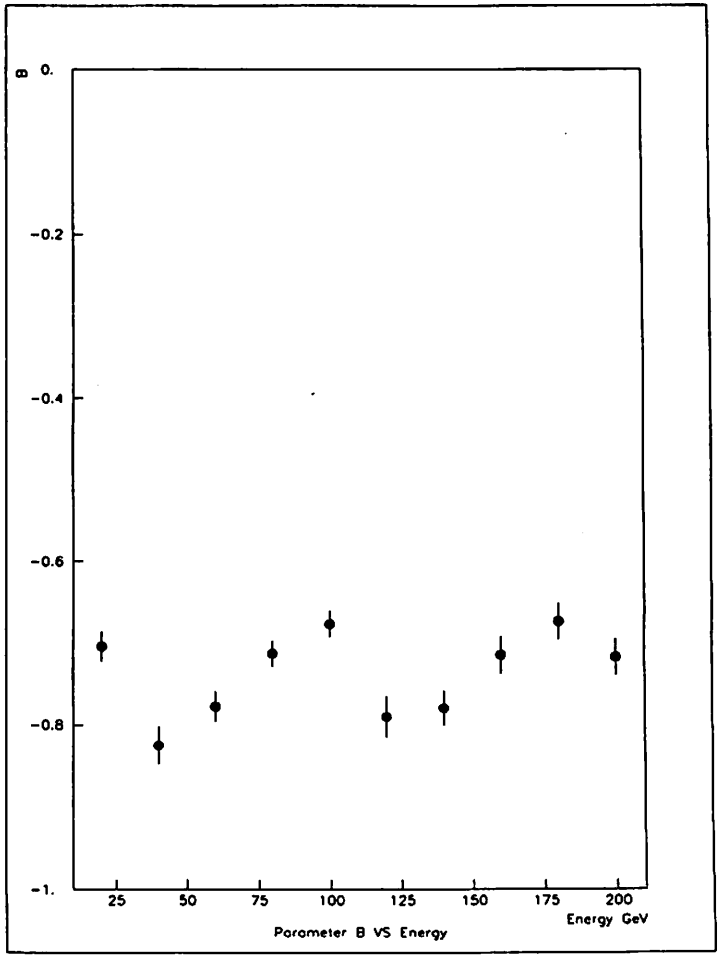

Fig. 3-2-7

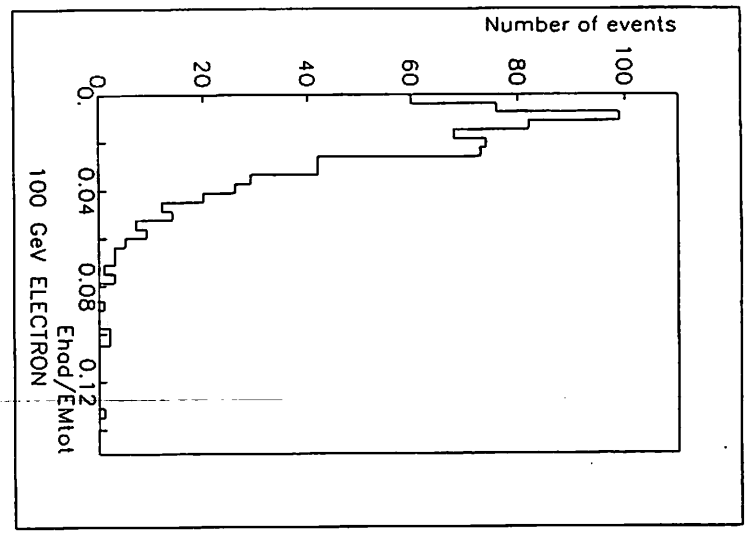

Fig. 3-2-8

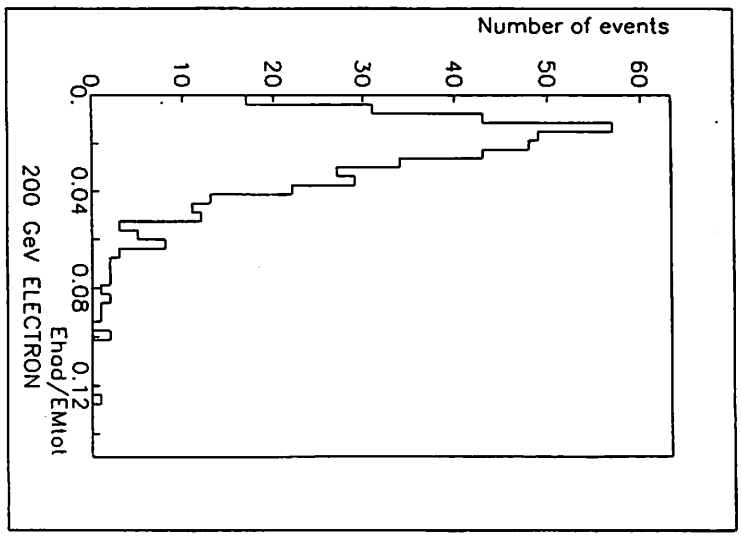

Fig. 3-2-9

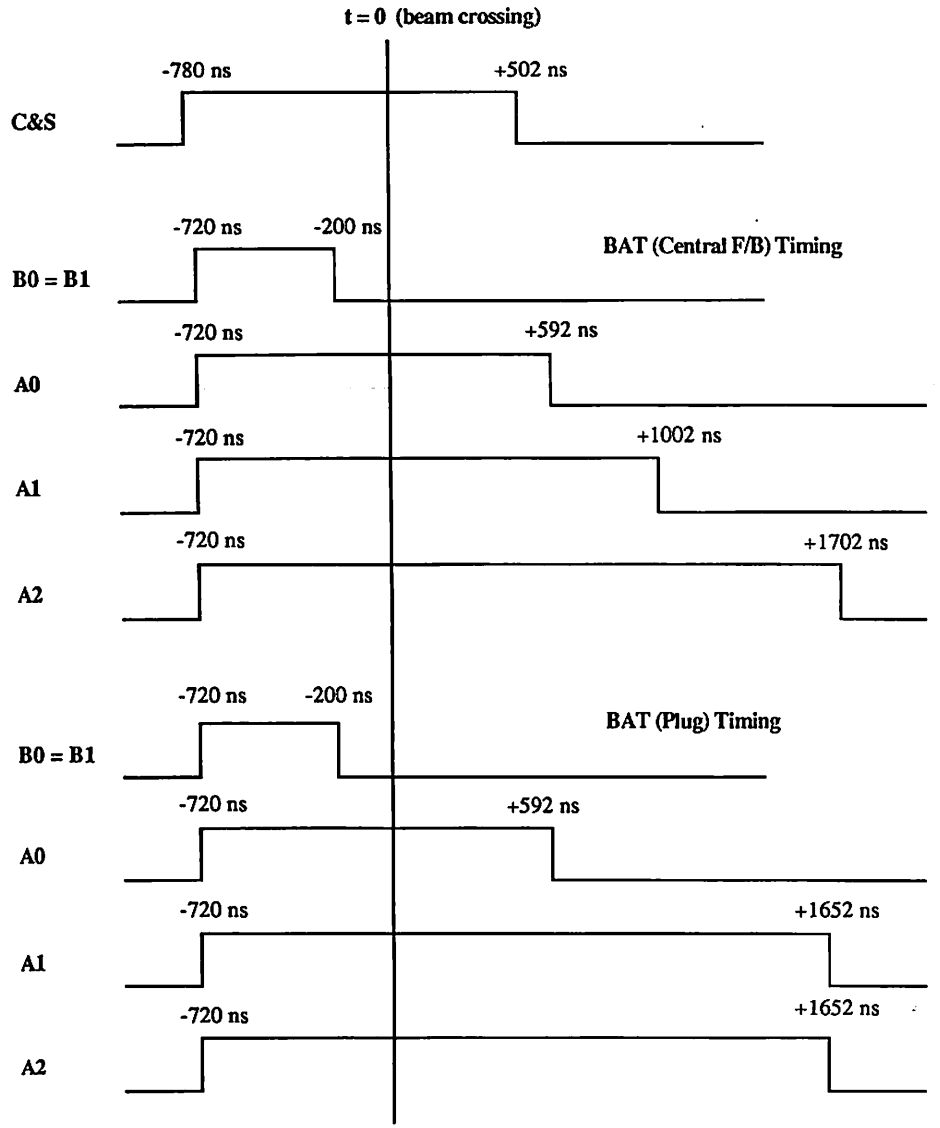

Fig. 4-1-1

Electron clustering algorithm

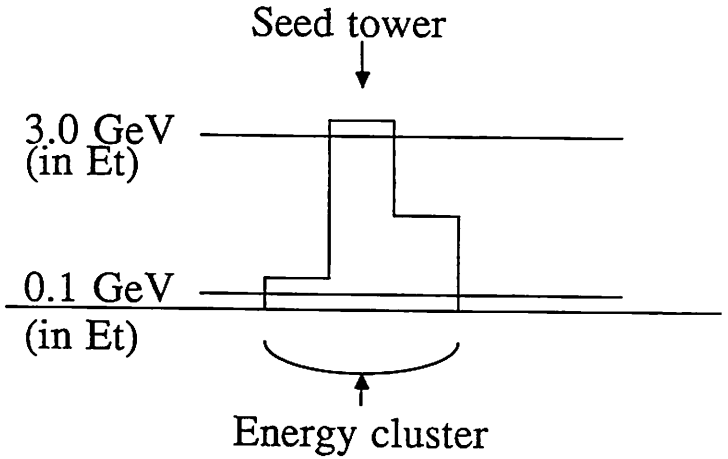

Clustering algorithm in the central EM calorimeter

Seed tower threshold	> 3 GeV
Tower threshold	> 0.1 GeV
No. of towers in η	$\leq$ 3 (seed $\pm$ 1)
No. of towers in φ	= 1

Fig. 5-1-1

ANALYSIS STREAM

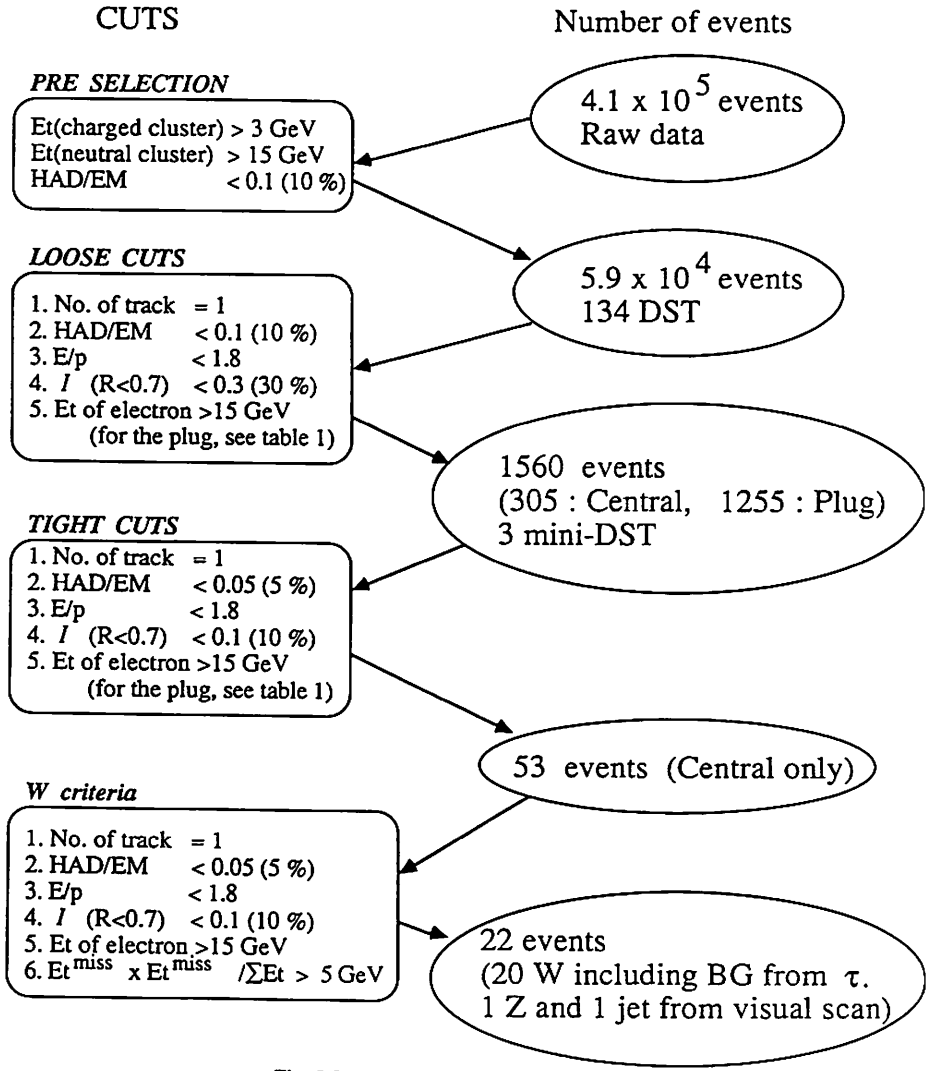

Fig. 5-3-1

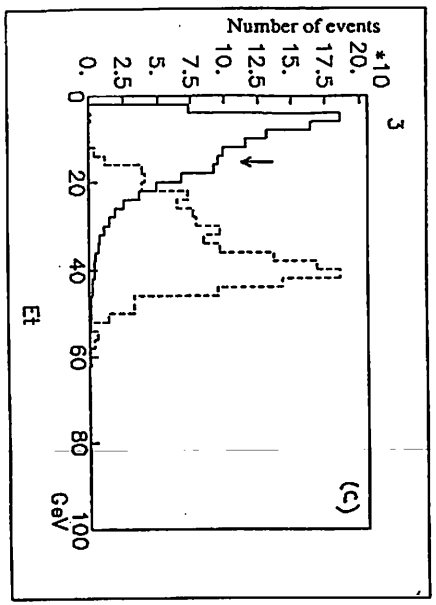

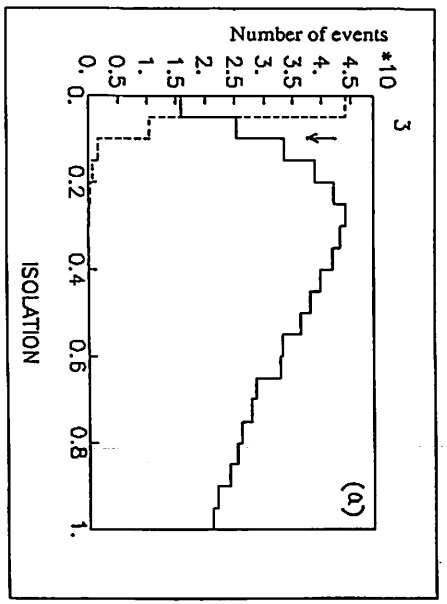

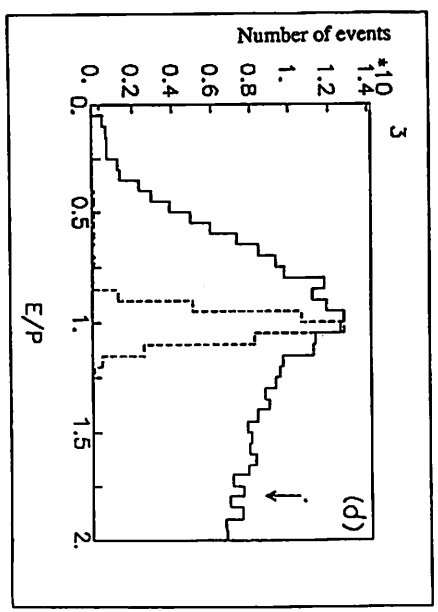

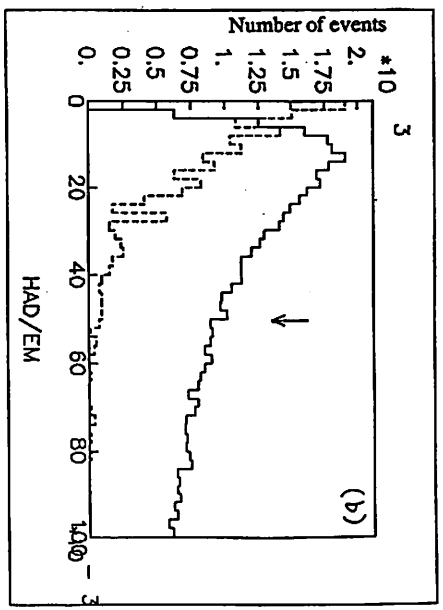

Fig. 5-3-2

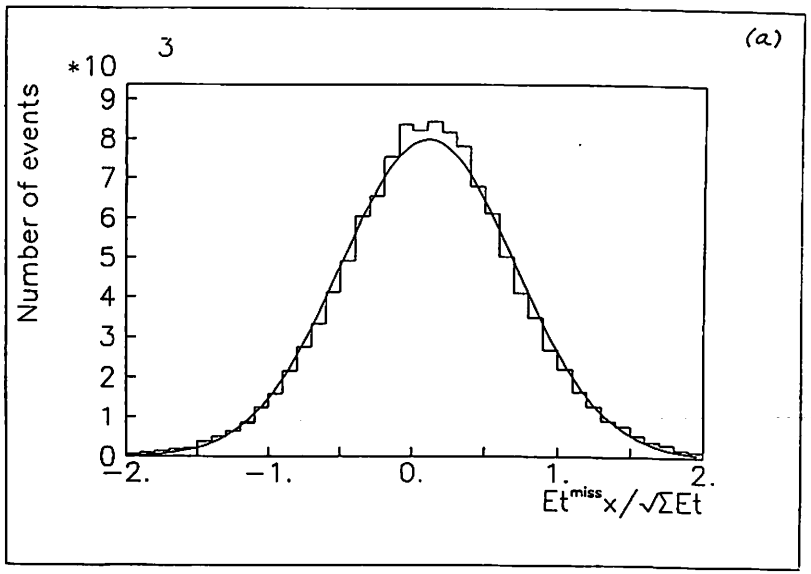

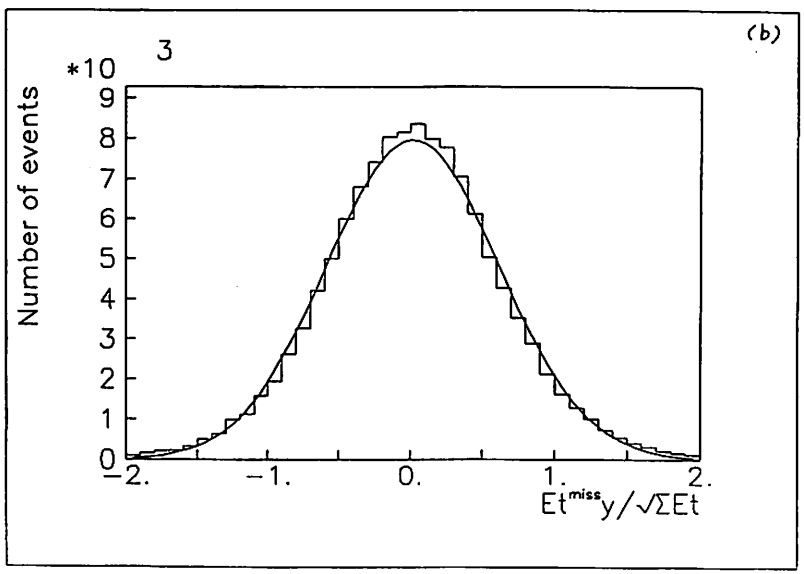

Fig. 5-3-3

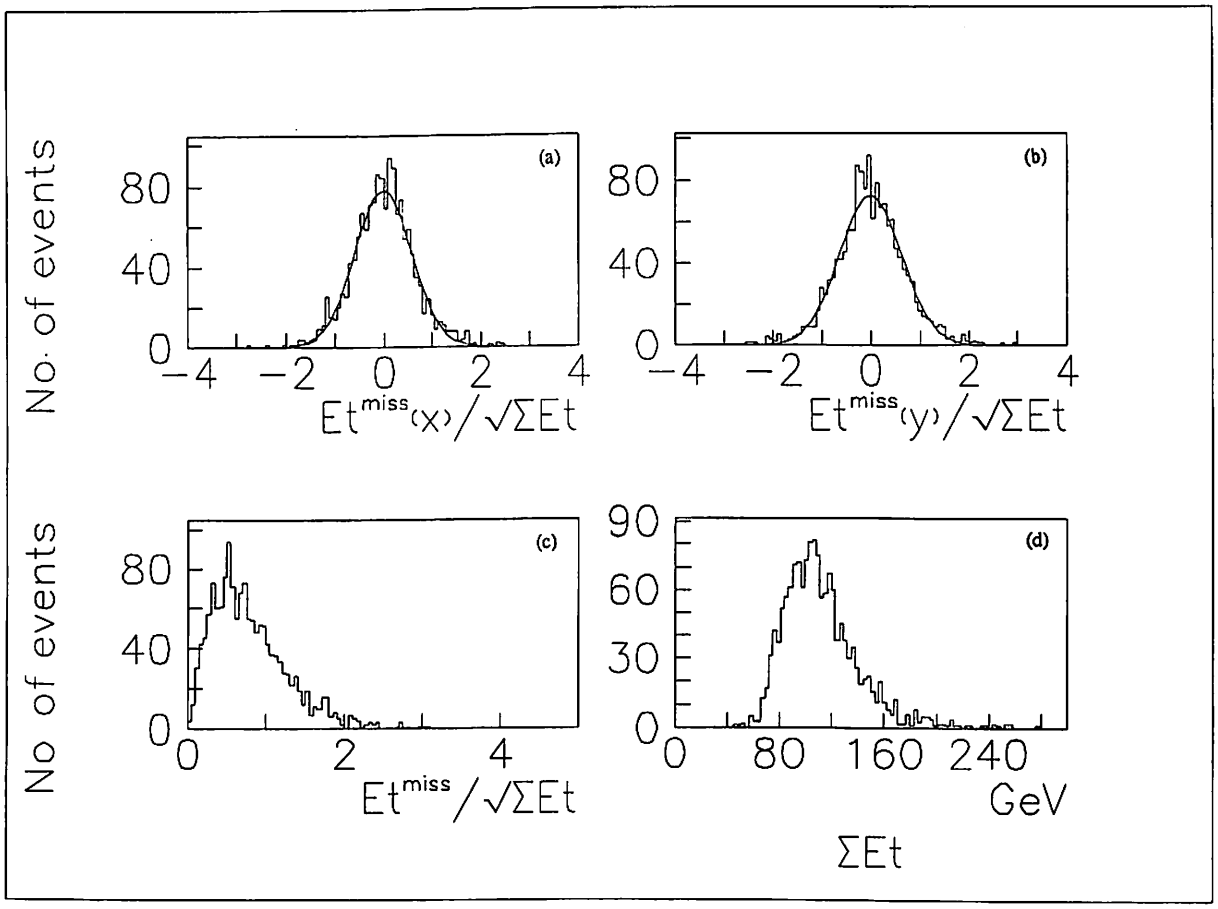

Fig. 5-3-5

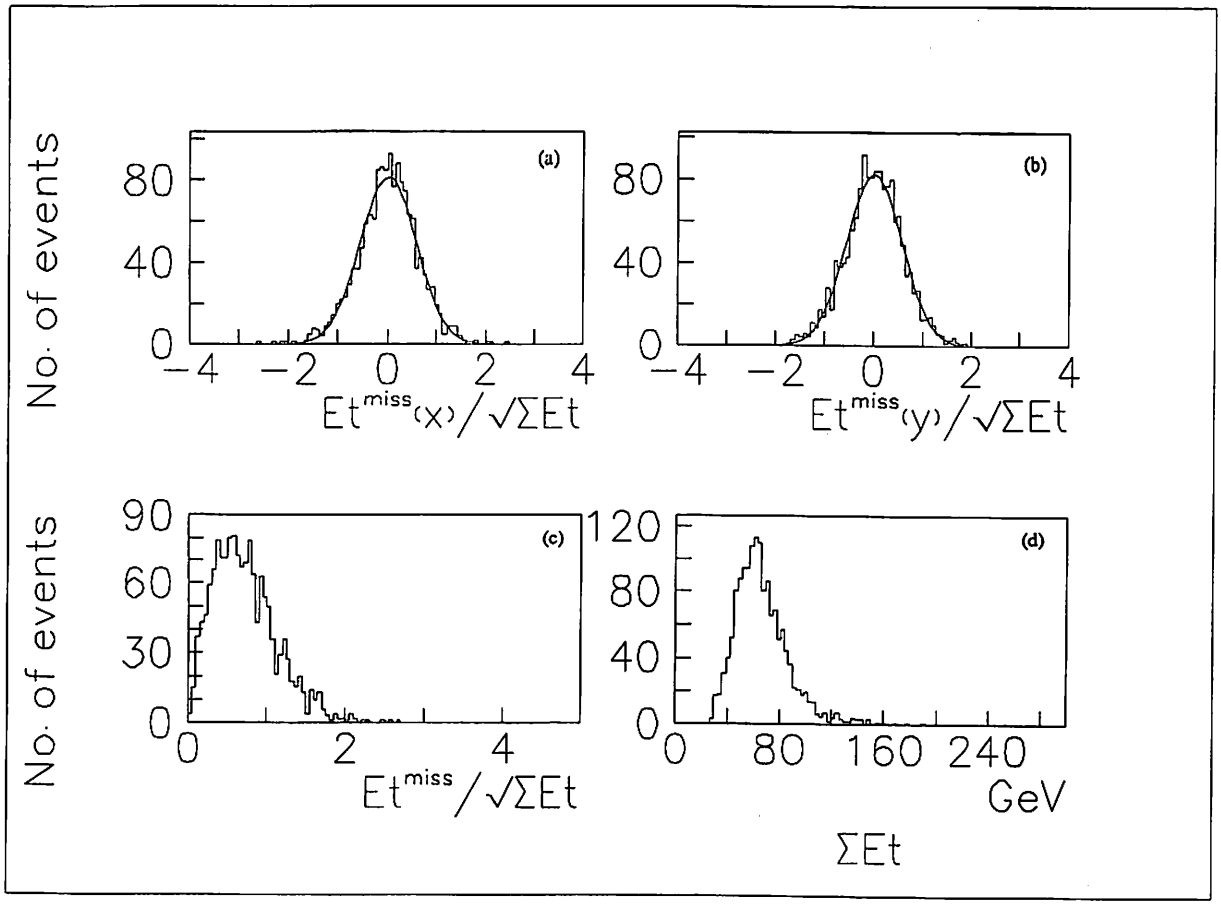

Fig. 5-3-4

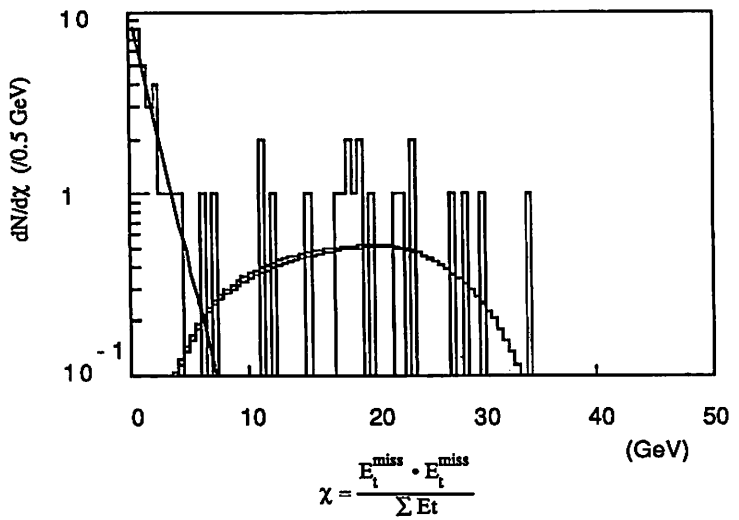

Fig. 5-4-1

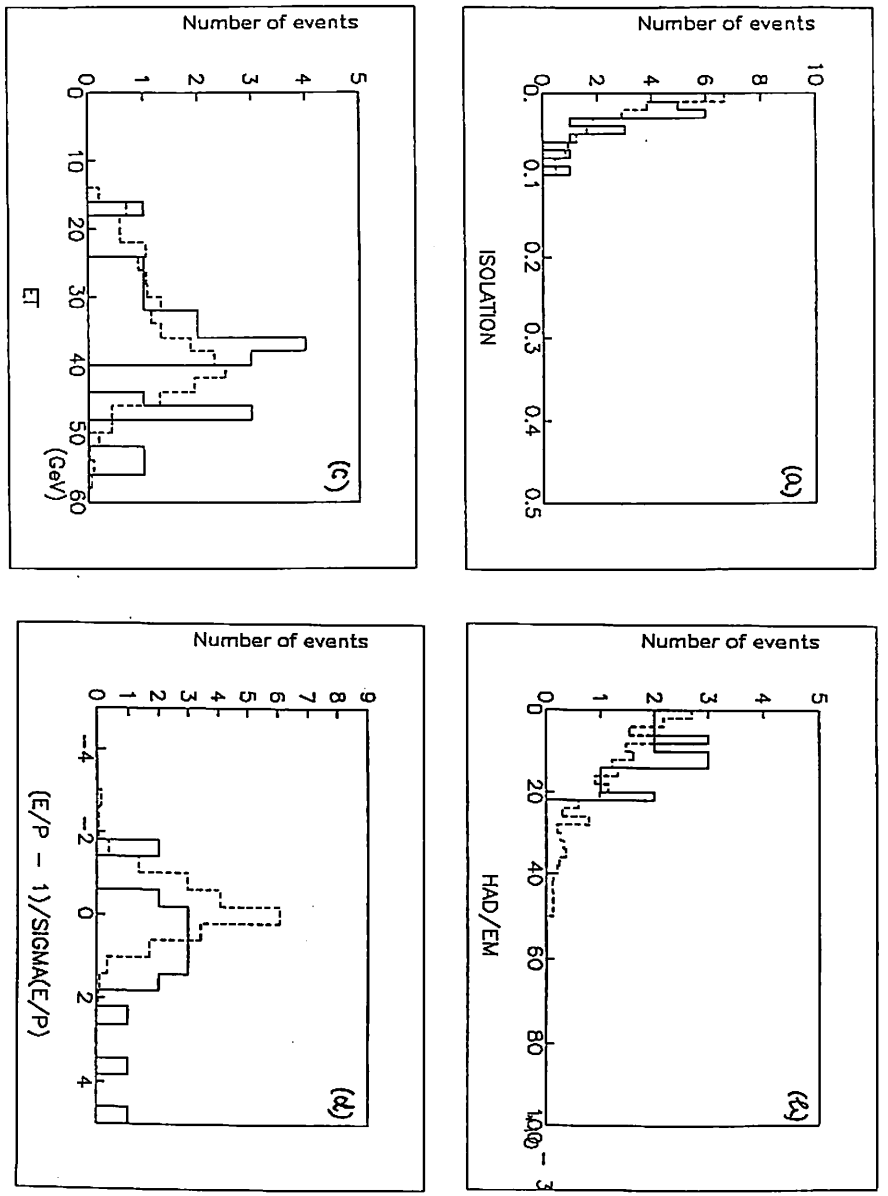

Fig. 5-4-2

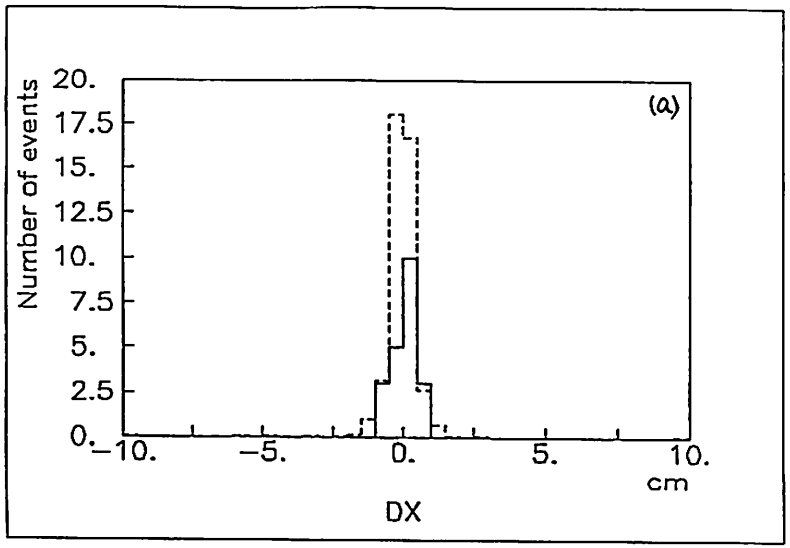

Fig. 5-4-3 (a)

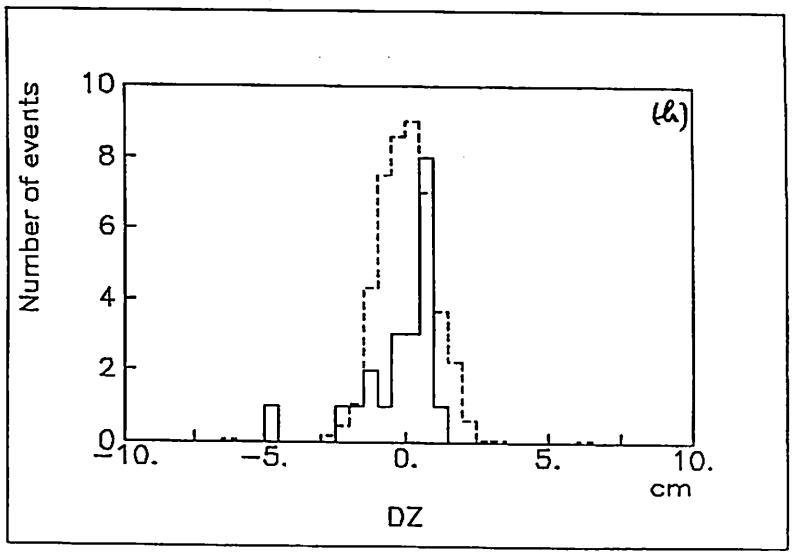

Fig. 5-4-3 (b)

ISOLATION

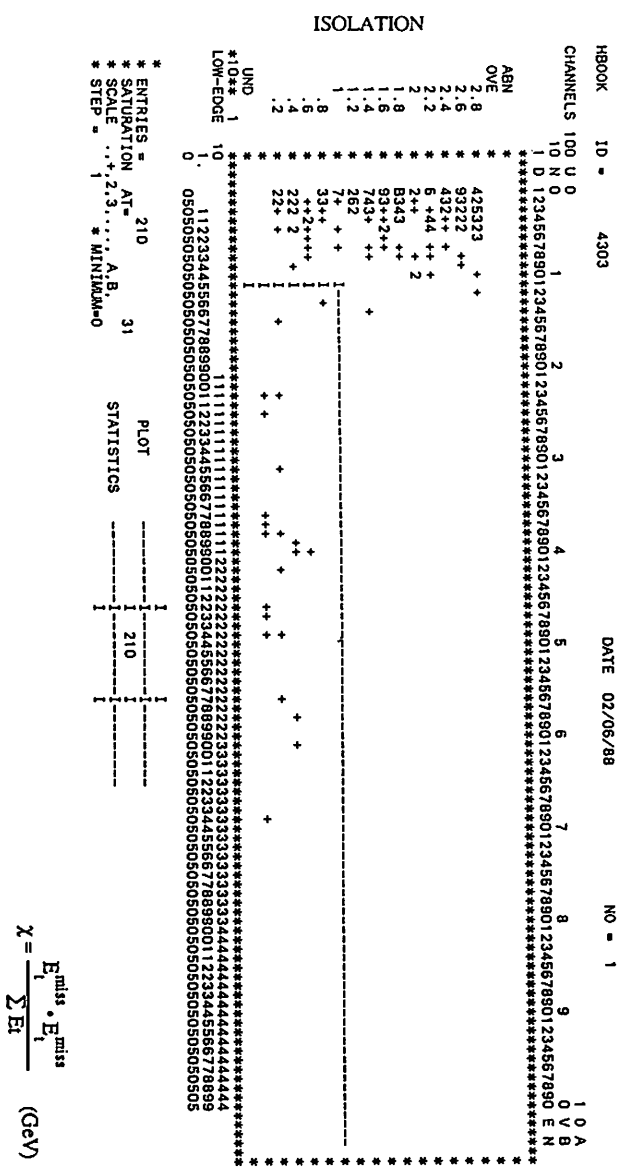

$$\chi = \frac{E_t^{miss} \cdot E_t^{miss}}{\Sigma Et} \quad (GeV)$$

Fig. 5-5-1

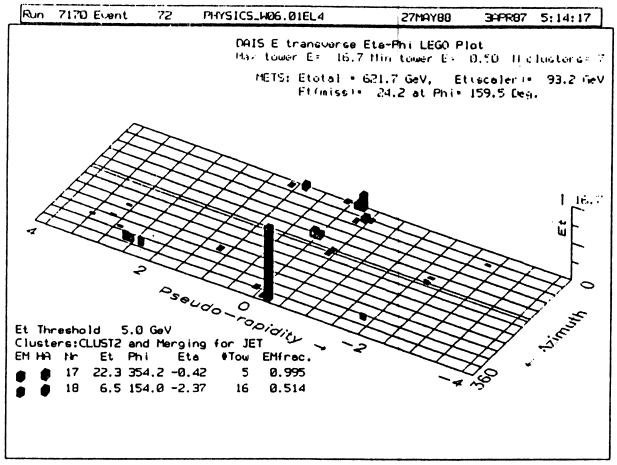

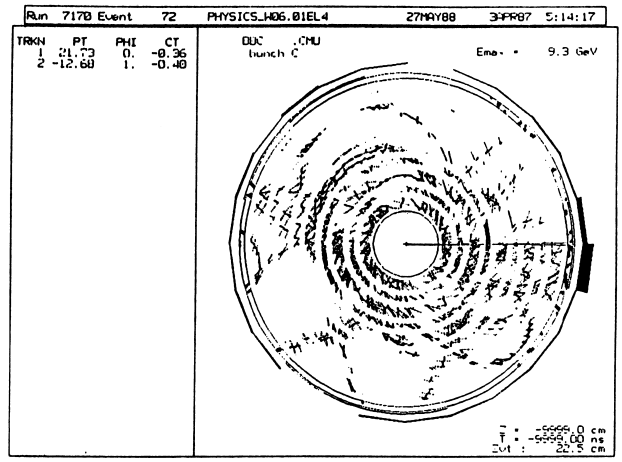

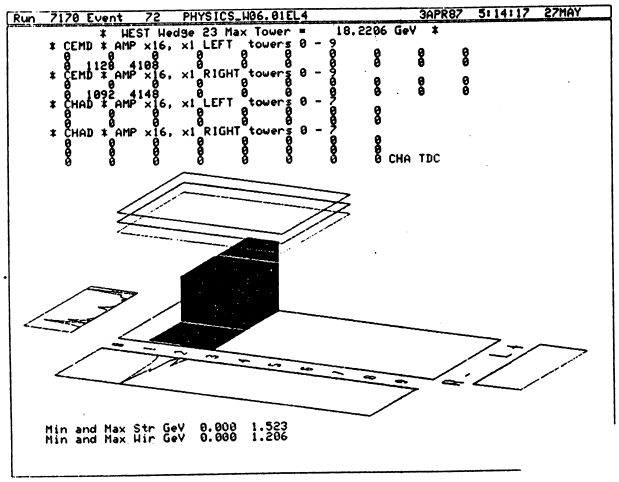

Fig. 5-5-3 (1)

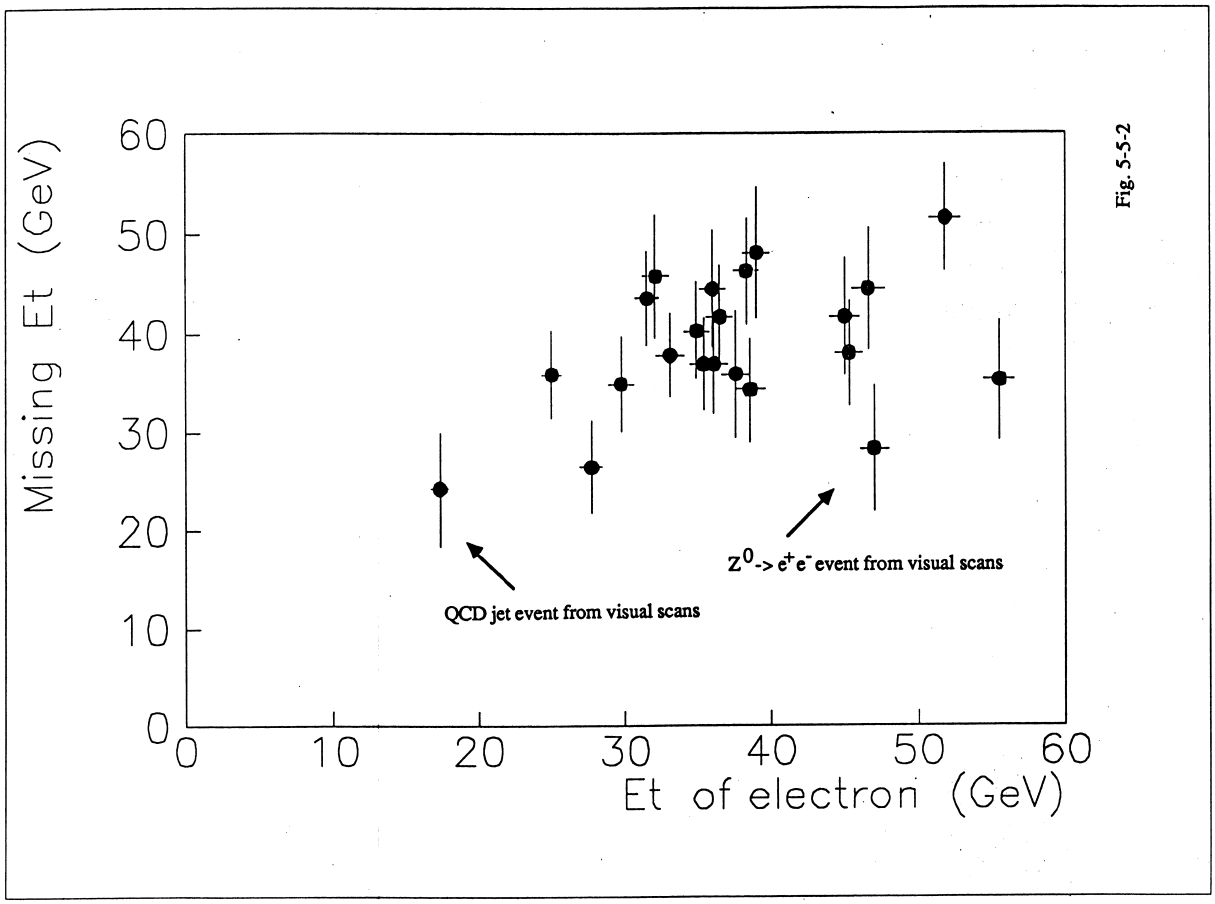

Fig. 5-5-2

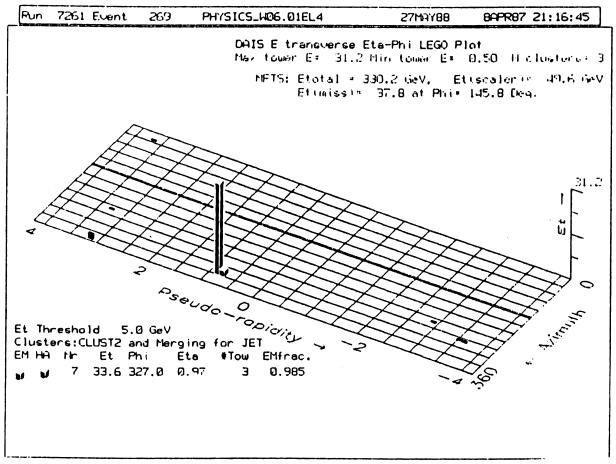

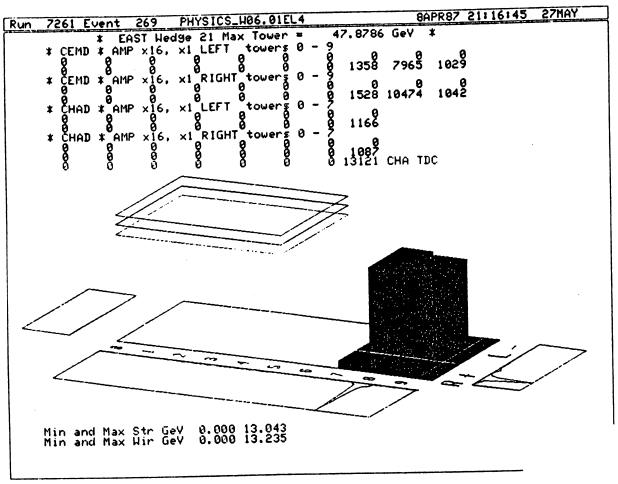

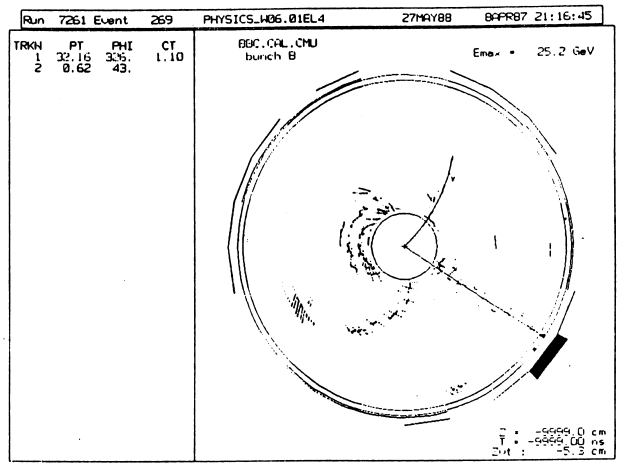

Fig. 5-5-3 (3)

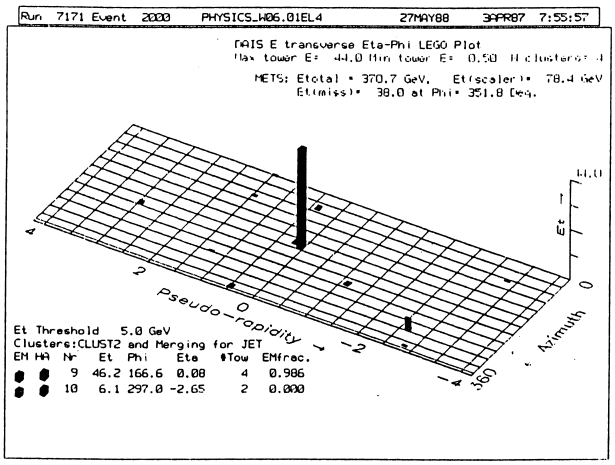

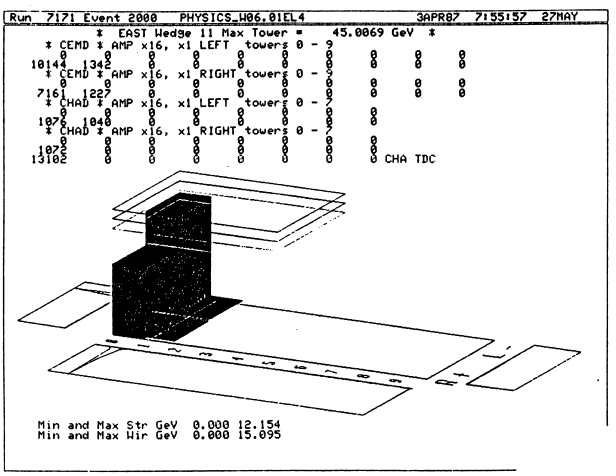

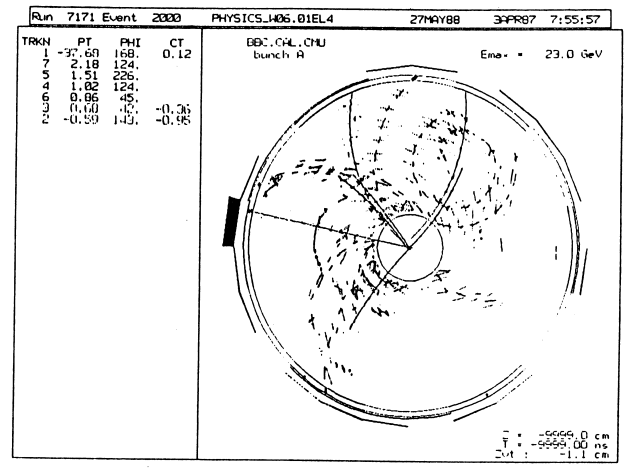

Fig. 5-5-3 (2)

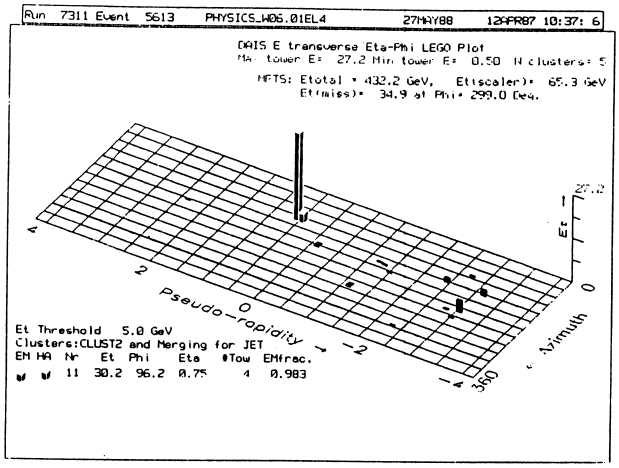

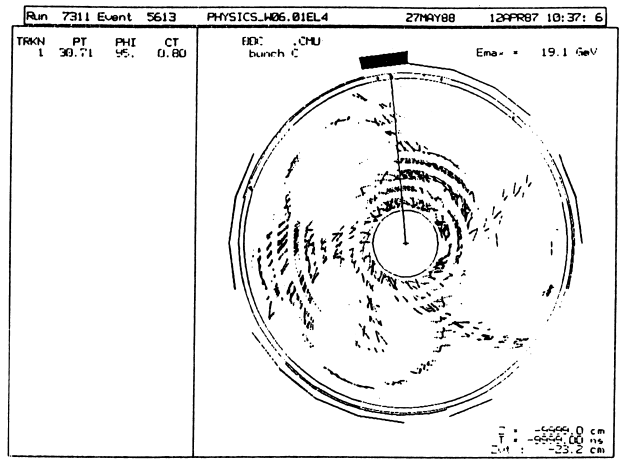

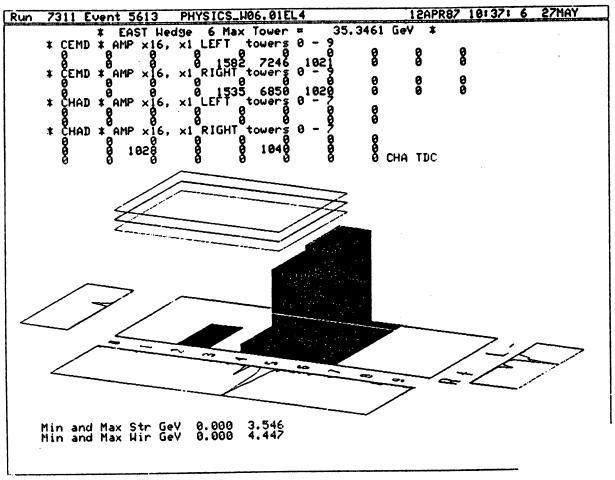

Fig. 5-5-3 (5)

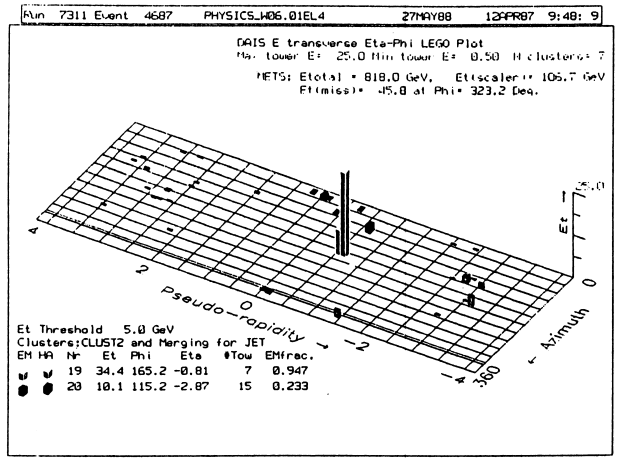

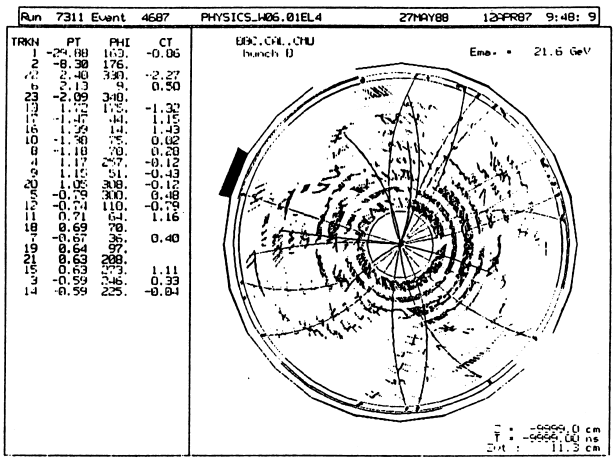

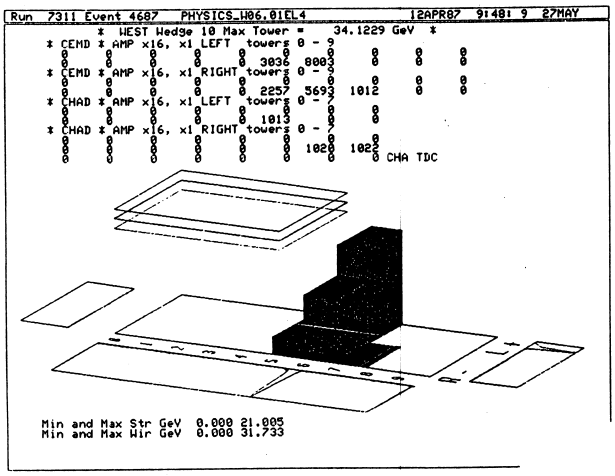

Fig. 5-5-3 (4)

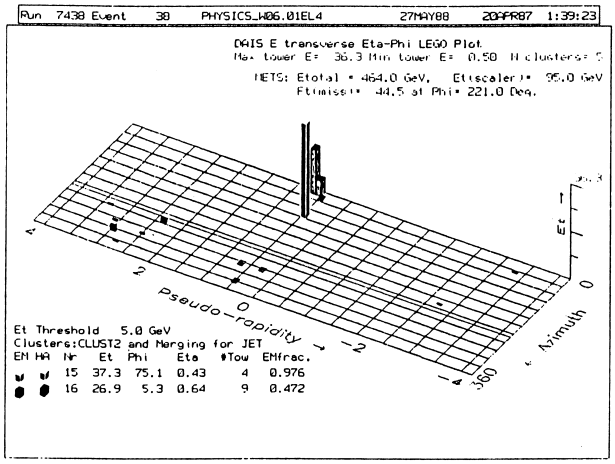

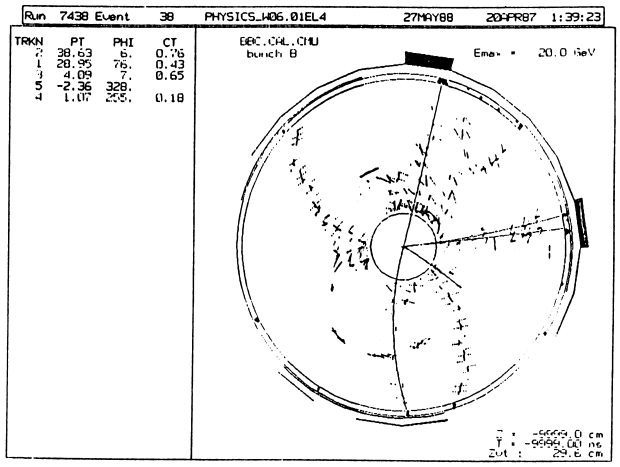

Fig. 5-5-3 (7)

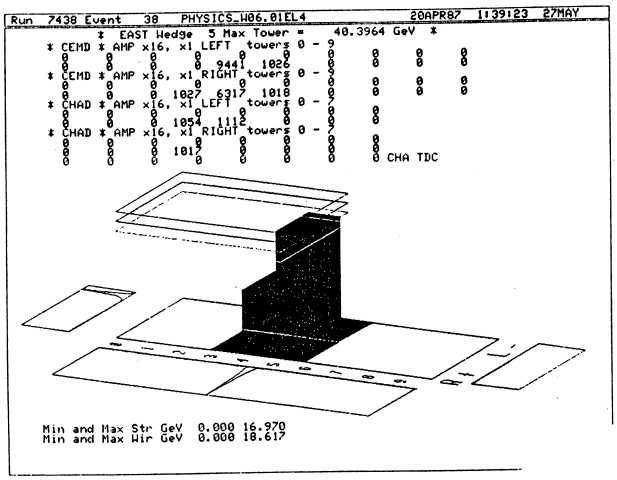

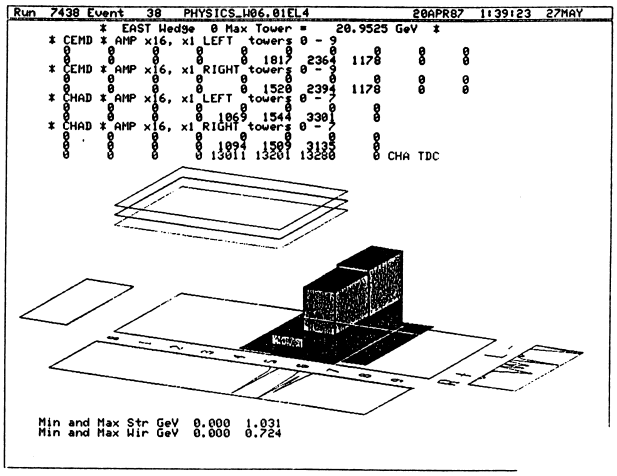

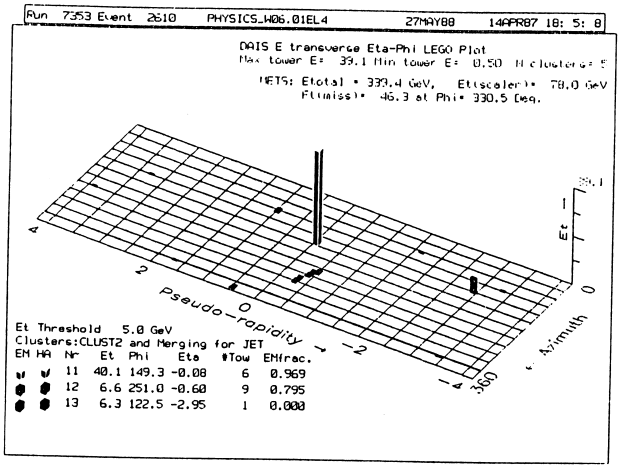

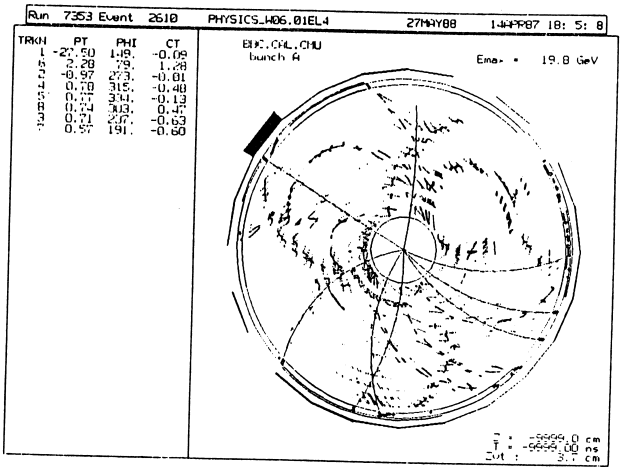

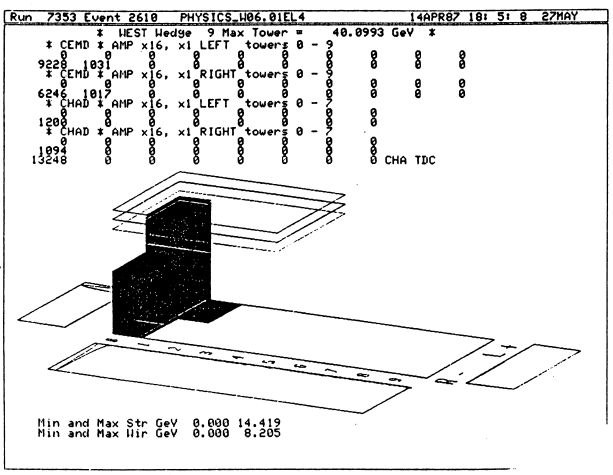

Fig. 5-5-3 (6)

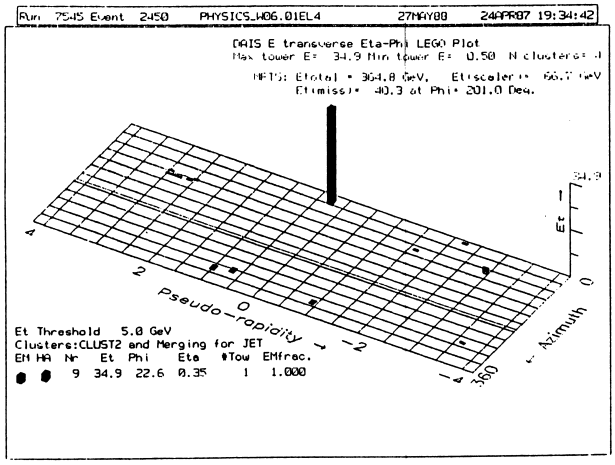

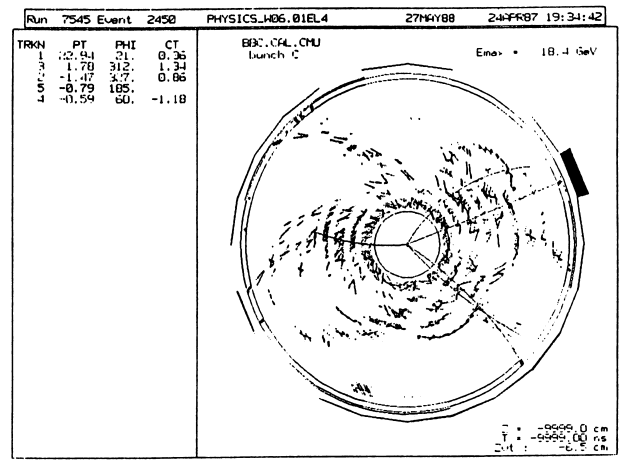

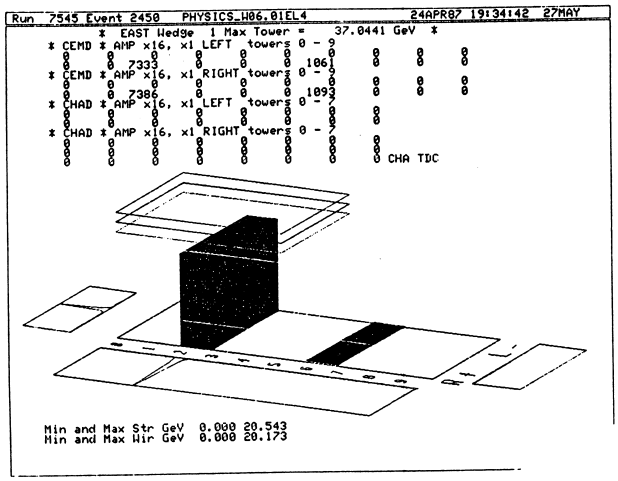

Fig. 5-5-3 (9)

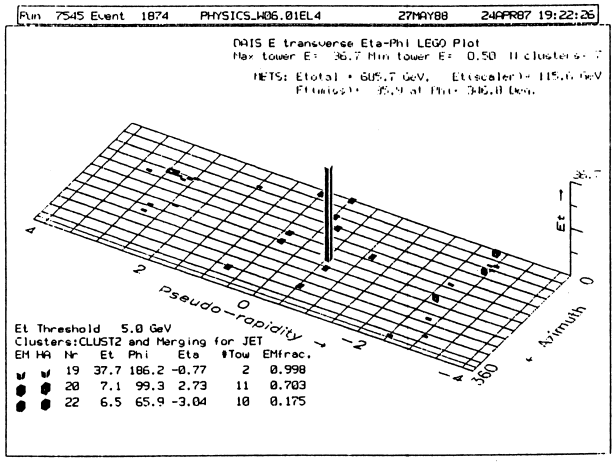

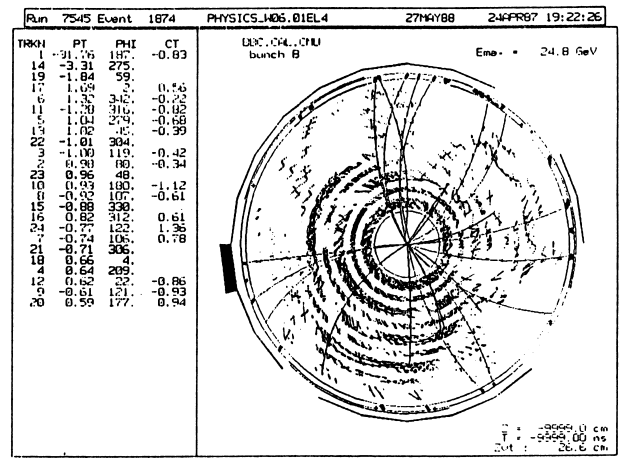

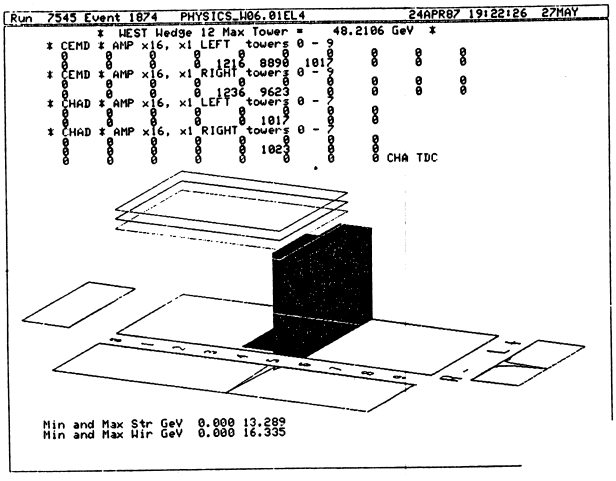

Fig. 5-5-3 (8)

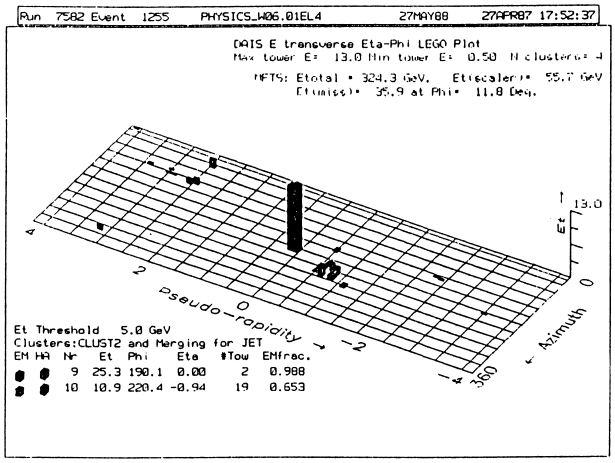

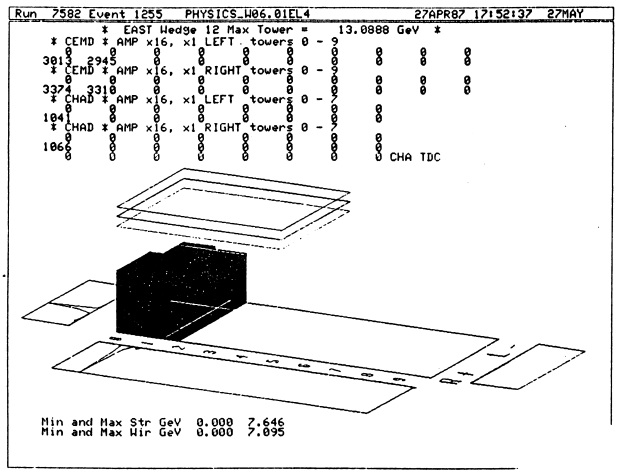

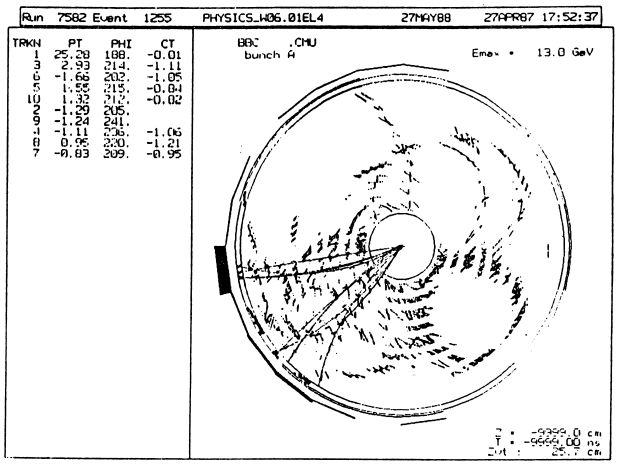

Fig. 5-5-3 (11)

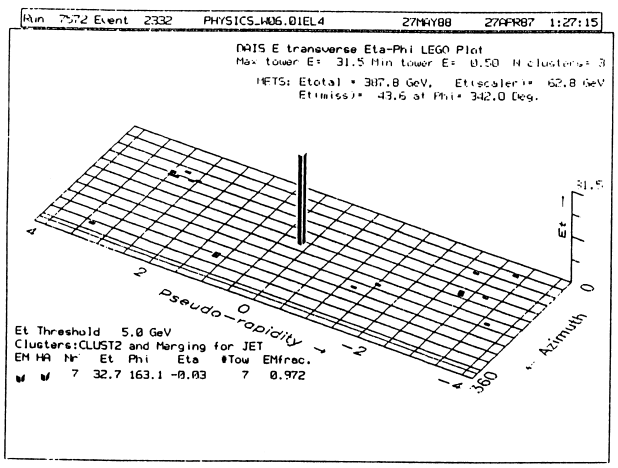

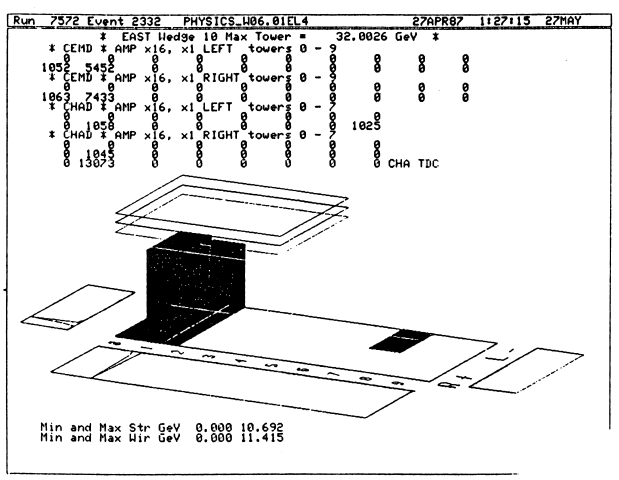

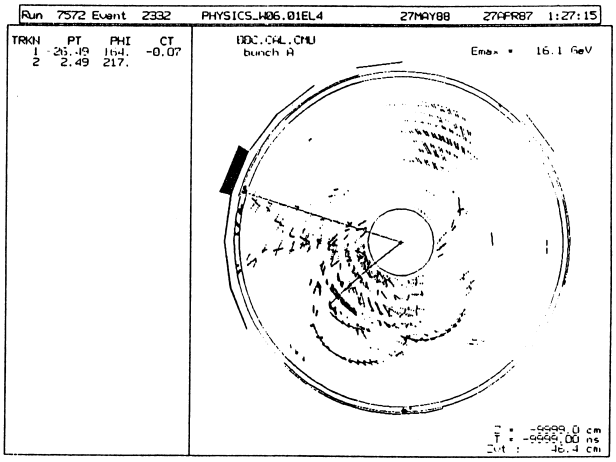

Fig. 5-5-3 (10)

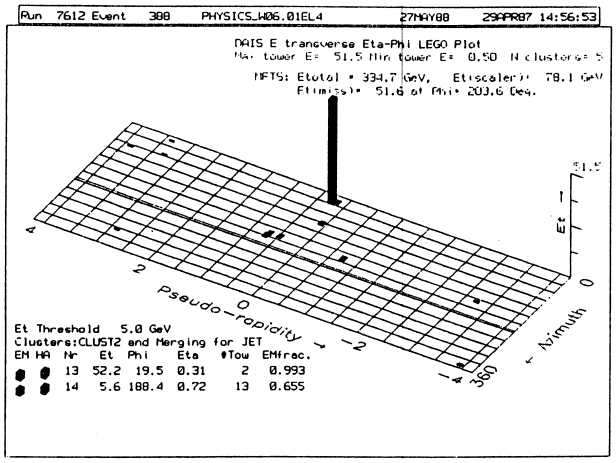

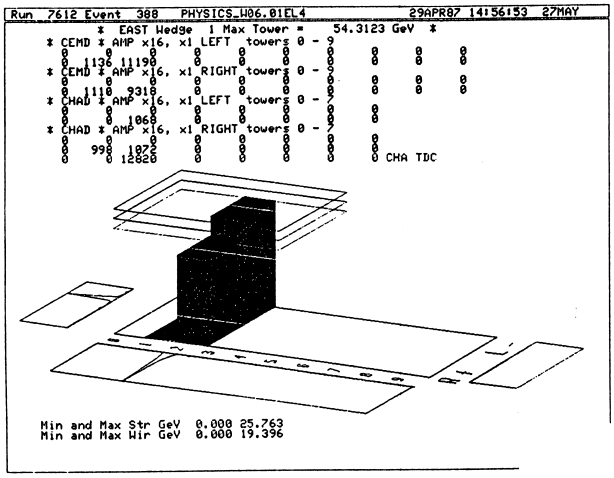

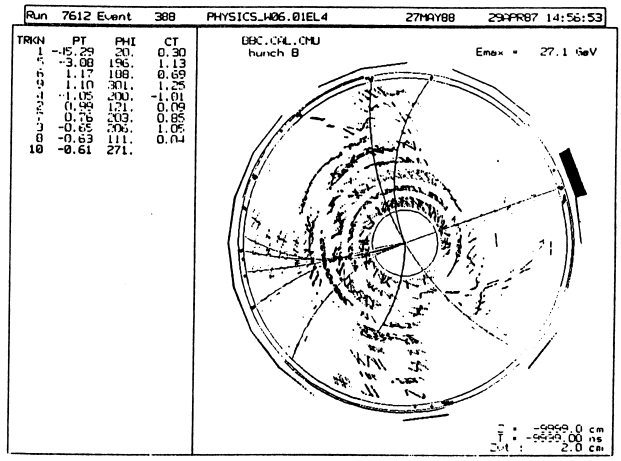

Fig. 5-5-3 (13)

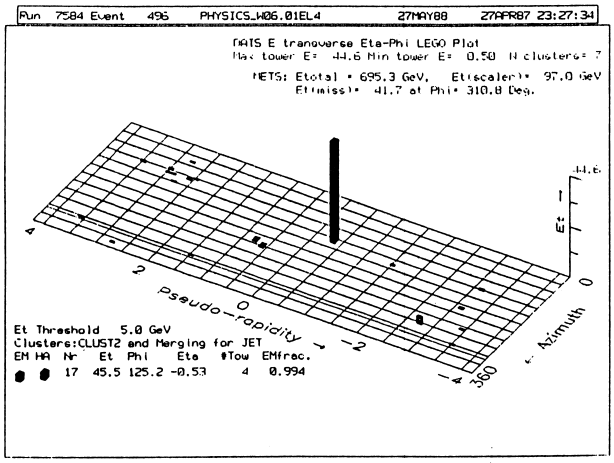

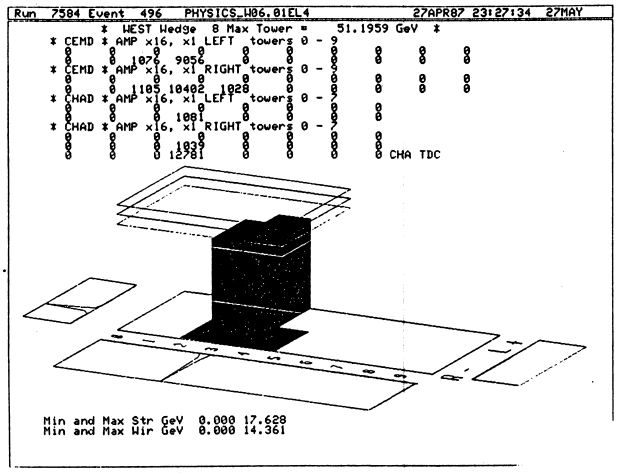

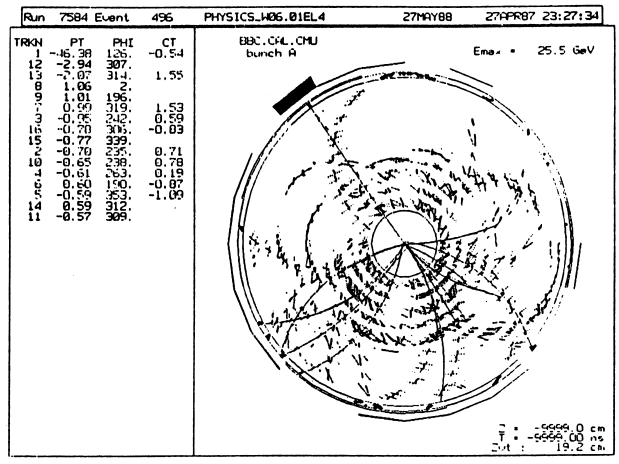

Fig. 5-5-3 (12)

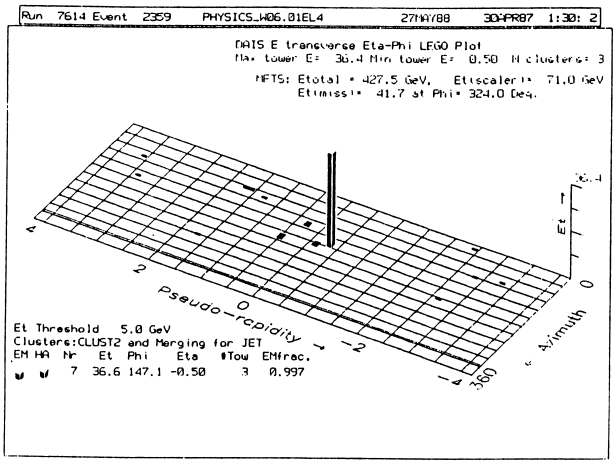

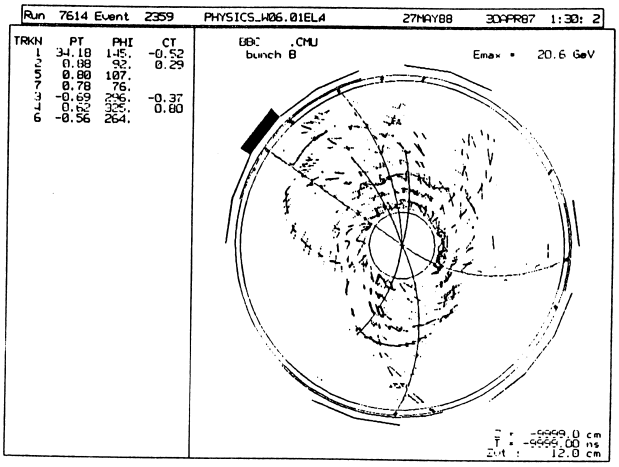

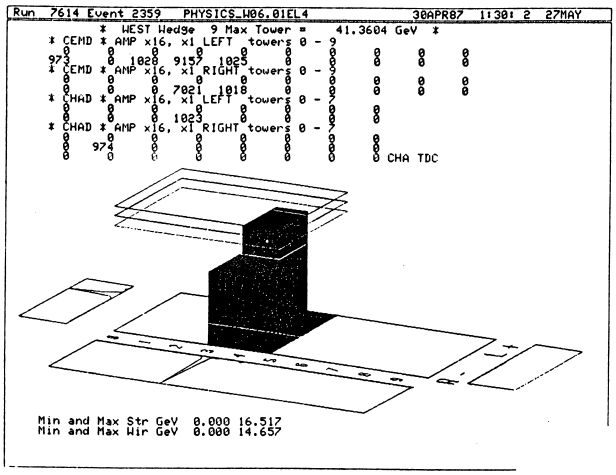

Fig. 5-5-3 (15)

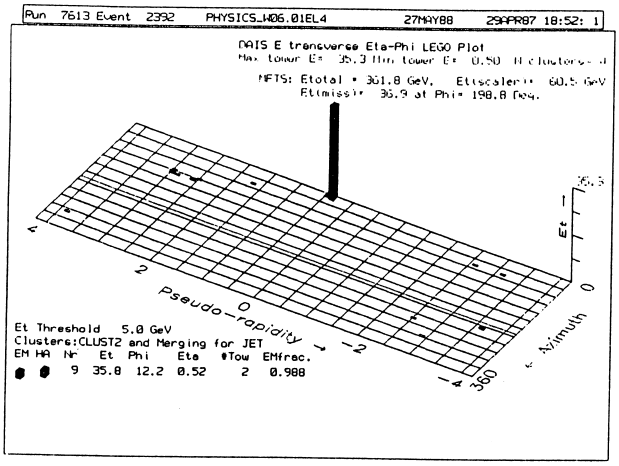

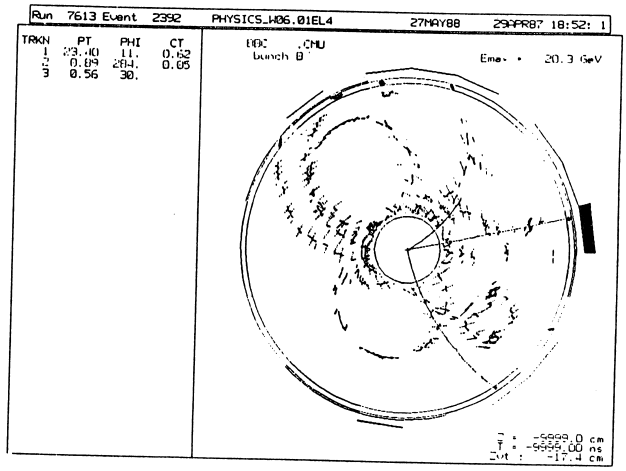

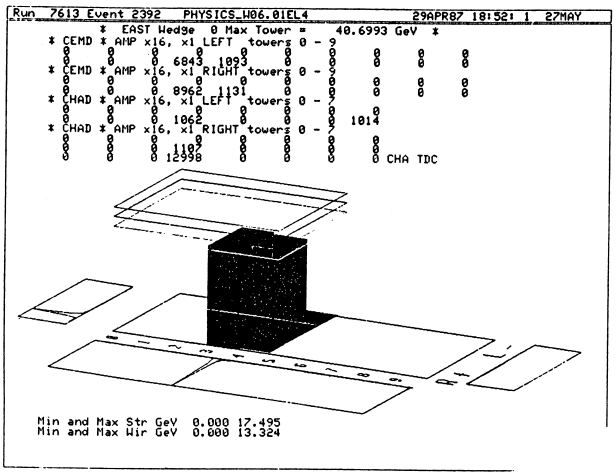

Fig. 5-5-3 (14)

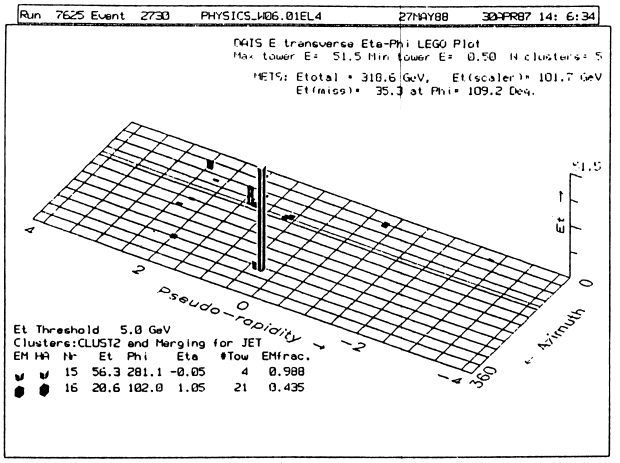

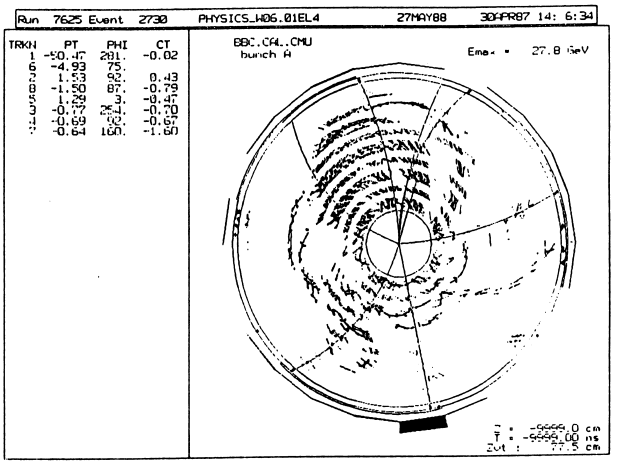

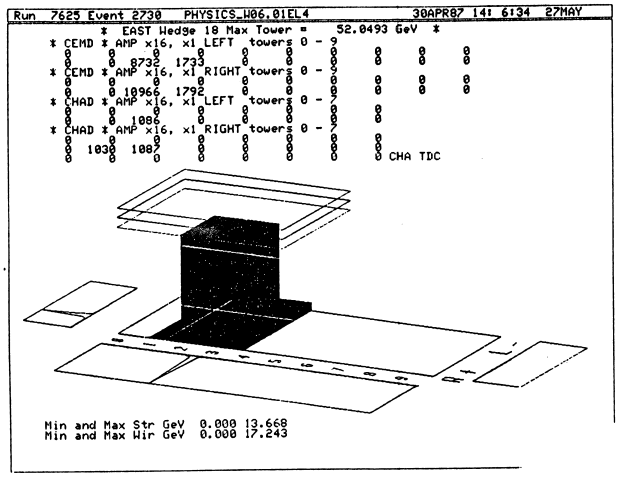

Fig. 5-5-3 (17)

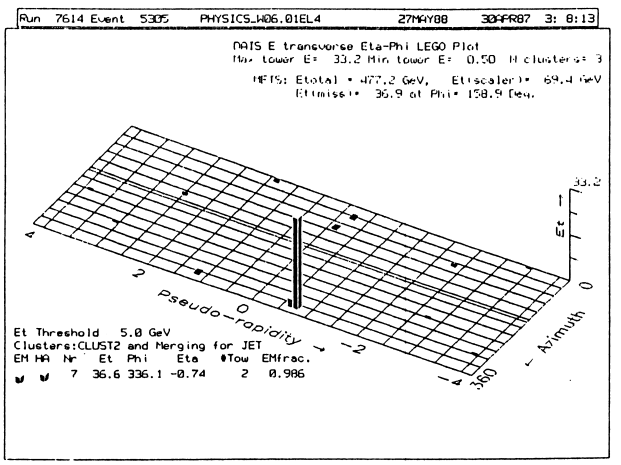

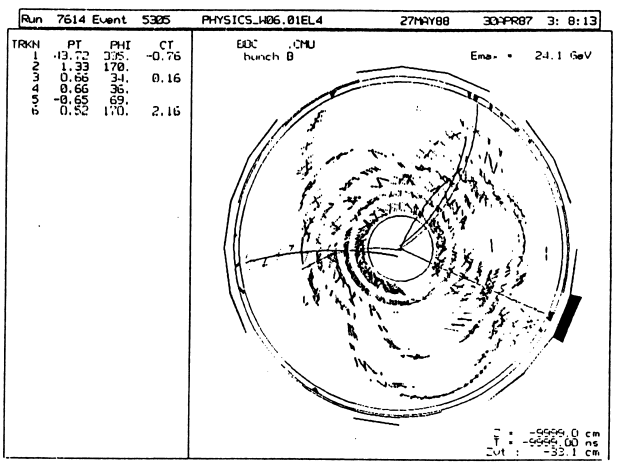

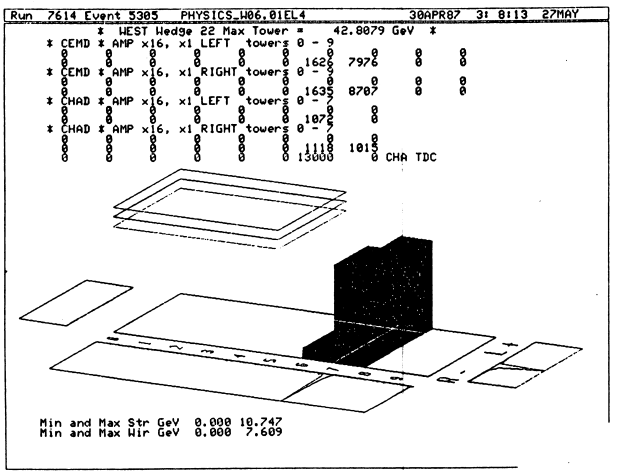

Fig. 5-5-3 (16)

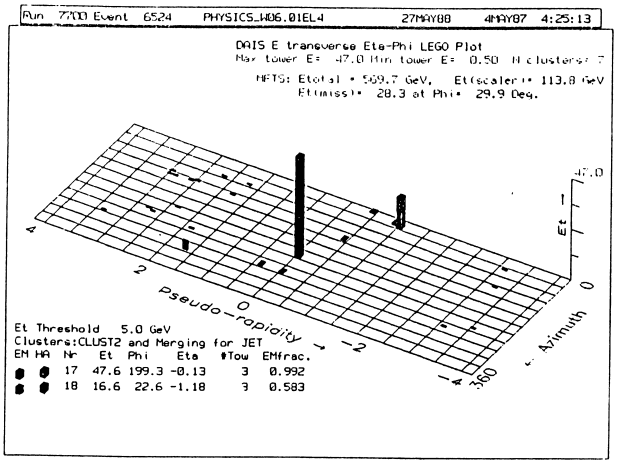

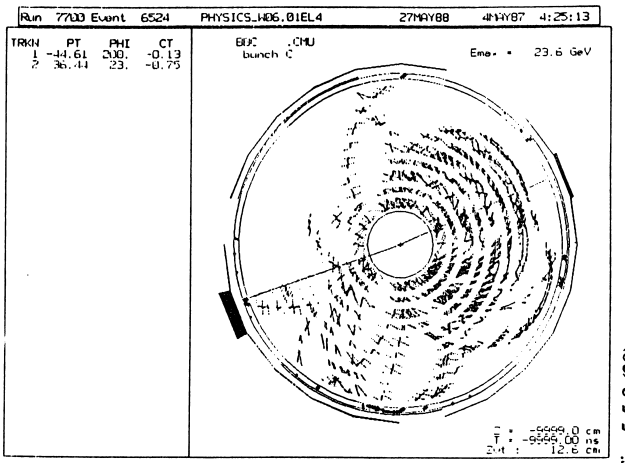

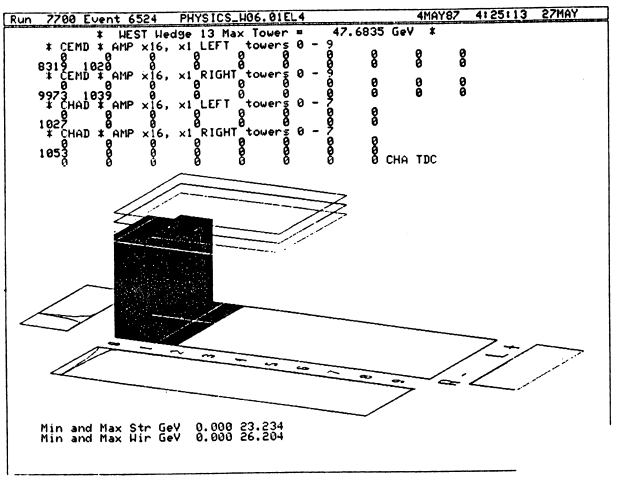

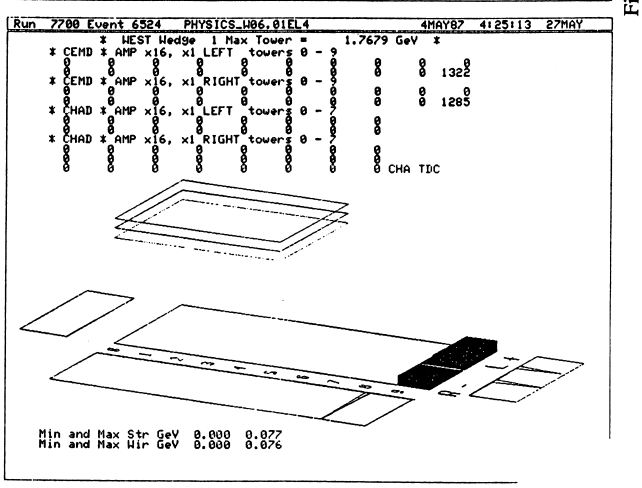

Fig. 5-5-3 (20)

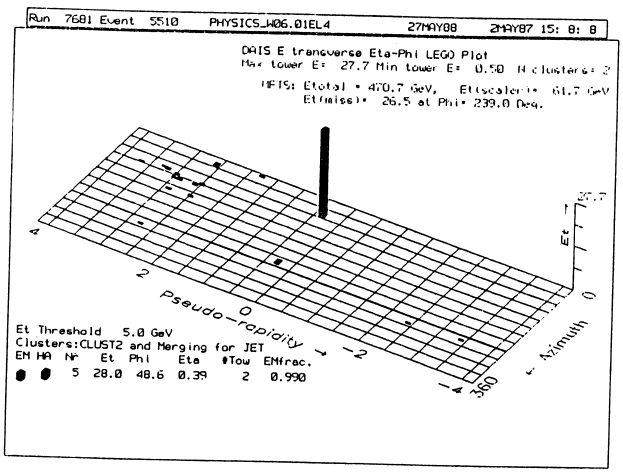

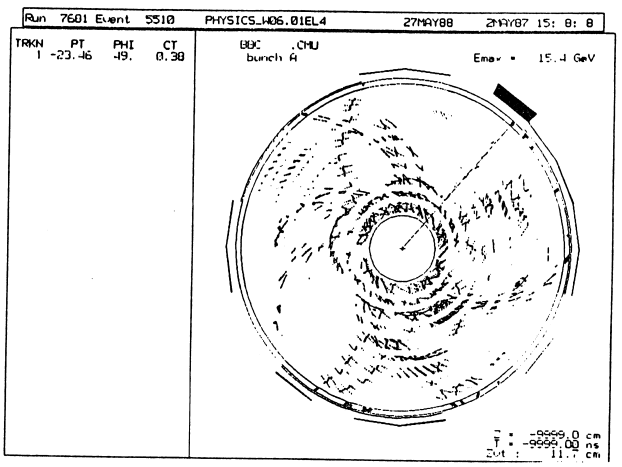

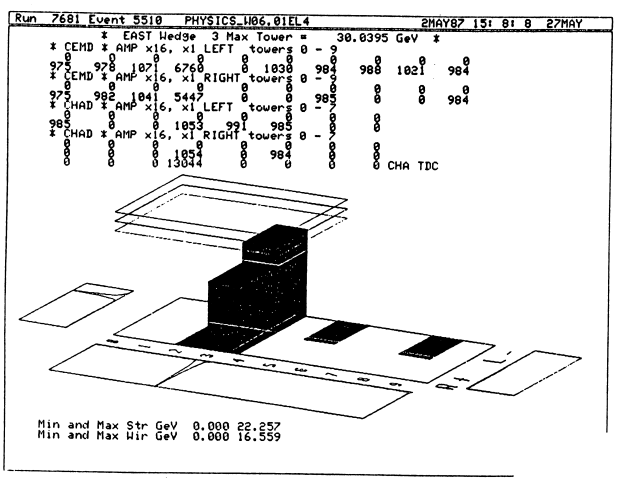

Fig. 5-5-3 (18)

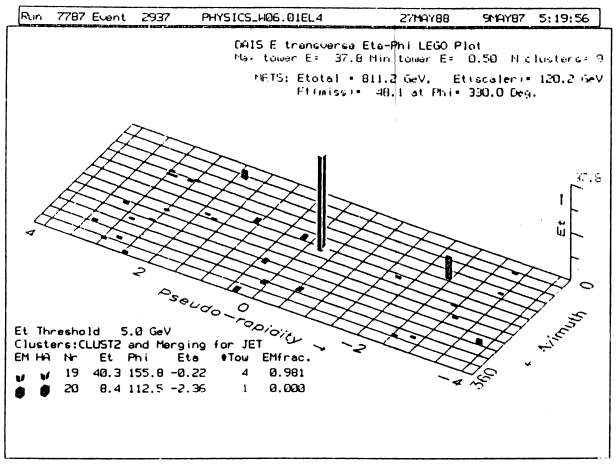

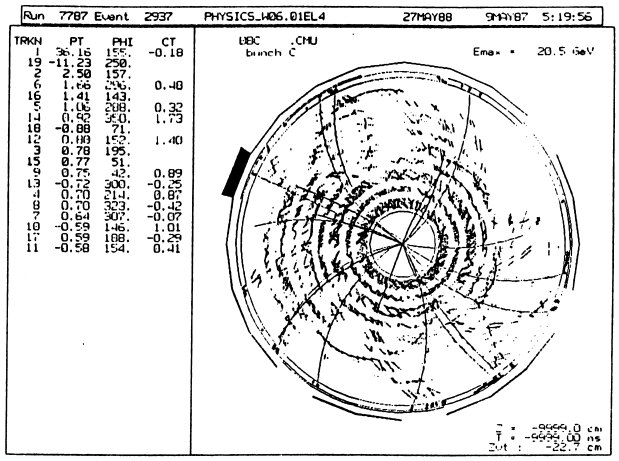

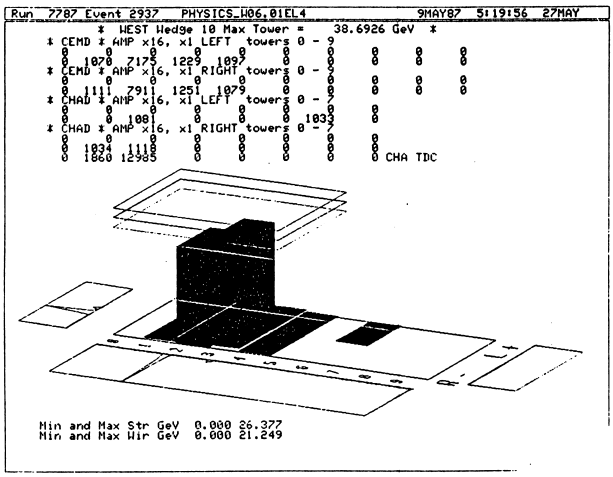

Fig. 5-5-3 (21)

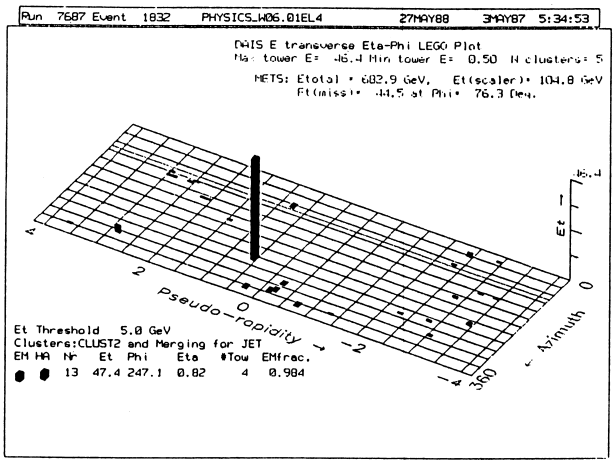

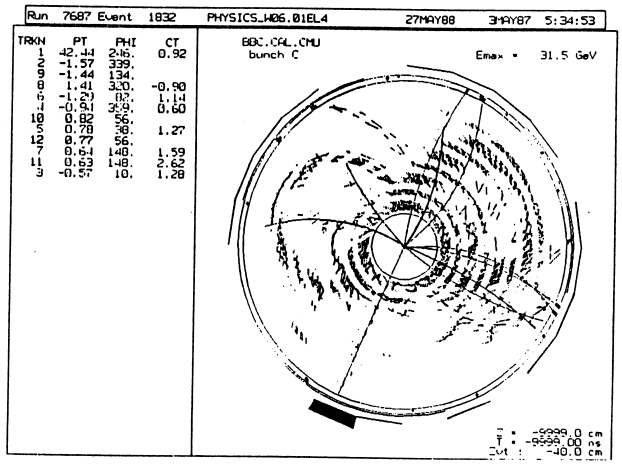

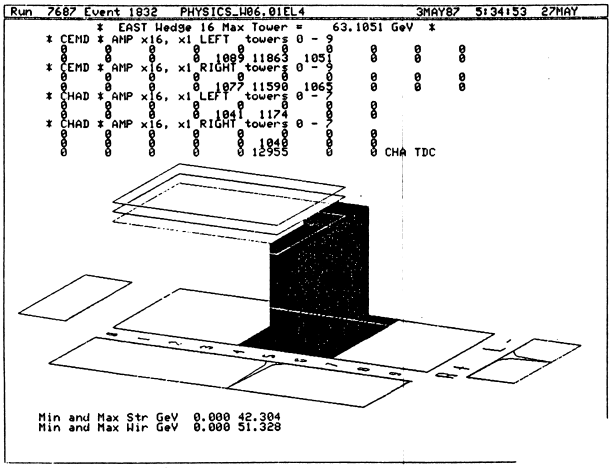

Fig. 5-5-3 (19)

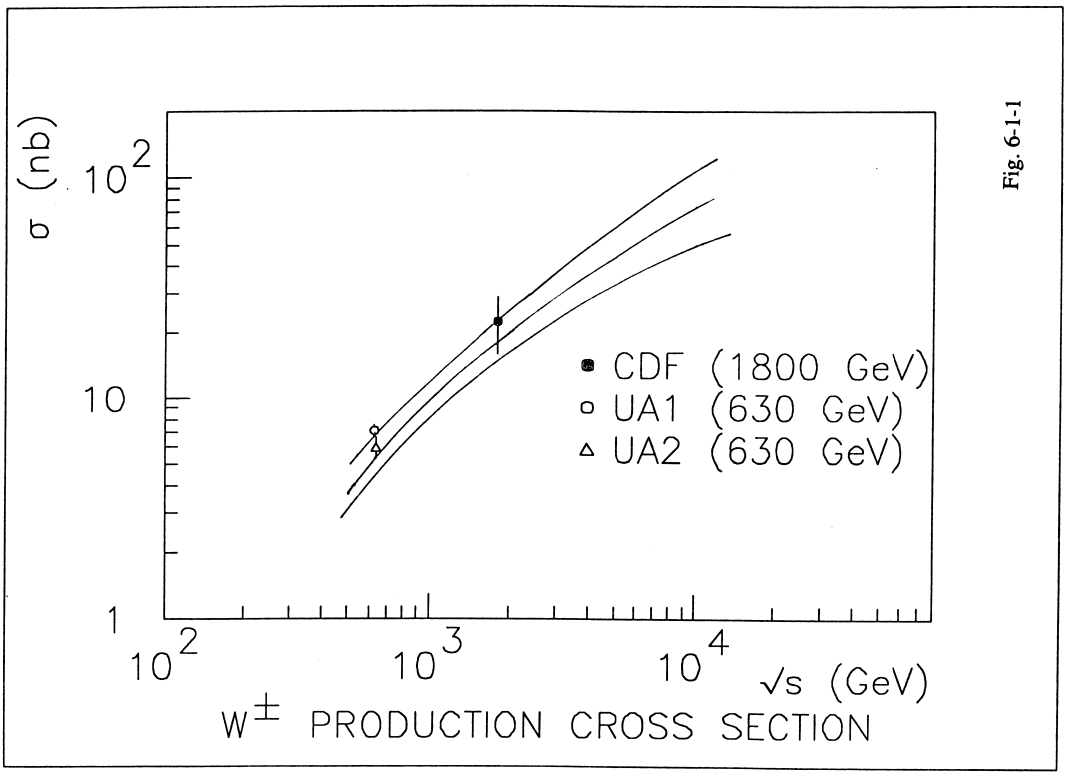

Fig. 6-1-1

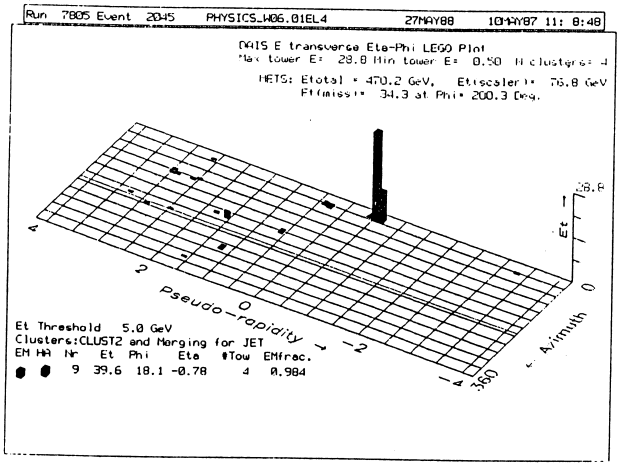

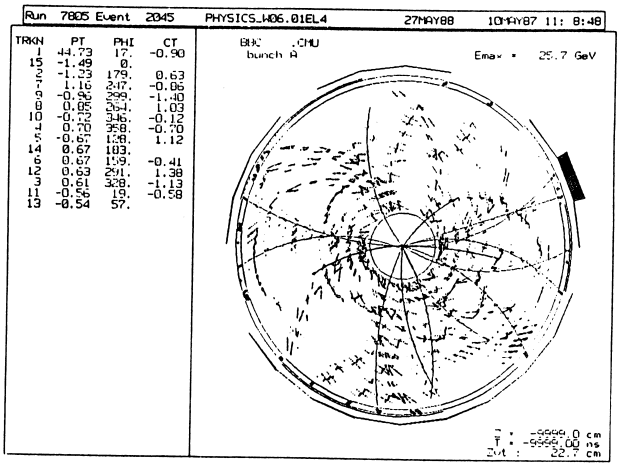

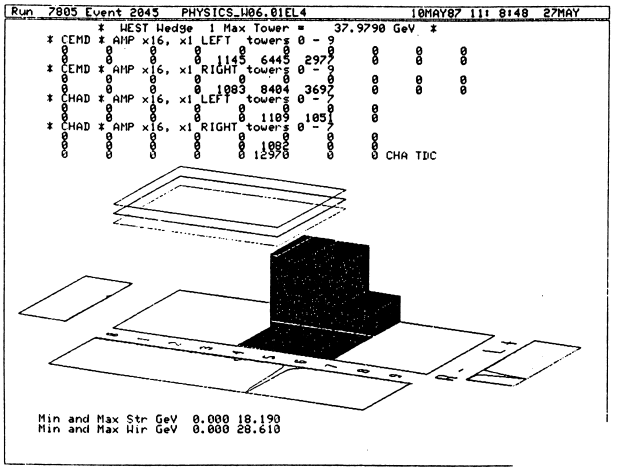

Fig. 5-5-3 (22)

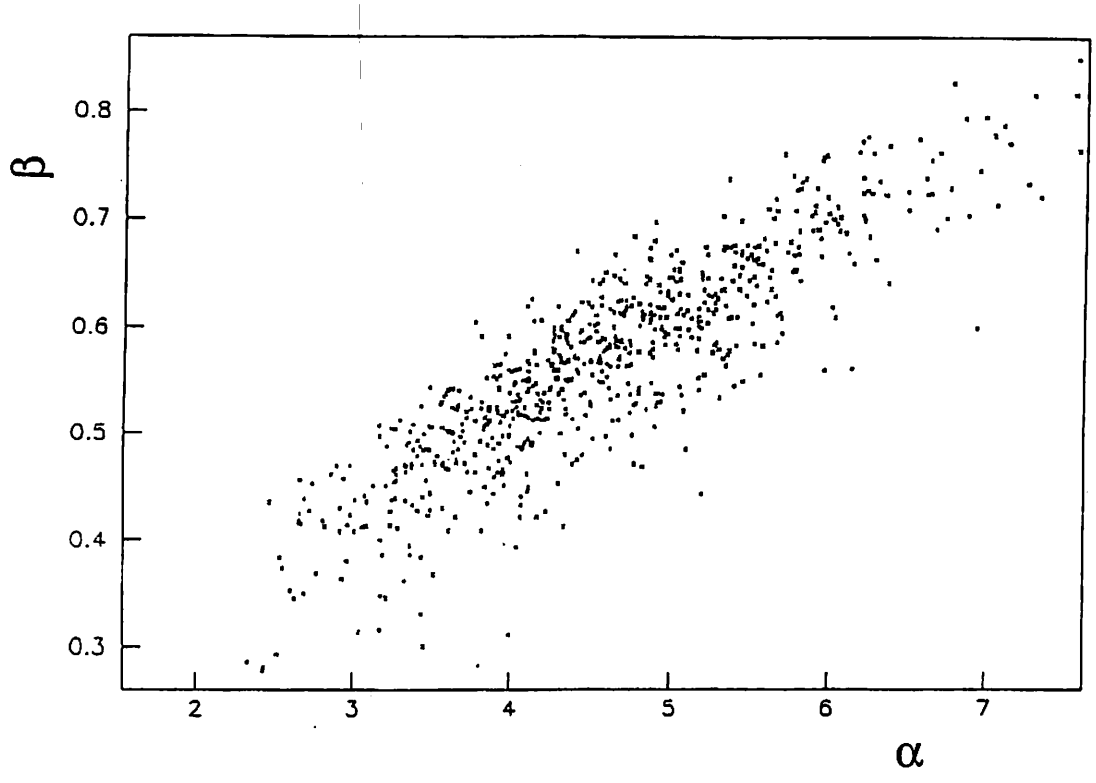

Fig. E-1

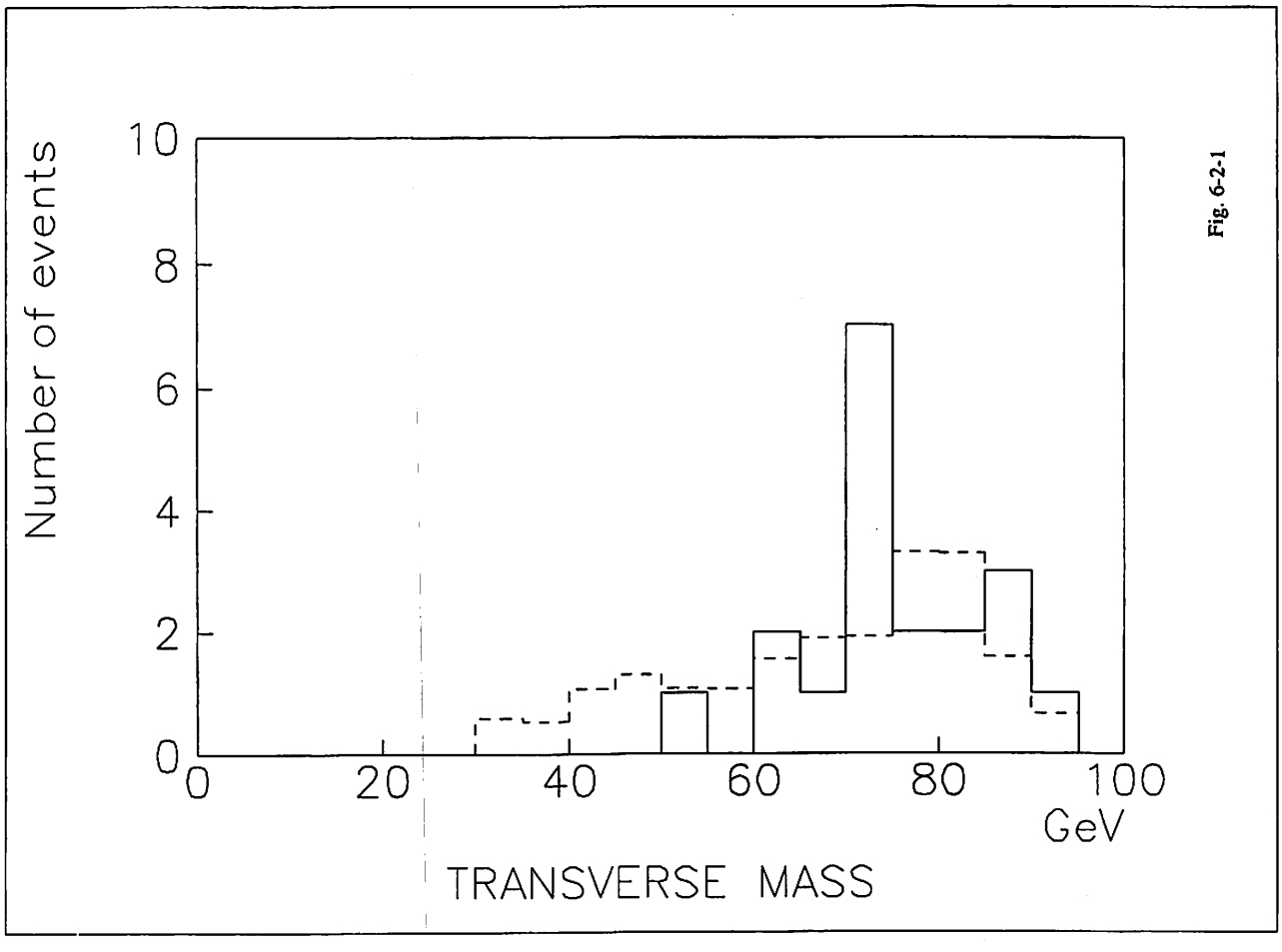

Fig. 6-2-1

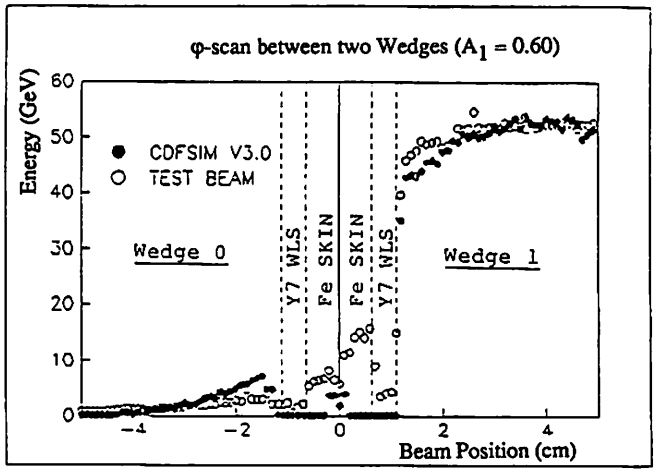
φ-scan between two Wedges (A_1 = 0.60)
Energy (GeV)
60
50
40
30
20
10
0
CDFSIM V3.0
TEST BEAM
Wedge 0
Wedge 1
Y7 WLS
Fe SKIN
Fe SKIN
Y7 WLS
−4
−2
0
2
4
Beam Position (cm)

Fig. E-2

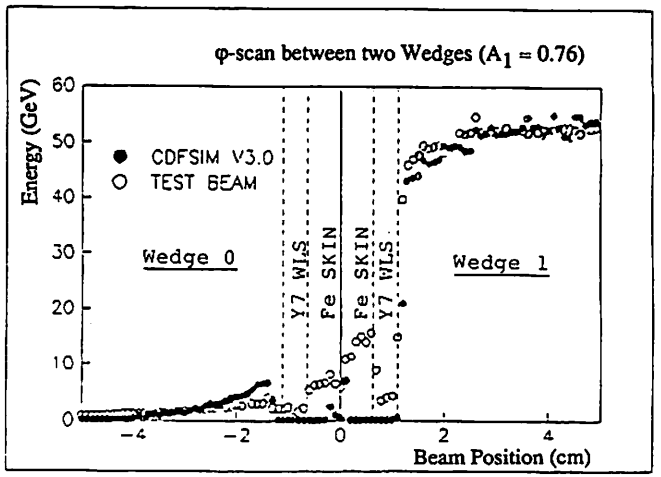
φ-scan between two Wedges (A_1 = 0.76)
Energy (GeV)
60
50
40
30
20
10
0
CDFSIM V3.0
TEST BEAM
Wedge 0
Wedge 1
Y7 WLS
Fe SKIN
Fe SKIN
Y7 WLS
−4
−2
0
2
4
Beam Position (cm)

Fig. E-3